

# INFRARED INTERSUBBAND TRANSITIONS IN NON-POLAR III-NITRIDES

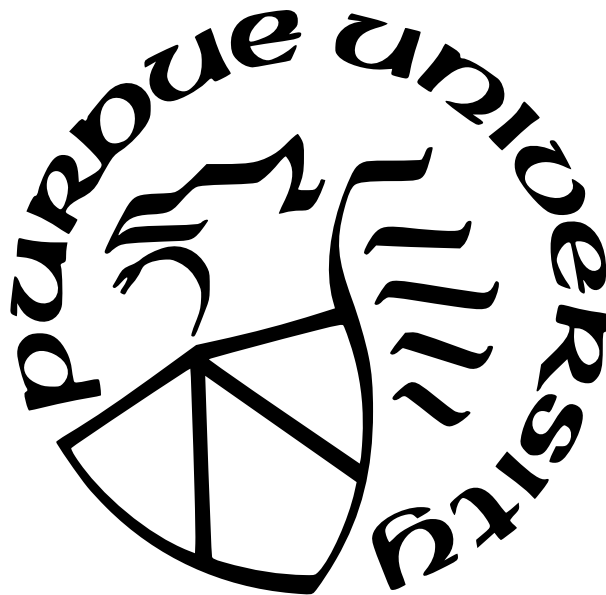
by  
Trang Nguyen

A Dissertation

*Submitted to the Faculty of Purdue University*

*In Partial Fulfillment of the Requirements for the degree of*

Doctor of Philosophy



Department of Physics and Astronomy

West Lafayette, Indiana

May 2022

**THE PURDUE UNIVERSITY GRADUATE SCHOOL  
STATEMENT OF COMMITTEE APPROVAL**

**Dr. Oana Malis, Chair**

Department of Physics and Astronomy

**Dr. Michael J. Manfra**

Department of Physics and Astronomy

Department of Electrical and Computer Engineering

Department of Materials Engineering

**Dr. Ken Ritchie**

Department of Physics and Astronomy

**Dr. Paul F. Muzikar**

Department of Physics and Astronomy

**Approved by:**

Dr. Gabor A. Csathy

## ACKNOWLEDGMENTS

I would like to thank my advisor, Professor Oana Malis, for her outstanding guidance. Professor Malis has always been willing to aid her students. Every time, her keen and innovative mind for physics amazes me. I feel really privileged to be her student.

I would like to thank my colleagues, Dr. Diaz, Dr. Cao, Brandon, Dr. Senichev, Ananthesh, etc., for their assistance with my research. I would like to thank the “special forces” of the physics department (Sandy, Janice, Pam, Carol, Dr. Lewicki, and others) for their insightful counsel. They prove to me that knowledge is not proportional to one’s title.

I would like to express gratitude to my parents (Nguyễn Hồng Vĩnh, Tôn Nữ Trang, Carman Munsell, and Lillie Munsell), my husband (Jeremy Munsell), my brothers (Nguyễn Tôn Vĩnh Trung and Nguyễn Tôn Vĩnh Thông), and my one-of-a-kind little “sister” Bo (QVy) for their support throughout my academic career. When others cast doubt me, you were the ones that stuck by my side. Without your unwavering support, I would not have been able to accomplish this remarkable feat. Con cảm ơn ba mẹ đã sinh con ra, yêu thương con, và nuôi con khôn lớn. Ông bà nội, con đã thực hiện được lời hứa của mình. Lời hứa tuy nhỏ nhưng là sức mạnh to lớn giúp con đi đến đích cuối.

I would like to thank many friends of mine-Nhung, Trang, Quỳnh, Kevin, Andres, Cheng An, Susan, Terrence, Alireza, Hongu, and more-for providing me with invaluable mental support throughout my PhD journey. Adeel Mugal, our very dear buddy, you will always be missed; your memory will live on forever in our heart.

Finally, I would like to extend my gratitude to Dr. Mojtaba Vaziri, my former advisor. He mentored me tremendously throughout my undergraduate studies at the University of Michigan-Flint. His incredible faith in me inspired me to continue working toward my ultimate goal no matter how difficult it may be.



# TABLE OF CONTENTS

LIST OF TABLES . . . . .	7
LIST OF FIGURES . . . . .	8
LIST OF SYMBOLS . . . . .	11
ABBREVIATIONS . . . . .	14
ABSTRACT . . . . .	16
1 INTRODUCTION TO III-NITRIDE SEMICONDUCTORS . . . . .	18
1.1 Motivation for nitride intersubband transitions in infrared range . . . . .	18
1.2 Applications of nitride intersubband transitions in infrared range . . . . .	19
1.3 Challenges of nitride semiconductors . . . . .	19
1.3.1 Large Effective Mass . . . . .	20
1.3.2 Internal Polarization Field . . . . .	20
1.3.3 Defects and Inhomogeneity . . . . .	23
2 INTERSUBBAND TRANSITIONS THEORY . . . . .	25
2.1 Intersubband Absorption Coefficient . . . . .	26
2.2 Many-Body Effects . . . . .	29
2.2.1 Exchange-Correlation Correction . . . . .	30
Hartree-Fock Approximation . . . . .	31
Local Density Approximation . . . . .	32
2.2.2 Depolarization Correction . . . . .	33
2.2.3 Excitonic Correction . . . . .	34
2.3 Linewidth Broadening . . . . .	35
2.4 Intersubband Transitions in III-Nitride Heterostructures . . . . .	36
3 TRANSMISSION ELECTRON MICROSCOPY . . . . .	38
3.1 Introduction to Transmission Electron Microscopy . . . . .	38

3.2	Elastic and Inelastic Scattering . . . . .	42
3.3	Diffraction Patterns . . . . .	43
3.4	Amplitude Constrast . . . . .	44
3.5	Challenges . . . . .	46
3.5.1	Damage from sample preparation process . . . . .	46
3.5.2	Damage from electron beam of TEM . . . . .	47
3.6	Scanning Transmission Electron Microscopy . . . . .	47
3.6.1	STEM Imaging . . . . .	47
3.6.2	STEM Sample Preparation . . . . .	48
	Traditional TEM Preparation Technique . . . . .	50
	Focused Ion Beam Technique . . . . .	52
4	INFRARED SPECTROSCOPY EXPERIMENTAL SETUPS AND PROCEDURES	55
4.1	Direct Transmission Measurements . . . . .	56
4.2	Attenuated Total Reflection Measurements . . . . .	58
4.3	Photoinduced Absorption Measurements . . . . .	59
5	M-PLANE STRAINED ALGAN/GAN . . . . .	60
5.1	Introduction . . . . .	60
5.2	Results . . . . .	62
5.3	Conclusion . . . . .	68
6	M-PLANE STRAIN-BALANCED (IN)ALGAN/INGAN . . . . .	69
6.1	Introduction . . . . .	69
6.2	Results . . . . .	70
6.3	Conclusion . . . . .	81
7	SUMMARY . . . . .	82
7.1	Review of Past Work on Lattice-Matched $In_{0.17}Al_{0.83}N/GaN$ Heterostructures	83
7.2	Future Work . . . . .	86
	REFERENCES . . . . .	93

A	TRADITIONAL TEM PREPARATION RECIPE FOR POLAR AND NON-POLAR III-NITRIDES . . . . .	103
A.1	Allied MultiPrep System 8” Precision Polishing System . . . . .	103
A.2	Gatan Dimpler Grinder II Model 657 . . . . .	104
A.2.1	General Procedure . . . . .	104
A.2.2	Improvement of Dimpler . . . . .	105
A.3	Gatan PIPSII Model 695 . . . . .	106
A.3.1	Sample and Gun Alignment . . . . .	106
A.3.2	PIPS Process . . . . .	108
B	FIB (TEM PREPARATION) FOR POLAR AND NON-POLAR III-NITRIDES RECIPE . . . . .	110
B.1	FEI Nova 200 Nanolab . . . . .	110
B.2	Thermo Scientific Helios G4 UX Dual Beam . . . . .	117
B.3	EZ-Lift - Helios G4 UX Dual Beam . . . . .	124
B.4	Omniprobe - FEI Quanta 3D FEG . . . . .	125
C	OPERATING NANOMILL FOR POLAR AND NON-POLAR III-NITRIDES . .	127
D	ALIGNING TEM INSTRUMENTS . . . . .	130
D.1	FEI-Technai T20 . . . . .	130
D.2	FEI-Talos . . . . .	133
D.3	Thermo Fisher Scientific-Themis Z . . . . .	138
D.3.1	TEM Mode Pre-alignment Process . . . . .	138
D.3.2	STEM Mode Pre-alignment Process . . . . .	140

## LIST OF TABLES

3.1	Advantages and disadvantages of different types of radiation for microscopy applications. . . . .	38
5.1	Summary of structural parameters, observed ISBA energy peak, experimental FWHM of ISBA peak, and theoretical calculation of the ISB transitions energies for a series of polar and non-polar $AlGaN/GaN$ heterostructures. . . . .	62
6.1	Summary of structural parameters, experimental results including ISBA energy peaks and FWHM of absorption peaks, and theoretical calculations of the transition energies for a series of m-plane $(In)AlGaN/InGaN$ MQWs [59]. . . . .	73
7.1	Summary of the structural parameters and the experimental results including ISBA energy peaks and FWHM of absorption peaks for a series of polar c-plane (near) lattice-matched $Sc_{0.15}Al_{0.85}N/GaN$ MQWs. . . . .	87
A.1	Polishing recipe for plan-view (cross-section) III-nitrides. . . . .	104

## LIST OF FIGURES

1.1	Wurtzite structure of $GaN$ , where x-, y-, z-directions are normal to a-, m-, c-planes, respectively. . . . .	22
1.2	Conduction band edge and probability amplitudes of the ground state and the first excited state of $Al_{0.85}Ga_{0.15}N/GaN$ in (a) polar c-plane direction and (b) non-polar m-plane direction with the well of 2.5 nm and the barrier of 3.1 nm. .	22
1.3	Conduction band edges and energy levels of the ground state and the first excited state of c-plane $Al_{0.83}Ga_{0.17}N/GaN$ and $In_{0.17}Al_{0.83}N/GaN$ undoped heterostructures with the well of 5nm and the barrier of 3.03 nm. . . . .	23
2.1	The difference between interband and ISBTs in a single non-polar m-plane $AlGaN/GaN$ quantum well system. . . . .	25
2.2	$45^\circ$ facets multi-pass waveguide used for ISBA. . . . .	29
2.3	The effect of many body corrections on the ISBT energy as a function of sheet charge density for 3.2 nm thick $GaN$ QWs and 2.05 nm thick barriers with non-polar m-plane $Al_{0.56}Ga_{0.44}N$ . This calculation was done using the HFA correction.	30
3.1	Basic TEM anatomy including gun, condenser lens system, objective lens system, projector lens system, and viewing screen/detector/camera from top to bottom.	40
3.2	Different scattering mechanisms in TEM. . . . .	42
3.3	Bragg diffraction in a crystal. . . . .	44
3.4	Schematic of image formation in TEM and STEM modes. . . . .	49
3.5	Traditional TEM Sample Preparation. . . . .	51
3.6	Schematic of the electron and ion beams of FIB instrument (left) and FIB milling process of H-bar FIB process (right). . . . .	53
3.7	In-situ lift out FIB. . . . .	54
4.1	FT-IR schematic layout. . . . .	56
4.2	Schematic of the overlap of the $\vec{E}$ field of the standing wave with the active region of MQW in the case without (a) and with (b) a metal cap layer. . . . .	57
4.3	Experimental setup for (a) ATR-FT-IR and (b) direct-FT-IR ISBA measurement techniques. . . . .	58
4.4	PIA measurement setup. . . . .	59
5.1	ISB transition spectra of sample A, B, C, and D (solid lines) and their fitting (dash lines) in black, red, blue, and magenta, respectively. The ISBA spectra of samples A and C were fitted using single peak Lorentzian fitting. The ISBA spectra of samples B and D were fitted using multi-peak Lorentzian fitting. . . .	63



5.2	The dependence of the ISBA energy on the QW thickness of sample A. The black and red lines are theoretical calculations with exchange interaction and total many-body correction (including exchange interaction, depolarization shift, and excitonic correction), respectively. The green straight line is the experimental ISBA of sample A obtained from direct-FT-IR measurement. . . . .	64
5.3	HRHAADF-STEM image(a) and EDS elemental maps of <i>Ga</i> (b) and <i>Al</i> (c) of sample A with zone-axis along the a-axis [32]. . . . .	65
5.4	Multi-peak Lorentzian fits for the ISBA spectra of samples B(left) and D(right) which have <i>Al</i> composition of 56% and 54% suggested by HRXRD, respectively. The Lorentzian fit for sample B contains peaks at 267 meV, 332 meV, and 396 meV with FWHMs of 110 meV, 72 meV, and 68 meV, respectively. The Lorentzian fit for sample D includes peaks at 356 meV, 427 meV, 493 meV, and 549 meV with FWHMs of 59 meV, 81 meV, 57 meV, and 201 meV, respectively. . . . .	67
5.5	Conduction band edge (black) and probability of the ground (blue) and first excited states (red) for sample B (left) and sample C (right). . . . .	68
6.1	[Reprinted/Adapted] with permission from [59] ©Optica Publishing Group. HRHAADF-STEM of sample H (a) and B (b-d) [59]. The lighter the element, the darker contrast appears on HAADF-STEM images. . . . .	71
6.2	[Reprinted/Adapted] with permission from [59] ©Optica Publishing Group. ISBA spectra of sample A using direct-FT-IR (red curve) and ATR-FT-IR (black curve) method. . . . .	72
6.3	[Reprinted/Adapted] with permission from [59] ©Optica Publishing Group. Effect of CBO on expected ISBA energy with HFA and LDA approaches for a single QW using sample F's structure. The experimental ISBA energy of sample F from direct-FT-IR was used to compare with theoretical estimations. The insets represents the conduction band edge and two lowest energy states inside QW [59]. . . . .	76
6.4	[Reprinted/Adapted] with permission from [59] ©Optica Publishing Group. Effect of aluminum mole fraction on calculated ISBA energy with HFA and LDA approaches. Samples in group I (A, B, and C) are plotted to compare with the theoretical estimation. . . . .	77
6.5	[Reprinted/Adapted] with permission from [59] ©Optica Publishing Group. Effect of sheet charge density on simulated ISBA energy using HFA (a) and LDA (b) methods. Samples in group II are listed for a comparison with the theoretical prediction [59]. . . . .	79
6.6	[Reprinted/Adapted] with permission from [59] ©Optica Publishing Group. The effect of QW width on ISBA energy simulated by HFA and LDA approaches. Samples in group III are used in comparison between experimental and theoretical results. The inset represents the simulated conduction band edge and electron wavefunction of the first 3 states of sample H [59]. . . . .	80

7.1	Experimental ISB transition spectrum of a c-plane 15-period $In_{0.15}Al_{0.85}N/GaN$ SL with the QW thickness of 3.15 nm and the barrier thickness of 4.88 nm. The ISBA curve has its peak located at 547 meV with a FWHM of 140 meV. . . . .	84
7.2	Plan-view HAADF-STEM image of a 30nm-thick InAlN c-plane samples grown at nitrogen flux (a) $1.75 \times 10^{14}$ , (b) $4.23 \times 10^{14}$ , (c) $6.42 \times 10^{14}$ , and (d) $1.26 \times 10^{15} atom/cm^2 s$ . Honeycomb cells consist of indium-rich borders and aluminum-rich centers [99].	85
7.3	HAADF-HRSTEM of sample D. The dark (bright) layers are $ScAlN$ ( $GaN$ ) layers.	86
7.4	Conduction band edges, energy levels, and probability amplitudes of the ground state and the first excited state of c-plane $Sc_{0.1875}Al_{0.8125}N/GaN$ (solid lines) and c-plane $Al_{0.9}Ga_{0.1}N/GaN$ (dash-lines) 10 s $\delta$ -doping at 1 nm away from the QW with the well of 4 nm and the barrier of 6 nm. . . . .	89
7.5	Experimental ISBA spectra of samples A (black), B (blue), and C (red) with ISBA peaks at 609 meV, 617 meV, and 611 meV, corresponding to FWHMs of 69 meV, 32 meV, and 44 meV respectively. The direct-FT-IR technique was used to obtain these spectra. . . . .	90
7.6	Experimental ISBA spectra of group II samples (left) and the effect of QW width on the ISBA energy (right). The theoretical calculations were done with polar c-plane $Sc_{0.1875}Al_{0.8125}N/GaN$ , 10 s $\delta$ -doping at 1 nm in the QB away from each side of the QW. . . . .	91
A.1	Cross-section view of mounting plan-view sample onto PIPS holder before milling.	108
B.1	Top view of lamella during thinning process. Lamella is cleaned from both sides leaving the middle region to be the thinnest part for TEM imaging. . . . .	117
B.2	FIB process . . . . .	120
B.3	Cross-section view of lamella during milling process. From left to right are: corrected lamella shape, losing the protection layer too fast, and losing lamella's bottom too fast. . . . .	124
D.1	TEM Pre-alignment Process . . . . .	139
D.2	STEM Pre-alignment Process . . . . .	141

## LIST OF SYMBOLS

$m^*$	electron effective mass
$f_{nn'}$	ISBT strength between 2 confined states inside the QW
$\hbar\omega_{nn'}$	energy difference between states $ n\rangle$ and $ n'\rangle$
$\langle n p_z n'\rangle$	momentum matrix element
$m_0$	free electron mass
$m_{GaAs}$	electron effective mass of GaAs
$\vec{P}_{internal}$	total internal polarization field
$E_{transition}$ or $E$	transition energy
$L$	QW width
$V(r)$	lattice potential
$V_s(r)$	potential from the (superlattice) heterostructure.
$p$	momentum
$\psi_i(r)$	electron wavefunction inside band ( $\nu$ )
$f_i(r)$	normalized envelop function with quantum number $i$
$u_\nu(r)$	normalized Bloch function in band $\nu$
$A$	the surface area of the quantum well in the xy-plane
$\vec{k}$	in-plane vector
$k_x(y)$	x(y)-component of $\vec{k}$
$\hbar$	Planck constant
$\pi$	Pi
$E_i$	confined energy of the electronic states inside the infinite quantum well
$W_{if}$	transition rate from state $i$ to state $f$
$H$	Hamiltonian
$\vec{A}$	vector potential
$\vec{E}$	electric field
$E_0$	electric field amplitude
$\vec{s}$	polarization unit vector
$I_{ab}$	absorbed EM energy per unit time per unit volume

$V$	volume of 3DEG
$I_{in}$	intensity of the incident radiation
$\eta$	refractive index
$\epsilon_0$	vacuum permittivity
$c$	speed of light
$\alpha_{ISB}$	ISBA coefficient
$T$	transmission rate
$m$	number of passes of EM wave through the active region
$N$	number of Qws
$\theta$	angle between the incident light and the growth direction
$C$	coupling factor representing the overlap of standing wave of $\vec{E}$ and the active region.
$\epsilon_r$	dielectric constant
$\psi(\vec{r})$	wavefunction of electron
$V(\vec{r})$	combination of lattice potential and external field
$U^{ion}(\vec{r})$	doping profile
$k_F$	Fermi wavevector
$\psi_0(x)$	wavefunction of single electron in the ground state
$\alpha$	depolarization shift (a part of many-body correction)
$E_{21}$	corrected transition energy from the exchange-correlation (a part of many-body correction)
$n_s$	charge density of the 2DEG
$V_{ex}$	exchange-correlation potential (a part of many-body correction)
$r_s$	dimensionleess parameter
$a^*$	effective Bohr radius
$\beta$	excitonic shift (a part of many-body correction)
$E_{correction}$	total corrected transition energy (a part of many-body correction)
$\Gamma$	full-width-half-maximum
$\tau_{inelastic}$	mean scattering time for inelastic collisions

$\sigma$	scattering cross section
$Z_{nucleus}$	atomic number of nucleus
$E_K$	kinetic energy
$\alpha$	fine structure (TEM section)
$d$	interplannar distant
$\Delta l$	total path difference
$\lambda$	wavelength

## ABBREVIATIONS

IR	infrared
QW(s)	quantum well(s)
SL(s)	superlattice(s)
ISBT	intersubband transitions
ISBA	intersubband absorption
QCLs	quantum cascade lasers
QWIPs	quantum well infrared photodetectors
ISB	intersubband
CBO	conduction band offset
LO	longitudinal-optical
FT-IR	Fourier transform infrared
MCT	Mercury Cadmium Telluride
MQW(s)	multiple quantum well(s)
(S)TEM	(scanning) transmission electron microscopy
EM	electromagnetic
2DEG	2D electron gas
EDS	energy dispersive x-ray spectroscopy
HAADF	high-angle annular dark field
HR-(S)TEM	high resolution (scanning) transmission electron microscopy
DP	diffraction pattern
BF	bright field
DF	dark field
FIB	focused ion-beam
PIPS	precision-ion-polishing system
SRIM	Stopping-and-Range-of-Ions-in-Matter
ATR	attenuated total reflection
PIA	photoinduced absorption
AFM	atomic force microscopy

XRD	x-ray diffraction
MBE	molecular beam epitaxy
PA-MBE	plasma-assisted molecular beam epitaxy
RMS	root mean square
FWHM	full-width-half-maximum
LDA	local density approximation
HFA	Hartree-Fock approximation

## ABSTRACT

Infrared intersubband absorption of III-nitride materials has been studied rigorously due to its broad potential applications into optoelectronic devices. III-nitrides have advantages of large conduction band offset, large longitudinal-optical phonon energy, and fast intersubband relaxation time. These special characteristics make nitrides promising materials for intersubband devices in the near-infrared range. However, the existence of challenges from these materials delays the progress towards the realization of high performance nitride intersubband devices. In this document, we discuss the challenges of III-nitrides and our efforts towards high intersubband transitions strength of different nitrides, in particular non-polar m-plane  $AlGaN/GaN$ , non-polar m-plane near strain-balanced  $(In)AlGaN/InGaN$ , and polar lattice-matched  $InAlN/GaN$ . Samples are characterized by multiple methods including atomic force microscopy, high-resolution x-ray diffraction, high-resolution (scanning) transmission electron microscopy, and Fourier transform infrared spectroscopy.

Polar c-plane  $AlGaN/GaN$  exhibits good agreement between experimental and predicted results for the intersubband transition energy. However, the lattice strain between layers caused by the lattice mismatch between materials leads to a large number of defects, affecting the vertical transport and resulting in low-quality devices. Lattice-matched  $InAlN/GaN$  was suggested as an alternative to eliminate this lattice strain, thus providing a better quality material for devices. We discuss the challenges of growing homogeneous  $InAlN$  alloys that persist after exploring a wide range of growth conditions. Additionally, the non-polar m-plane  $AlGaN/GaN$  is also being investigated. Low  $Al$ -composition m-plane  $AlGaN/GaN$  experimental intersubband absorption shows good agreement with the theoretical results. As the  $Al$  composition exceeds 60%, however, the m-plane  $AlGaN$  alloy becomes kinetically unstable during plasma-assisted molecular beam epitaxy growth, resulting in unique nanostructures that affect the intersubband transition energy and linewidth. For the first time, we reported the ISBA energy of near strain-balanced non-polar m-plane  $(In)AlGaN/InGaN$  heterostructures in the mid-infrared range with narrow linewidths comparable to the smallest full-width-half-max published in the literature for non-polar m-plane  $AlGaN/GaN$  su-



perlattices. Additionally, we propose polar near lattice-matched  $Sc_{0.15}Al_{0.85}N/GaN$  as an alternative to c-plane lattice-matched  $InAlN/GaN$ .

# 1. INTRODUCTION TO III-NITRIDE SEMICONDUCTORS

## 1.1 Motivation for nitride intersubband transitions in infrared range

In the high-technology age, better performing optoelectronic devices in the range of infrared (IR) wavelengths are in high demand. Most common semiconductor devices rely on optical transitions between the valence band and the conduction band. Because of this, the operating range of these devices is determined by the bandgap of the material. However, intersubband transitions (ISBTs) are optical transitions between quantized energy levels in a quantum well made by a conduction band offset (CBO) of a combination of different materials. Devices using intersubband transitions can operate in a much wider range of wavelengths. When a heterojunction is formed from dissimilar alloys, the difference in bandgap energy leads to quantum wells (QWs) with finite barriers. Given a couple of semiconductors, the confined electronic energy states inside the QW that produce the optical transition can be tuned by changing the width of the well. The use of ISBTs offers a substantial improvement over traditional semiconducting technology. Furthermore, this approach creates the possibility of making new devices like quantum cascade lasers (QCLs), quantum well infrared photodetectors (QWIPs), etc.

Devices using ISBT inherit a few characteristics from the constituent alloys. One property is the CBO, also known as the height of the QB, that indicates the maximum possible confined energy of the QW. Another property is the longitudinal-optical (LO) phonon energy that affects the population inversion of the devices, causing challenges for lasing. Nitride-based semiconductors ( $AlN$ ,  $InN$ ,  $GaN$ , and their alloys) have been widely used in ultraviolet and visible optoelectronic devices with significant societal impact [1]–[6].

To appreciate why III-nitride semiconductors are interesting candidates for ISB transition devices, we will discuss the differences between arsenide and nitride semiconductors. While  $Al_{0.4}Ga_{0.6}As/GaAs$  has a  $CBO \approx 0.3$  eV, and the CBO of  $In_{0.53}Ga_{0.47}As/In_{0.52}Al_{0.48}As$  is about 0.5 eV, III-nitride semiconductors can have  $CBO > 1$  eV that allows bigger transition energy (smaller wavelength) between the confined states. Additionally, III-nitride alloys have larger LO phonon energy (90 meV) than arsenides (36 meV) that allows these materials to

be used for detectors and lasers in the far-IR (30-60  $\mu m$ ) in addition to the near-IR (1.5-3  $\mu m$ ) regimes.

## 1.2 Applications of nitride intersubband transitions in infrared range

Over the past 20 years, Fourier transform infrared (FT-IR) spectroscopy has been used for chemical sensing of over 50,000 organic chemicals [7]. This makes FT-IR spectroscopy a crucial technique for chemical detection, especially in the medical field. Since mid-20<sup>th</sup> century, FT-IR spectroscopy has been shown to be extremely useful for many biomedical fields of research, especially cancer research [8]. The *HgTeCd* (MCT) detector is commonly used in the IR regime, but it is costly to make. The nitride QWIP is an alternative type of detector based on ISBT that has high sensitivity [9].

Another promising application of III-nitrides is lasers for gas sensing. Despite the fact that lead salt diode lasers are the most common device for trace gas sensing, ISB infrared lasers are a potential alternative due to their precision and tunability [10]. The QCLs are known for their narrow linewidth at high power at room temperature. In addition, *InGaAs/InAlAs* QCLs have excellent performance at high power in the mid-IR range compared to the lead salt laser. However, the arsenide materials have a small CBO that limits their operation at shorter wavelengths. With higher CBO ( $>1$  eV), novel nitride materials are suitable for building near- and far-IR QCLs.

## 1.3 Challenges of nitride semiconductors

Though the III-nitrides are promising for the development of optoelectronic devices in the near-IR regime, these materials still present a few challenges, such as large effective mass, internal polarization field (along the c-axis of *AlGaN/GaN*), lattice mismatch between *AlN* and *GaN*, defects, etc. However, it should be emphasized that solutions have been proposed to some of these obstacles. For example, the complications resulting from the internal polarization field can be solved by using m-plane *AlGaN/GaN*, since the m-plane is known to be a non-polar direction. The high composition of *Al* in m-plane *AlGaN/GaN* heterostructures has been shown to have a high interface roughness due to the kinetic instability of *AlGa*N

alloys under metal-rich conditions [11]. This problem affects the ISBT strength, which is fundamentally related to device performance and is discussed in greater depth in chapter 5. A proposed solution is to reduce the percentage of *Al* and replace *GaN* with  $In_xGa_{1-x}N$ . We also investigate another nitride alloy,  $In_{0.17}Al_{0.83}N$  that is perfectly lattice-matched to *GaN*. This makes it possible to grow a thick epi-layer of material for making devices. Nonetheless, the inhomogeneity associated with this alloy creates another impediment toward the realization of high performance III-nitrides. In the following sections, we will discuss these challenges in detail.

### 1.3.1 Large Effective Mass

The electron effective mass,  $m^*$ , directly impacts the intensity of ISBT. Through equation 1.1, we can see how the ISBT strength between 2 confined states inside the QW varies inversely with effective mass.

$$f_{nn'} = \frac{2}{m^* \hbar \omega_{n'n}} |\langle n | p_z | n' \rangle|^2 \quad (1.1)$$

where  $\hbar \omega_{n'n}$  is the energy difference between states  $|n\rangle$  and  $|n'\rangle$  and  $|\langle n | p_z | n' \rangle|$  is the momentum matrix element.

The electron effective mass in *GaN* ( $m^*$ ) is  $0.2m_0$ , where  $m_0$  is the free electron mass. This effective mass is quite large relative to the arsenides, where  $m_{GaAs}^*$  is  $0.067m_0$ . Hence, at a given doping level, we observe a weaker ISBTs signal in nitrides than in arsenides. This challenge leads to a requirement of heavy Si doping in nitride heterostructures, usually more than  $10^{18}$  atom/cm<sup>3</sup>. In a later chapter, we will discuss the consequences of this heavy doping requirement on ISBT energy and linewidth, which have profound implications for the performance of devices.

### 1.3.2 Internal Polarization Field

Nitride alloys can exist as two distinct types of crystalline structure, namely wurtzite and zinc-blende. Figure 1.1 represents the wurtzite structure of *GaN*, where *Ga* is shown in red.

All of the nitride alloys discussed in this document take the wurtzite structure. The metal-nitrogen bond is asymmetric, causing an electric dipole moment pointing from nitrogen to the metal atom. The net effect of these dipoles is called spontaneous polarization. Another type of self-polarization, results from lattice strain, whereby the charge density is modified along the growth direction. This strain induced polarization is referred to as piezoelectric polarization. The total internal polarization field  $\vec{P}_{internal}$  is the sum of these two polarizations. However, it should be noted that each alloy has a unique value of  $\vec{P}_{internal}$ . Therefore, at the interface of each heterojunction, there would be an accumulation of charge. This layer of charge affects the shape of the energy band edge. For example, in a c-plane heterostructure, both spontaneous polarization and piezoelectric point along the c-axis; thus,  $\vec{P}_{internal}$  in c-plane  $AlGaN/GaN$  is larger than for other directions (i.e., m-plane heterostructures). Hence, for a c-plane heterojunction, there is a larger buildup of charge at the interface, resulting in an asymmetric QW and barrier (again, compared to an m-plane heterojunction of the same alloy). The asymmetric QW reduces the overlap of the wavefunctions between states and thus diminishes the ISBT rate. Figure 1.2 shows the asymmetric and symmetric QWs ( $GaN$ ) with the confined wavefunctions in the ground state and the first excited state. We can see clearly that the overlap of wavefunctions in Figure 1.2a is smaller than in Figure 1.2b that corresponds to a different transition rate between the two growth directions given the same QW and barrier widths.

Fortunately, a lattice-matched  $InAlN/GaN$  of 17% In is an alternative to reduce the internal polarization field. Figure 1.3 shows the difference in internal polarization field strength between  $Al_{0.83}Ga_{0.17}N/GaN$  and lattice-matched  $In_{0.17}Al_{0.83}N/GaN$ . Due to the perfect lattice-matched condition of 17% In of  $InAlN$ , there is no contribution to polarization from piezoelectric effect. Figure 1.3 also shows the energy levels of the ground state and the first excited state of each QW. Nonetheless, as mentioned earlier, the ISBT energy can be tailored by the width of the QW. Therefore, the difference in  $E_{21}$  in this case is non-trivial and controllable.

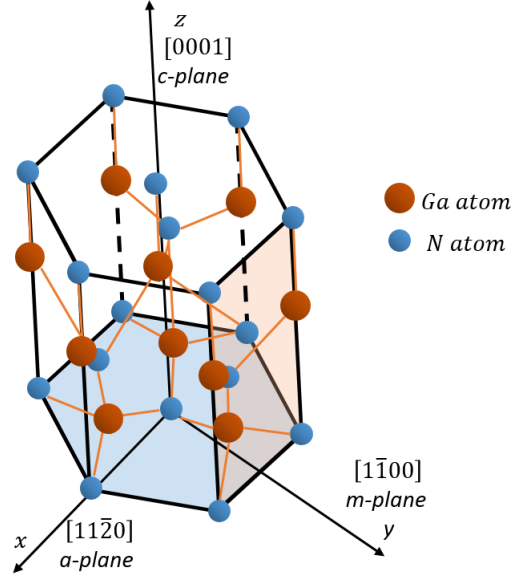


**Figure 1.1.** Wurtzite structure of  $GaN$ , where x-, y-, z-directions are normal to a-, m-, c-planes, respectively.

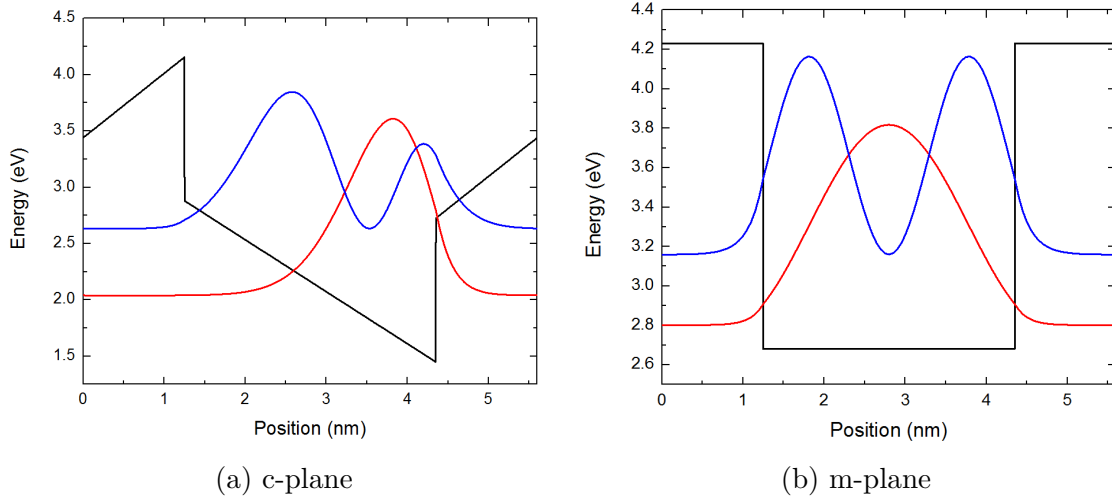


**Figure 1.2.** Conduction band edge and probability amplitudes of the ground state and the first excited state of  $Al_{0.85}Ga_{0.15}N/GaN$  in (a) polar c-plane direction and (b) non-polar m-plane direction with the well of 2.5 nm and the barrier of 3.1 nm.

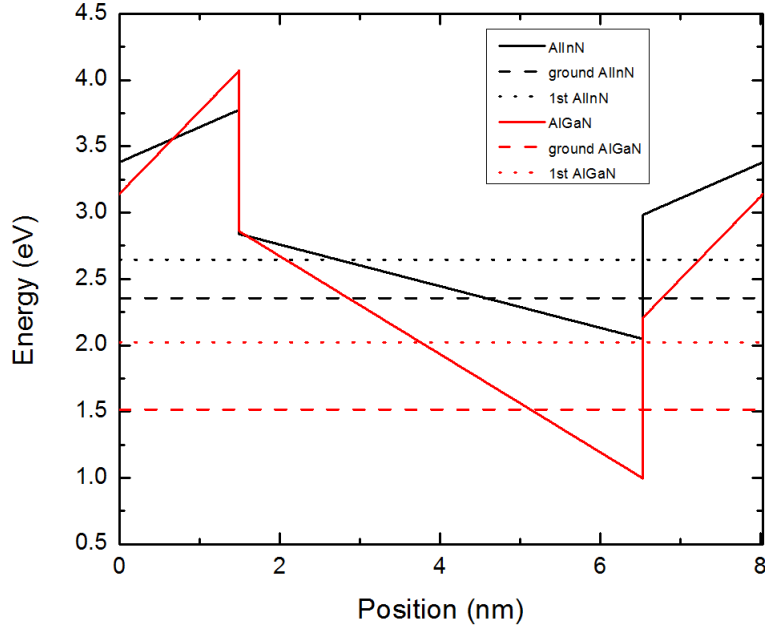


**Figure 1.3.** Conduction band edges and energy levels of the ground state and the first excited state of c-plane  $Al_{0.83}Ga_{0.17}N/GaN$  and  $In_{0.17}Al_{0.83}N/GaN$  undoped heterostructures with the well of 5nm and the barrier of 3.03 nm.

### 1.3.3 Defects and Inhomogeneity

C-plane  $GaN$  is often grown on a sapphire substrate. A thin film of  $GaN$  grown on c-plane sapphire was found to have many types of dislocation defects, including screw, edge, and mixed. The lowest dislocation density in  $GaN$  grown on sapphire c-plane is around  $10^8$  atom/cm<sup>2</sup> by the lateral overgrowth method [12]. The defect density is greatly reduced by replacing a pure sapphire substrate with one consisting of a sapphire base underlying a thick  $GaN$  layer grown by hydride vapor phase epitaxy [13]. The m-plane samples are grown on commercially available free-standing  $GaN$  substrates [14], that usually have a defect density 2 orders of magnitude smaller than c-plane substrates ( $10^5 - 10^6$  atom/cm<sup>2</sup>). However, thin film  $GaN$  grown on a non-polar m-plane substrate is found to have high density stacking faults (planar defects). These defects are formed at the interface of  $GaN$  and the substrate and propagate along the growth direction [12]–[16].

Quantum confinement is achieved at the interface between dissimilar materials, for example,  $AlGaIn/GaN$ . Due to the lattice mismatch between  $AlGaIn$  and  $GaN$ , there are

also strain-generated defects in the QWs and barriers. Moreover,  $AlGaN$  and  $GaN$  do not have a lattice-matched alloy composition. Thus, this combination of alloys is not ideal for growing a thick active region for complex devices.

An alternative solution to the lattice-matching challenge is  $In_{0.17}Al_{0.83}N/GaN$ . This alloy is exactly lattice matched to  $GaN$  along the  $a$ -axis, enabling the growth of a thick layer of active region. However, the unique nanostructures of this material dramatically affect its homogeneity and, therefore, the ISBTs rate of multiple quantum wells (MQWs). We will discuss this matter in a chapter 7, including evidence from scanning transmission electron microscopy (STEM) images and the optical measurements from FT-IR spectroscopy.

Another replacement of  $AlGaN/GaN$  heterostructures is strained-balanced  $(In)AlGaN/InGaN$ . Although, there is strain between these materials, we are able to grow MQWs at nearly strain-balanced conditions leading to the possibility of growing a thick active region for devices. These superlattices (SLs) show good absorption spectra with a small full-width-half-maximum (FWHM) that makes them promising for optoelectronic applications. In chapter 6, we will also discuss the limitations of this semiconductor combination in ISBA energy.



## 2. INTERSUBBAND TRANSITIONS THEORY

In this chapter, we discuss the theory of ISBTs and its corrections. As previously mentioned, most optoelectronic devices rely on interband transitions, where electrons and holes recombine across the band gap. Thus, a limit is imposed on the range of wavelengths to which these devices respond. In devices using ISBTs, optical absorption promotes electrons from the ground state to the first excited state in the conduction band instead of across the band gap, thereby greatly increasing the range of operation. ISBTs are of great interest due to their potential applications and the flexibility they provide in designing structures. Various alloy compositions result in different conduction band edge profile, or commonly referred to as CBO, and the QW width dictates the transition energy ( $E_{transition} \approx \frac{1}{L^2}$ ). Figure 2.1 shows schematically the fundamental difference between interband transitions and ISBTs as well as the relationship between transition energy,  $E$ , and the QW width,  $L$ . In practical experiments, the intersubband absorption (ISBA) from a single QW is too small to detect. Hence, the heterostructures are usually built of multiple layers of wells and barriers, forming a so-called MQW system.

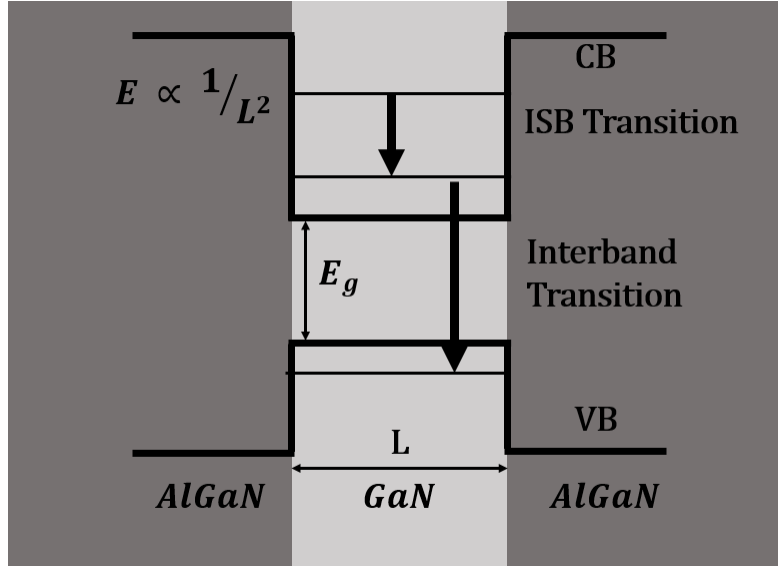


**Figure 2.1.** The difference between interband and ISBTs in a single non-polar m-plane *AlGaIn/GaN* quantum well system.

## 2.1 Intersubband Absorption Coefficient

We start with the simplest model of Schrodinger equation for an electron inside a QW with infinite barriers

$$\left( \frac{p^2}{2m_0} + V(r) + V_s(r) \right) \psi(r) = E\psi(r) \quad (2.1)$$

where  $V(r)$  is the lattice potential and  $V_s(r)$  is the potential from the (superlattice) heterostructure. The wavefunction of the electron is calculated using the envelope-function approach in the effective-mass approximation [17]

$$\psi_i(r) = f_i(r)u_v(r) \quad (2.2)$$

where  $\psi_i(r)$  is the electron wavefunction inside band ( $v$ ),  $f_i(r)$  is the normalized envelope function with quantum number  $i$ , and  $u_v(r)$  is the normalized Bloch function in band  $v$ .

From equation 2.1, we notice the  $V_s(r)$  term has only 1 non-zero component along the growth direction, namely  $z$ . Hence, the electron freely moves in the  $x$  and  $y$  directions, and we will focus only on the growth direction to solve the Schrodinger equation. The envelope wavefunction and the Schrodinger equation along  $z$ -direction can be written as

$$f_i(r) = \frac{1}{\sqrt{A}} e^{i\vec{k} \cdot \vec{r}} \phi_i(z) \quad (2.3)$$

$$\frac{-\hbar^2}{2m^*} \frac{d^2 \phi_i(z)}{dz^2} + V_s(r) \phi_i(z) = E_i \phi_i(z) \quad (2.4)$$

where  $A$  is the surface area of the quantum well in the  $xy$ -plane,  $\vec{k} = \langle k_x, k_y, 0 \rangle$  is in-plane wave-vector. Notice that we do not use the electron mass ( $m_0$ ), but rather the electron effective mass ( $m^*$ ) due to the approach mentioned above. Then, the solution to the Schrodinger equation from equation (2.4) is given by

$$E_i(k) = E_i + \frac{\hbar^2 k^2}{2m^*} \quad (2.5)$$

where  $E_i = \frac{i^2 \hbar^2 \pi^2}{2m^* L^2}$  is the confined energy of the electronic states inside the infinite quantum well of width  $L$ , and the second term is the solution from the plane wave. Now it is clear how the ISBT energy can be engineered by changing the structure of the material.

Next, we make use of Fermi's golden rule to calculate the ISBA coefficient. Recall from quantum mechanics, the transition rate from state i to state f is given as

$$W_{if} = \frac{2\pi}{\hbar} |\langle \psi_i | H' | \psi_f \rangle|^2 \delta(E_f - E_i - \hbar\omega) \quad (2.6)$$

where  $H' = \frac{e}{2m^*} (\vec{A} \cdot \vec{p} + \vec{p} \cdot \vec{A})$  represents the interaction between an electron and the external electromagnetic field,  $\vec{A}$  is vector potential ( $-\frac{\partial \vec{A}}{\partial t} = \vec{E}$ ). Since  $\vec{E}$  is the electric field of an incident light ray that is linearly polarized;  $\vec{E}$  can be written as

$$\vec{E} = E_0 \vec{s} \cos(\vec{q} \cdot \vec{r} - \omega t) \quad (2.7)$$

where  $\vec{s}$  is the polarization unit vector. Hence, the transition rate from state i to state f becomes

$$W_{if} = \frac{2\pi}{\hbar} \frac{e^2 E_0^2}{4m^{*2} \omega^2} |\langle i | \vec{s} \cdot \vec{p} | f \rangle|^2 \delta(E_f - E_i - \hbar\omega) \quad (2.8)$$

$$\langle i | \vec{s} \cdot \vec{p} | f \rangle = \vec{s} \cdot \langle u_{v_i} | \vec{p} | u_{v_f} \rangle \langle f_i | f_f \rangle + \vec{s} \cdot \langle u_{v_i} | u_{v_f} \rangle \langle f_i | \vec{p} | f_f \rangle \quad (2.9)$$

Notice that the first term on the right hand side of equation 2.9 describes the interband transition with an overlap integral of the envelope function. However, we are interested in ISBTs. Hence, this term vanishes. Moreover, the second term in equation 2.9 represents the ISBT; and  $\langle u_{v_i} | u_{v_f} \rangle = 1$  due to the normalization of  $u_v$ . Therefore,  $\langle f_i | \vec{p} | f_f \rangle$  defines the ISBT from subband i to f inside band  $\nu$ .

The ISBA coefficient is defined as the ratio of the intensity of the absorbed electromagnetic (EM) wave to the intensity of the incoming wave. The intensity of the absorbed EM wave is calculated as the absorbed EM energy per unit time per unit volume,  $I_{ab} = \frac{\hbar\omega W_{if}}{V}$ . In our case, we consider a 2D electron gas (2DEG); instead of volume, we will use the area of the 2DEG, A. The intensity of the incident radiation is calculated as  $I_{in} = \frac{1}{2} \epsilon_0 c \eta E_0^2$ ; where

$\eta$  is the refractive index,  $\epsilon_0$  is the vacuum permittivity, and  $c$  is the speed of light. Hence, the ISBA coefficient is given as

$$\begin{aligned}\alpha_{ISB} &= \frac{I_{ab}}{I_{in}} \\ &= \frac{2\hbar\omega W_{if}}{A\epsilon_0 c\eta E_0^2} \\ &= \frac{\pi e^2}{\epsilon_0 c\eta\omega m^* A} |\langle f_i | \vec{p} | f_f \rangle|^2 \delta(E_f - E_i - \hbar\omega)\end{aligned}\quad (2.10)$$

Fortunately, with a few assumptions we can derive an explicit expression for  $\alpha_{ISB}$  in the case of a 2DEG as

$$\begin{aligned}\alpha_{ISB} &= \frac{\pi e^2}{\epsilon_0 c\eta\omega m^* A} \sum_{i,f} \int A \frac{2}{(2\pi)^2} d^2k \left( \frac{1}{1 + e^{(E_f - E_F)/kT}} - \frac{1}{1 + e^{(E_i - E_F)/kT}} \right) \\ &\quad |\langle f_i | \vec{p} | f_f \rangle|^2 \frac{\Gamma/2\pi}{(\hbar\omega_p - \hbar\omega)^2 + (\Gamma/2)^2}\end{aligned}\quad (2.11)$$

where the integral is from the Fermi-Dirac distribution of a 2DEG,  $E_F$  is the Fermi energy of the material, and  $k$  is Boltzmann's constant. The factor of 2 comes from the spin of the electron.  $\int d^2k \frac{A}{(2\pi)^2} \left( \frac{1}{1 + e^{(E_f - E_F)/kT}} - \frac{1}{1 + e^{(E_i - E_F)/kT}} \right)$  comes from the difference in the Fermi-Dirac distribution of states  $i$  and  $f$ , and  $\frac{\Gamma/2\pi}{(\hbar\omega_p - \hbar\omega)^2 + (\Gamma/2)^2}$  is an empirical Lorentzian linewidth replacing the  $\delta$  function. We will discuss this broadening factor in a later section.

In practical terms, the absorption from a single quantum well is too small to detect. Thus, the sample is usually composed of a heterostructure of MQWs. For certain optical measurement techniques, to enhance the ISBA, the sample is polished on both sides and the back, while it is unnecessary for other methods. More details of the sample preparation process of different methods will be discussed in the later sections. The purpose of side polishing is to create facets where incident light undergoes multiple passes by bouncing between the front and the back of the sample through the active region as in Figure 2.2.

The ISBA only occurs when the incoming electric field,  $\vec{E}$ , is coincident with the growth direction,  $z$ . This orientation of the incident EM wave is called p-polarization. Experimental measurement of transmission from the s-polarized light, where  $\vec{E}$  is perpendicular to the

growth direction, is useful as background information. Quantitatively, the transmission through such a waveguide can be calculated as

$$T \approx \exp\left[-C \cdot m \cdot N \cdot \alpha_{ISB} \cdot \frac{\sin^2\theta}{\cos\theta}\right] \quad (2.12)$$

where  $m$  is the number of passes through the active region,  $N$  is the number of QWs,  $\theta$  is the angle between the incident light and the growth direction, and  $C$  is the coupling factor representing the overlap of the standing wave of  $\vec{E}$  and the active region. The value of  $C$  is in the range of 0 to 2.

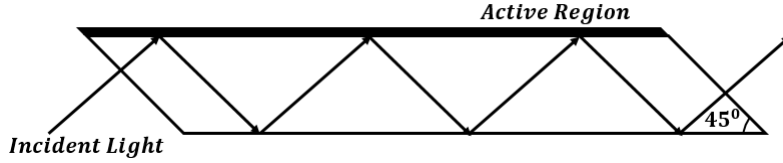


**Figure 2.2.** 45° facets multi-pass waveguide used for ISBA.

## 2.2 Many-Body Effects

Polar and non-polar III-nitride heterostructures are of great interest due to their wide range of applications. However, a high charge concentration level of  $10^{12}$  particle/cm<sup>2</sup> is required to observe light absorption in these structures. Many body effects become non-trivial at impurity density higher than  $10^{12}$  particle/cm<sup>2</sup>. Moreover, there are other corrections that have been shown to contribute to the total correction of transition energy due to the high density of charge; these include depolarization and many body exciton (excitonic) corrections [18]. Figure 2.3 shows the many-body effects on ISBA energy of a non-polar m-plane *AlGa*N/*GaN* MQWs, including exchange energy calculated using HFA method, depolarization shift, and excitonic interaction correction. In this section, we will discuss in detail each energy correction term.

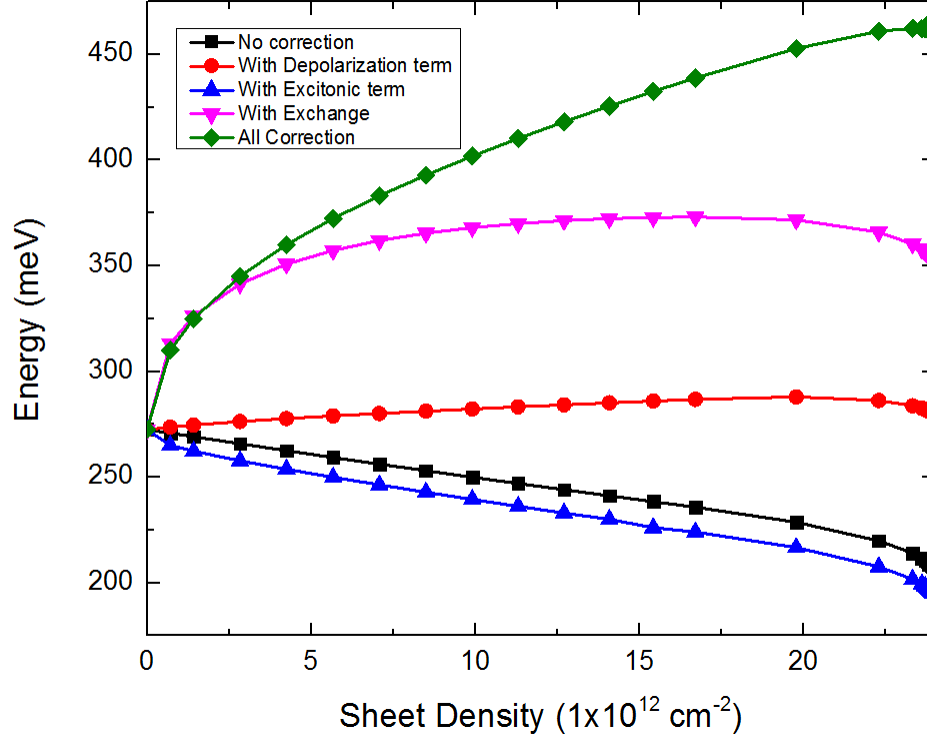


**Figure 2.3.** The effect of many body corrections on the ISBT energy as a function of sheet charge density for 3.2 nm thick *GaN* QWs and 2.05 nm thick barriers with non-polar m-plane  $Al_{0.56}Ga_{0.44}N$ . This calculation was done using the HFA correction.

### 2.2.1 Exchange-Correlation Correction

Let us re-write the Schrodinger equation for a single electron moving through an electron gas in different style from equation 2.1 as

$$\left(\frac{-\hbar^2}{2m^*}\nabla^2 + V(\vec{r})\right)\psi_i(\vec{r}) + V_{xc}\psi_i(\vec{r}) = E_i\psi_i(\vec{r}) \quad (2.13)$$

where  $(\frac{-\hbar^2}{2m^*} + V(\vec{r}))$  comes from the one-electron model that includes the kinetic energy term and the external potential (e.g., the potential of the nucleus), and the  $V_{xc}$  is the exchange-correlation potential. The exchange-correlation potential describes how one electron avoids another when it moves through the electron sea [19]. There are different types of exchange interaction, including direct exchange, indirect exchange, and super exchange [20]. However, in the case of small interatomic distances, only the direct exchange would contribute to the

energy shift of the ISBTs through the interaction of one electron with its neighbors, causing an anti-parallel alignment of the electronic spin (i.e., the Pauli exclusion principle). Hence, the consequence of this phenomenon is to lower the energy state. The correlation energy comes from the Coulomb repulsion of one electron with another [19]. We will discuss in further detail how the exchange and correlation energies are calculated using different methods, namely the Hartree-Fock approximation (HFA) and the local density approximation (LDA) below.

### Hartree-Fock Approximation

HFA is an improvement of the Hartree method by adding the interaction of one electron with another with the opposite spin [21]. With the Hartree method, equation 2.13 becomes

$$\left(\frac{-\hbar^2}{2m^*}\nabla^2 + V_{nucleus}(\vec{r}) + V_e(\vec{r})\right)\psi_i(\vec{r}) = E_i\psi_i(\vec{r}) \quad (2.14)$$

where  $m^*$  is the effective mass of the electron,  $V_{nucleus}$  describes the interaction of one electron and the nucleus as that electron moves and the  $V_e$  represents the e-e interaction through Coulomb repulsion. Notice that in equation 2.14, the exchange interaction between two electrons with opposite spins was not included. This term was included in the Hartree-Fock method as a correction to the total energy of the electron. The interaction terms are distinct from the kinetic energy, lattice potential, impurity potential, and external field potential as shown in equation 2.15 below [22]

$$\begin{aligned} \frac{-\hbar^2}{2m^*}\nabla^2\psi_m(\vec{r}) + V(\vec{r})\psi_m(\vec{r}) + U^{ion}(\vec{r})\psi_m(\vec{r}) + \sum_n \int d\vec{r}' \frac{e^2}{4\pi\epsilon_0\epsilon_r|\vec{r}-\vec{r}'|} \\ - \sum_n \int d\vec{r}' \frac{e^2}{4\pi\epsilon_0\epsilon_r|\vec{r}-\vec{r}'|} \psi_n^*(\vec{r}')\psi_m(\vec{r})\delta_{s_m,s_n} = E_m\psi_m(\vec{r}) \end{aligned} \quad (2.15)$$

where  $m^*$  is the effective mass of the electron,  $\epsilon_0$  is the vacuum permittivity,  $\epsilon_r$  is the dielectric constant of the QW material,  $\psi(\vec{r})$  is the wavefunction of the electron,  $V(\vec{r})$  is a combination of lattice potential and external field, and  $U^{ion}(\vec{r})$  can also be looked at as a doping profile. The two sums in equation 2.15 represent the direct Coulomb and exchange interactions,

respectively. As mentioned previously, in a highly doped system, the contribution from the exchange interaction dominates the Coulomb interaction [22]. Thus, we will focus on the exchange term only. The negative sign reflects the anti-parallel spins. The exchange term vanishes unless the spins in states  $m$  and  $n$  are identical, following the Kronecker  $\delta$ .

Bandara et al. calculated the electron energy from equation 2.15 in separate steps. First, the Schrodinger equation of one electron, excluding the exchange-correlation effect, is solved by solving the Poisson equation with two boundary conditions. The first boundary condition states that “charge neutrality prevails in each unit cell of MQW”; and the second boundary condition says that “all donors do not freeze out even when the temperature is extremely low” (0 K) [18]. The exchange energy is calculated using the result from solving the one-electron Schrodinger equation previously. Consider the exchange interaction between electrons in the ground state subband of a MQW system, the exchange term from equation 2.15 becomes

$$\Delta E_{1 \rightarrow 2, ex} = \frac{-e^2}{2\epsilon_0\epsilon_r} \int_0^{k_F} \frac{d^2 k'}{(2\pi)^2} \int dx \int dx' \frac{e^{-q|x-x'|}}{q} |\psi_0(x')|^2 |\psi_0(x)|^2 \quad (2.16)$$

where  $k_F$  is the Fermi wavevector,  $q = |k - k'|$ ,  $x$  is the orthogonal coordinate to the QW, and  $\psi_0(x)$  is the wavefunction of a single electron in the ground state. With the assumption that  $\psi_0(x)$  is strongly localized inside the QW, only the first two terms from Taylor’s expansion are required to approximate the exponential. The negative sign causes a significant blue shift in the transition peak.

While HFA calculates the exact exchange energy, it neglects details of the correlation energy calculation. Since, the electron wavefunction in HFA is approximated by a single Slater determinant which does not take into account the Coulomb repulsion, the total electron energy calculated by HFA is always higher than the observed energy [21], [23]. Other than Banrada et al. [22], Manasreh et al. [24] also overestimated the exchange interaction derived from the Schrodinger equation while neglecting the correlation interaction [18].

## Local Density Approximation

In contrast to HFA, LDA is the first step in density functional theory that uses the approximated local density (i.e., the electron density of the system is uniform everywhere)



to explain the effect of many-body instead of the wavefunction. With the LDA, we consider the total energy functional of an electron as [19]

$$E_0[n] = T_s[n] + \int d^3r n(\vec{r})v(\vec{r}) + U[n] + E_{xc}^{LDA}[n] \quad (2.17)$$

where  $T_s[n] + \int d^3r n(\vec{r})v(\vec{r}) + U[n]$  comes from the Hatree approximation without self-interaction correction, and  $E_{xc}^{LDA}[n]$  is the exchange-correlation energy functional. The exchange-correlation correction is calculated as [19], [25]

$$E_{xc}^{LDA}[n] = \int d^3r n[\vec{r}] \epsilon_{xc}^{uniform}(n[\vec{r}]) \quad (2.18)$$

where  $\epsilon_{xc}^{uniform}(n)$  is the exchange-correlation energy per electron in a gas of electrons with uniform density  $n$ . Using the Hohenberg-Kohn and Kohn-Sham theories, the exchange-correlation potential term was obtained within the LDA by Hedin and Lundqvist as [18], [25]–[27]

$$V_{xc}(n(z)) = \frac{-2}{r_s} \left( \frac{9}{4\pi^2} \right)^{1/3} \frac{e^2}{8\pi\epsilon_0\epsilon_r a^*} \left[ 1 + 0.7734 \frac{r_s}{21} \ln \left( 1 + \frac{21}{r_s} \right) \right] \quad (2.19)$$

where  $r_s = \sqrt[3]{\frac{3}{4\pi(a^*)^3 n(z)}}$  is a dimensionless parameter and  $a^* = \frac{4\pi\epsilon_0\hbar^2}{m_0 e^2 \frac{\epsilon_r}{m^*/m_0}}$  is the effective Bohr radius. The observed exchange-correlation energy is then simply calculated by integrating the energy functional over the whole space.

### 2.2.2 Depolarization Correction

In a many-body system, an individual electron is polarized not only by the external radiation, but also by its neighbors. As the EM waves strike the surface of the active region, local electrons are polarized. Hence, each electron feels not only the external field, but also the depolarization of the other electrons. In other words, the external electric field has two important effects on the free charges of the system. It promotes electrons from a lower state to a higher state through an electron excitation process. The external field also modulates the charge density of the material.

From one electron theory, the transition occurs when the photon energy,  $\hbar\omega$ , is the same

as the energy difference between the ground state and the first excited state of the subbands. However, this is not the case for a thin film of dielectric material [28]. The factor  $\alpha$  accounts for the depolarization shift and can be calculated as

$$\alpha = \frac{2e^2 n_s}{\epsilon_0 \epsilon_r E_{21}} \int_{-\infty}^{\infty} dz \left( \int_{-\infty}^z dz' \psi_0(z') \psi_1(z') \right)^2 \quad (2.20)$$

where  $E_{21}$  is the corrected transition energy from the exchange-correlation calculated in section 2.2.1,  $\psi_0$  and  $\psi_1$  are wavefunctions of the ground state and the first excited state, and  $n_s$  is the charge density of the 2DEG.  $\epsilon_0$  and  $\epsilon_r$  are vacuum permittivity and dielectric constant, respectively. The integral represents the squared frequency shift that has the unit of length. As equation 2.20 suggests, this correction becomes non-trivial with either high sheet charge density or low absorption energy. We will show in the next section the role of this factor,  $\alpha$ , in the shift of the ISBT energy along with the excitonic shift.

### 2.2.3 Excitonic Correction

The excitonic term originates from the recombination of the excited electron and the quasi-hole left behind in the ground state. This correction is named in analogy to the electron-hole pair across the band gap in excitons. The exchange-correlation potential term is approximated as equation 2.19. In order to have good agreement with experimental results, Bloss and Jogai [18], [27] applied the local density approximation to formulate the exciton and depolarization shift of the ISB transition energy as

$$E_{correction} = E_{21} \sqrt{1 + \alpha - \beta} \quad (2.21)$$

where  $\alpha$  is the factor accounting for the depolarization shift derived from section 2.2.2, and  $\beta$  is a dimensionless factor describing the excitonic shift. This new factor,  $\beta$ , is calculated as

$$\beta = \frac{-2n_s}{E_{21}} \int_{-\infty}^{\infty} dz \psi_2(z)^2 \psi_1(z)^2 \frac{\partial V_{xc}(n(z))}{\partial n(z)} \quad (2.22)$$

Following from equation 2.21, we notice that the excitonic shift introduces a negative change in energy. For a small effective mass,  $\beta \ll \alpha$ , but for a larger effective mass, the two are

comparable. In the case of the nitrides,  $\beta$  is about an order of magnitude smaller than  $\alpha$ . Hence, as we can see in Figure 2.1, the excitonic shift is weak relative to the depolarization shift and the exchange-correlation effect.

### 2.3 Linewidth Broadening

Linewidth broadening is an important parameter in the operation of optoelectronic devices. For example, the smaller the full-width-half-maximum,  $\Gamma$ , the higher the optical gain in QCLs. The line broadening is due to several mechanisms, including electron and phonon scattering, interface roughness, and non-parabolicity. On the other hand, the FWHM of the ISBA peak can be calculated based on both inelastic and elastic scattering. It is obtained as

$$\Gamma = \hbar \left( \frac{1}{2\tau_{inelastic}} + \frac{1}{\tau_{elastic}} \right) \quad (2.23)$$

where  $\Gamma$  is the FWHM of the ISB absorption peak,  $\tau_{inelastic}$  is mean scattering time for inelastic collisions, and likewise  $\tau_{elastic}$  is the scattering time of elastic collisions.

In more detail, phonon scattering is inelastic. The electron needs to have an energy of  $E_{LO}$  in order to emit an optical phonon. For a narrow QW, that means  $E_{21} > E_{LO}$ , the LO phonon scattering is non-trivial. It becomes the main contribution to total relaxation. However, for a wide QW ( $E_{21} < E_{LO}$ ), the FWHM depends on several mechanisms including phonon scattering, impurity scattering, alloy disorder, etc.[17]

The elastic scattering can be due to impurity scattering or interface roughness scattering. Impurity scattering represents the interaction between electrons and ionized donor atoms. The strength of this mechanism depends on the spatial overlap of electron wavefunctions inside the QW and the doping profile. This type of scattering is quite effective due to the small relaxation time [17]. In addition, interface roughness broadening has both long range and short range components. The long range roughness broadening is caused by the wide spread of ISB transition energies due to structures with various QW widths; while the short range broadening is due to the interaction between electrons traveling in the QW and the interface (related to the electron mobility inside the well). Alloy disorder scattering originates from the random distribution of atoms (Al, In, and Ga) in the alloys, providing

a perturbation in the crystal potential. Nonetheless, a high doping level is also required to observe light absorption in these heterostructures, and therefore impurity scattering becomes the major contribution to the total relaxation [29] ( $> 70\%$  of total linewidth broadening) in either delta doping or continuous doping in well and barrier.

## 2.4 Intersubband Transitions in III-Nitride Heterostructures

III-nitride semiconductors such as  $AlN$ ,  $GaN$ , and  $InN$ , as well as their alloys, have been effectively exploited in ultraviolet and visible optoelectronic devices, with significant societal impact [1]–[6]. Additionally, they have lately attracted attention as promising materials for infrared (IR) intersubband (ISB) devices (1.5–60  $\mu\text{m}$ ) [11], [30]–[36]. Nitride materials are ideal for usage in IR devices due to their large and broadly tunable CBO, high longitudinal optical phonon energy (92 meV), and sub-picosecond ISB relaxation durations [30], [35]. Over the last decade, the majority of research on nitride intersubband transitions has concentrated on c-plane heterostructures [37]–[39]. However, due to the asymmetric quantum wells (QWs) produced by the strong built-in polarization forces along the c-axis [40], these materials present difficulties for application in practical nitride infrared optoelectronics. Fortunately, the symmetry of the wurtzite crystal allows for the growth of nitride heterostructures in the nonpolar ( $10\bar{1}0$ ) direction, also known as the m-plane direction, which totally eliminates built-in polarization fields.

In recent decades, there have been several reports of the ISBA of polar c-plane  $AlN/GaN$  in infrared range (1.0–3.5  $\mu\text{m}$ ) [41]–[50]. Tchernycheva et al. reported in reference [51] the ISBA energy of polar  $AlN/GaN$  MQWs in the range of 640–932 meV (1.32–1.9  $\mu\text{m}$ ) with FWHMs of 70–100 meV. Guillot et al. reported an ISBA energy at 866 meV with a record FWHM of 40 meV from an unintentionally doped  $AlN/GaN$  MQW, resulting in weak absorption [42]. However, growing thick structures with highly strained  $AlN/GaN$  heterostructures for application purposes is not practical because the material eventually cracks. Alternatively, to reduce strain in this material combination,  $AlN$  can be substituted with  $AlGaIn$ . The ISBA energy of polar  $AlGaIn/GaN$  with a variation of QW thickness can approach 10  $\mu\text{m}$  [52]. Additionally, high doping levels are required for strong ISBA for nitrides. However,

this not only increases ISBA energy substantially due to many body effects explained in section 2.2, but also broadens the ISBA curve due to the impurity scattering discussed in section 2.3.

Polar III-nitride heterostructures have internal (spontaneous and piezoelectric) fields that make it difficult to build high-performance ISB devices. One way of eliminating this internal electric field is to grow these MQW structures on non-polar planes like m- and a-planes [34]. However, the lattice mismatch along the c-axis is greater than along the a-axis, resulting in a high defect density in these semiconductors and hindering the formation of atomically flat surfaces during growths [35]. Lim et al. reported that non-polar m-plane  $AlGaN/GaN$  heterostructures show better ISBA results (i.e. smaller FWHMs) than a-plane  $AlGaN/GaN$  [36], [53]. On m-plane  $AlGaN/GaN$  MQWs grown by plasma-assisted molecular beam epitaxy (PA-MBE), we obtained far- and mid-IR ISBA [32], [54], [55]. Monavarian et al. recently measured ISB transitions in m-plane  $AlGaN/GaN$  produced with ammonia MBE with a record-narrow linewidth of 38 meV at 224-274 meV (4.5-5.5  $\mu m$ ) [56]. However, due to the large lattice mismatch between the component materials, the  $AlGaN/GaN$  system is not scalable to thick devices. Additionally, an unanticipated problem developed during the development of  $AlGaN$  with a high  $Al$  mole percentage on the m-plane [11], [57], [58]. We discovered that PA-MBE development of  $AlGaN$  on m-plane  $GaN$  is unstable, preventing the synthesis of planar, homogenous  $AlGaN$  alloys with a composition of more than 60%  $Al$  [11], [32]. To address these limitations, we examine non-polar m-plane near strain-balanced  $(In)AlGaN/InGaN$  superlattices. For the first time, the measured ISBTs of  $(In)AlGaN/InGaN$  MQWs were reported in the range of 3.4-5.1  $\mu m$  with FWHMs comparable to those reported in the literature for m-plane  $AlGaN/GaN$  heterostructures [59]. Theoretical calculations suggest that the ISBA energies of these superlattices are extremely sensitive to the choice of CBO. More research is required to fully understand the CBO of this material combination for more accurate prediction of the ISBA energy.

### 3. TRANSMISSION ELECTRON MICROSCOPY

#### 3.1 Introduction to Transmission Electron Microscopy

The fundamental resolution limit of a microscope is given by the wavelength of radiation. The Table 3.1 lists various types of radiation and their benefits and drawbacks. While both X-ray and electrons provide small wavelengths, electron beams can provide well-focused, high-resolution images that are critical for several different material studies, e.g. defects, material homogeneities, alloy composition (alloy material), etc. In this chapter, we will focus on the electron microscope, which uses electrons as its radiation source.

Transmission electron microscopy (TEM) is a useful technique for the structural study

**Table 3.1.** Advantages and disadvantages of different types of radiation for microscopy applications.

Type of Radiation	Advantages	Disadvantages
Visible light	Not very damaging Easily focused Eye is wonderful detector	Long wavelength
X-rays	Small wavelength Å Good penetration	Hard to focus Damage sample
Electrons	Small wavelength (pm) Can be focused	Damage sample Poor penetration
Neutrons	Low sample damage Small wavelength (pm)	How to produce? How to focus?

of materials that uses electrons as a source of radiation. In 1925, Louis de Broglie proposed that the electron also has wave-like properties [60]. This discovery opened up a new era for applications using electrons and their wave-particle duality. One of those great inventions was the transmission electron microscope by Ernst Ruska and Max Knoll in 1931. The microscope is constructed with an electron gun on top and a vacuum column with several built-in lenses, coils, detectors, and screens to guide the electron beam from the source to the desired screen for collecting images. Figure 3.1 shows the basic TEM anatomy with the path of the electron beam. After being emitted by the filament, the electrons that have a small energy  $\Delta$  then go through the Wehnelt cylinder, resulting in a spatially coherent electron

beam (i.e. all electrons have the same direction) and entering the accelerator stack to gain energy. The accelerator stack consists of a series of disks with a hole in the middle for the beam to pass through. After completely passing through this stack, the electron beam is then precisely controlled and directed using a magnetic field created by a series of coils and lenses to form a desired beam before hitting the specimen and being collected on a specific detector for a specific type of image. The electron's wavelength is inversely proportional to its energy and much smaller than that of visible light. This makes TEM an alternative solution for high resolution imaging techniques compared to visible-light microscopy. In this document, both bulk and heterostructures of nitrides are investigated by different TEM modes, including scanning transmission electron microscopy and energy dispersive x-ray spectroscopy (EDS). However, due to the large error bar, EDS elemental maps are considered a secondary characterization approach and are therefore utilized for qualitative rather than quantitative analysis. Nonetheless, we will also discuss the limitations of TEM due to sample preparation, beam damage, and image interpretation.

Basic TEM imaging depends on the scattering mechanisms between the electron beam and the electrons/nuclei of the specimen through Coulomb interaction, as shown in Figure 3.2. Different measuring techniques collect different types of secondary signal from a wide range of scattering processes. For example, secondary electron images contain information about the specimen's surface topography. (S)TEM uses the signal from the transmitted beam that has structural information about the crystallography of the material. One of the fundamental differences between bright field and dark field images is the origin of the electron beam. A dark field image is a collection of scattered electrons from a diffracted beam or a portion of a diffraction ring, while a bright field image is a collection of electrons from the direct beam. A dark field technique is often used if bright field images are not clear enough. It is also used for crystal lattice and crystal defect studies.

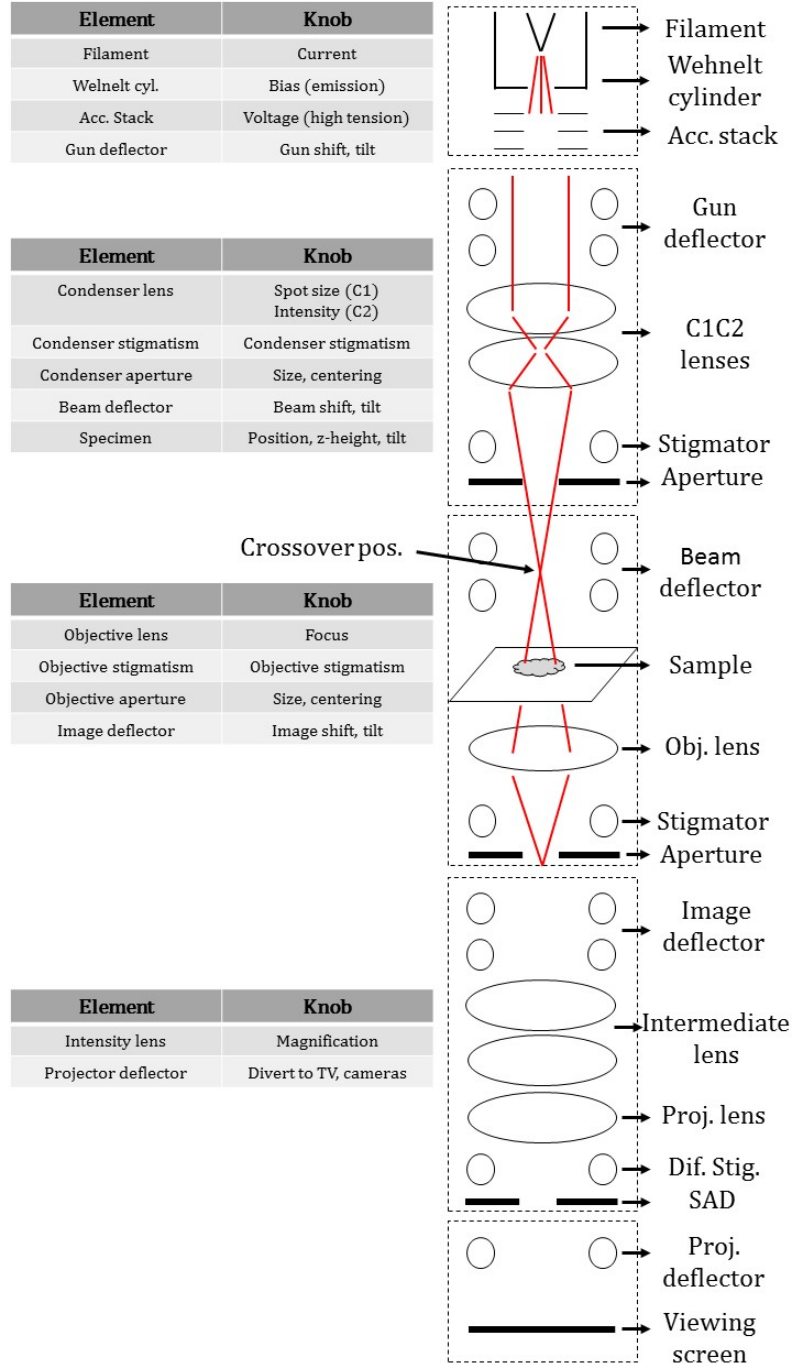


**Figure 3.1.** Basic TEM anatomy including gun, condenser lens system, objective lens system, projector lens system, and viewing screen/detector/camera from top to bottom.

All STEM images in this document were taken with the high-angle annular dark field (HAADF)-STEM method. Images of polar c-plane lattice-matched *InAlN/GaN* samples



were taken using the FEI Talos 200X at 200kV, with STEM resolution (i.e. probe size) of 1.2 Å in diameter. Images of non-polar m-plane  $AlGaN/GaN$  were taken using FEI Titan 80-300 at 300 kV with STEM resolution (i.e. probe size) of 0.136 nm, while images of non-polar m-plane strain-balanced  $(In)AlGaN/InGaN$  were taken using Thermo Scientific Themis Z at 300kV, 0.24 nA, and 0.65 Å probe size. Themis Z allows the images to be corrected up to 3<sup>rd</sup> order of aberration, including astigmatism, spherical, coma, etc. Furthermore, energy-dispersive x-ray spectroscopy was used to perform 1D and 2D elemental maps of desired regions. Due to its large error bar for aluminium, gallium, and indium composition, this method was only used for qualitative information to confirm the existence and ratio of elements grown by the PA-MBE process.

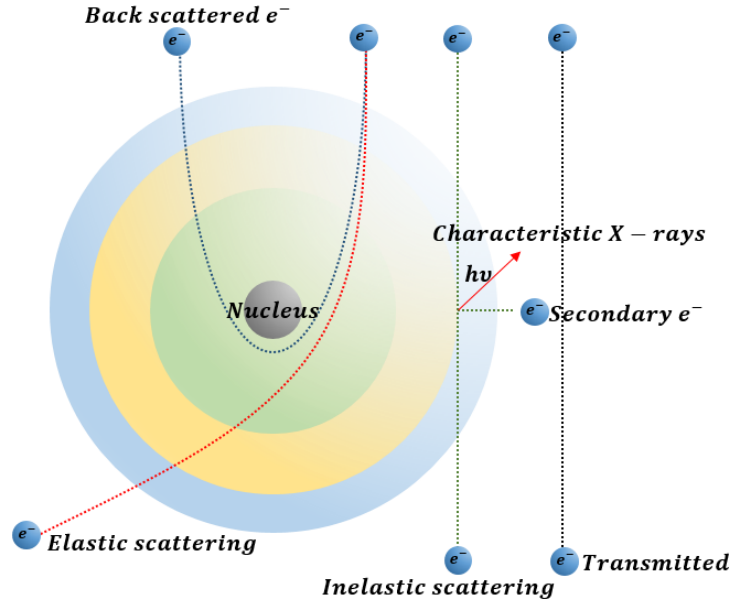


**Figure 3.2.** Different scattering mechanisms in TEM.

### 3.2 Elastic and Inelastic Scattering

As mentioned earlier, TEM images are formed by different electron scattering signals. In this section, we will discuss these mechanisms in more detail. There are several ways of sorting scattering mechanisms into categories. For example, elastic vs. inelastic scattering (if we think of electrons as particles), or coherent vs. incoherent (if we think of electrons as waves), or even back vs. forward scattering (if we want to emphasize the scattered angle of electrons). However, understanding the causes of these phenomena is more important than sorting them in order to gather the information from the images. For simplicity, we will focus on the differences between elastic and inelastic scattering.

Elastic scattering is also known as Rutherford scattering. During this process, the electron interacts with other electrons from the cloud or the nuclei of the sample's atoms through

Coulomb interaction, resulting in no loss of energy. The differential cross section for a scattering event between an electron and a nucleus is given as

$$\begin{aligned}\frac{d\sigma}{d\Omega} &= \left( \frac{e^2 Z_{nucleus}}{4\pi\epsilon_0 E_K} \right)^2 \frac{1}{16\sin^4(\theta/2)} \\ &= \left( \frac{\alpha' \hbar c Z_{nucleus}}{E_K} \right)^2 \frac{1}{16\sin^4(\theta/2)}\end{aligned}\tag{3.1}$$

where  $Z_{nucleus}$  is the atomic number of the nucleus,  $E_K$  is the kinetic energy of the incident electron,  $\theta$  is the scattering angle, and  $\alpha'$  is the fine structure ( $\alpha' = \frac{1}{137}$ ). As we can see in equation 3.1, the scattering cross section is inversely proportional to the electron kinetic energy. This means that a more energetic electron beam would have a smaller scattering angle.

In contrast to elastic scattering, inelastic scattering does not conserve energy. This means that some of the energy from the electron beam is transferred to the specimen, including extra useful secondary signals like secondary electron emission, x-ray emission, etc. However, at certain high energies, the electron beam can cause knock-on and sputtering damage to the specimen, resulting in non-trivial or even deceptive information as the sample chemistry is changed. Some approaches to reducing the amount of energy lost to heat include cooling the specimens and making thinner samples.

### 3.3 Diffraction Patterns

The capability to examine diffraction patterns (DPs) is one of the advantages of the TEM over SEM or visible-optical microscopy. DPs contain crystallographic characteristics including lattice parameters, symmetry, etc., and the type of material, such as crystalline and amorphous materials. Unlike XRD, TEM DPs are formed by electron diffraction. Since high energy electrons can have much shorter wavelengths than x-ray laboratory sources, we are able to have high resolution images at the sub-nanometer scale with TEM. Figure 3.3 illustrates Bragg diffraction inside of a crystal. Images are formed with Bragg diffraction and contain diffraction contrast. We will discuss this type of contrast, along with others, later. In Bragg diffraction, the two incoming beams are scattered from points A and B at

an angle  $\theta$  off the horizontal. Given the distance between the two consecutive planes,  $d$ , the total path difference is

$$\begin{aligned}\Delta l &= CB + BD \\ &= 2d \cdot \sin(\theta)\end{aligned}\tag{3.2}$$

For constructive interference, the total path difference is a multiple of wavelength of the incoming electron,  $\lambda$ . Therefore, equation 3.2 becomes

$$n \cdot \lambda = 2d \cdot \sin(\theta)\tag{3.3}$$

where  $n$  is an integer. In our research, we use TEM DPs to align the electron beam and the specimen. DPs are also used in some cases of sensitive materials to find the location of a specific element or alloy using the information from lattice constants from the patterns.

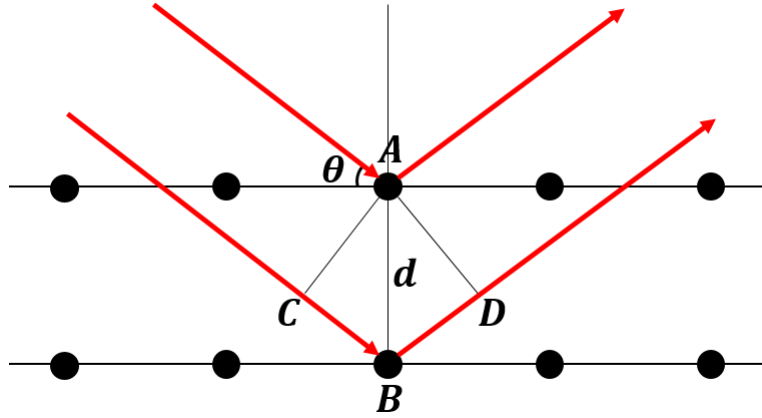


**Figure 3.3.** Bragg diffraction in a crystal.

### 3.4 Amplitude Contrast

Mass-thickness and diffraction contrasts are two types of amplitude contrast. These two types of contrast happen in both TEM and STEM modes during the bright field (BF) and dark field (DF) imaging processes. While diffraction contrast is usually used to find and

study defects in crystals, we often interpret the mass-thickness contrast from the STEM images to study the structure of our samples and explain their effects on optical properties. However, it is not easy to distinguish these two contrasts in the same picture. Hence, STEM images are taken under specific conditions to maximize one type of contrast over the other for a given post-analysis purpose. For example, if we want to study the defects and homogeneity of our material, during the STEM imaging process, we would pick the low diffraction angle electron beam, so that our result would only contain diffraction contrast. Bright field and dark field images are formed by the direct and diffracted beam, respectively. The contrast of the BF and DF images is the opposite of each other.

The mass-thickness contrast originates from Rutherford scattering. As we mentioned in an earlier section, the differential cross section for Rutherford scattering is directly proportional to the atomic number  $Z_{nucleus}^2$ . Moreover, the cross section is also directly related to the sample's thickness [60], meaning that the thicker the specimen, the more elastic scattering. Thus, with a given thickness of specimen, different elements would introduce different cross sections, resulting in a different Z-contrast on the image. For example, the larger  $Z_{nucleus}$ , the stronger the electron scattering, leading to a darker region in the BF image or a brighter one in the DF image. This is the reason why mass-thickness contrast is also called Z-contrast. STEM images that contain only Z-contrast have similar information to images from SEM formed by back-scattered electrons. However, since the specimen for TEM is relatively thin, the signal of these back-scattered electrons is too low to form any clear image for analysis. Hence, the STEM image is more useful in this case.

The diffraction contrast arises from the Bragg diffraction of the electron on the surface of the sample. The condition for the best diffraction contrast is called the “two-beam condition” ( $g \cdot b$ ). In order to achieve this requirement, a certain g-vector is chosen. Then, the sample is simply tilted until the DP shows only one strong diffracted beam from that g-vector along with the direct beam. While the Z-contrast is easy to interpret, it is complex to analyze the information from the diffraction contrast of the image.

Both mass-thickness and diffraction contrasts co-exist at low diffraction angles ( $< 5^\circ$ ). However, at higher angles, the mass-thickness contrast dominates the total amplitude con-

trast since the Bragg scattering is irrelevant. Our STEM images in this document are formed by high-diffracted angle electrons that are collected by HAADF detectors.

### 3.5 Challenges

As mentioned above, electrons have a small penetration depth, leading to one of the fundamental requirements for (S)TEM samples being electron-transparent. In general, a 100 nm-thick sample is transparent enough for measurement, but samples with a thickness of 50-100 nm are required to obtain a high resolution (S)TEM (HR-(S)TEM) image [60]. This is one of the big challenges in TEM, since it is not quite as simple to prepare an electron-transparent thin and free of damage lamella. In general, the time it takes to prepare one sample is proportional to its quality, regardless of technique. Another challenge is the damage caused by a strong electron beam. A strong electron beam is a result of high resolution imaging with a small electron wavelength. In more detail, we will discuss different sample preparation methods and some difficulties in acquiring images of thin samples in (S)TEM mode below.

#### 3.5.1 Damage from sample preparation process

Damage during sample preparation and imaging processes is a major challenge for achieving useful TEM images. There are different TEM sample preparation techniques, including traditional polishing, high energy ion beam etching, mechanical slicing, and a combination thereof. As a high-energy ion beam is used to prepare a TEM sample, it can cause damage to the final product. Sputtering, knock-on damage, and amorphization are examples of energetic ion beam effects on the specimen, leading to unclear or even ambiguous TEM results [61]. There are reports in the literature stating that FIB can influence the size of grains in face-centered cubic crystal samples [62]–[64]. Moreover, during this process, the high-energy ions from the ion beam can be implanted into the original material, causing deceptive contrast and erroneous alloy composition studies. In order to avoid these problematic images, extra cleaning steps are involved (i.e., nanomill and plasma cleaning). All the details of the TEM sample preparation recipe can be found in the appendices [A](#) and [B](#).

### 3.5.2 Damage from electron beam of TEM

The electron beam from TEM can cause sample damage during the imaging process. It has been shown for certain types of materials that the high energy electron beam can change the original structure of crystals [60]. For example, a high-energy electron beam can induce nanoclusters of indium in *InGaN* [65] causing misleading information from TEM analysis of this material. The energy of the electron beam is inversely proportional to the wavelength of the electron. Thus, as we require high resolution images, a small electron wavelength is needed, and a high-energy electron beam is the consequence of this relationship. Strong electron beam can result in a different structure than the original crystal structure hence, faulty analysis. During any TEM process, the high-energy electron beam can not only cause different contrasts by interacting with any available contamination on the lamella's surface, but also burn and leave holes in the lamella. Thus, as working with not ideal specimen (i.e. "dirty" and "too" thin), the time window for focusing and acquiring images is small, making it hard to obtain good TEM results. This time window strongly depends on the experience level of TEM users and the quality of the lamellae. Another consequence of the strong electron beam is the low signal-to-noise ratios, which leads to a lack of data points for statistical analysis.

## 3.6 Scanning Transmission Electron Microscopy

### 3.6.1 STEM Imaging

STEM is a specific mode in TEM including different types of measurement, such as bright field (BF), dark field (DF), nano-diffraction, etc. While TEM is used to study the diffraction patterns of the material, we often use STEM to study the contrast from the image of our specimen, e.g., HRHAADF-STEM. As stated previously in this chapter, the picture created by electrons at high diffraction angles mostly contains mass-thickness contrast (i.e., Z-contrast). Figure 3.4 shows the schematic of image formation in TEM and STEM. In TEM, a parallel electron beam enters the specimen. The electron beam, after passing through the specimen, goes through a series of lenses and apertures to finally form the image on the image

plane. The objective aperture acts as a filter to select electrons from only the direct beam or diffracted beam in order to form BF or DF, respectively. In contrast, STEM requires a convergent incident electron beam, as shown in the separate box in Figure 3.4. This beam then hits the surface of the specimen, and the direct and diffracted beams land on BF and HAADF detectors to form BF and HAADF images, respectively. Moreover, the beam coming out of the sample has a conical shape formed by the condenser aperture. As it hits the phosphor screen, a bright circle named “Ronchigram” is formed. If the instrument is well aligned on amorphous material, then the Ronchigram will be circular and symmetrical. If the Ronchigram is oval and asymmetrical, the probe then needs to be fixed using a probe corrector. This process is done after the general instrument alignment process. It includes correction of 2-fold stigmatism (A1), 2<sup>nd</sup> order comma (B2), 3-fold stigmatism (A2), spherical aberration (C3), star aberration (S3), and 4-fold stigmatism (A3). Each of these terms indicates the shape of the Ronchigram; thus, the shape of the Ronchigram would reflect the affected coefficient that requires correction. More details of how to perform probe correction can be found in appendix D.

### 3.6.2 STEM Sample Preparation

STEM measurements are straight-forward when the microscope is well aligned. Because the microscope alignment procedure, including the probe correction process, is detailed in appendix D on aligning TEM instruments, we will only discuss the various TEM sample preparation processes in this section. In order to obtain good STEM results, it is necessary to have not only thin and clean TEM samples but also a well-aligned TEM instrument. There are many requirements for a good TEM sample. As mentioned before, an electron-transparent sample is extremely important to achieve high resolution TEM images. Thus, a uniform thin flat surface is desired. However, if the sample is too thin, it can be “burned” by the high-energy electron beam from the TEM. Furthermore, the material of the specimen should not be active towards the high-energy electron beam to avoid interactions/damage caused by TEM measurements.

There are a wide variety of TEM sample preparation techniques. Some of them can take



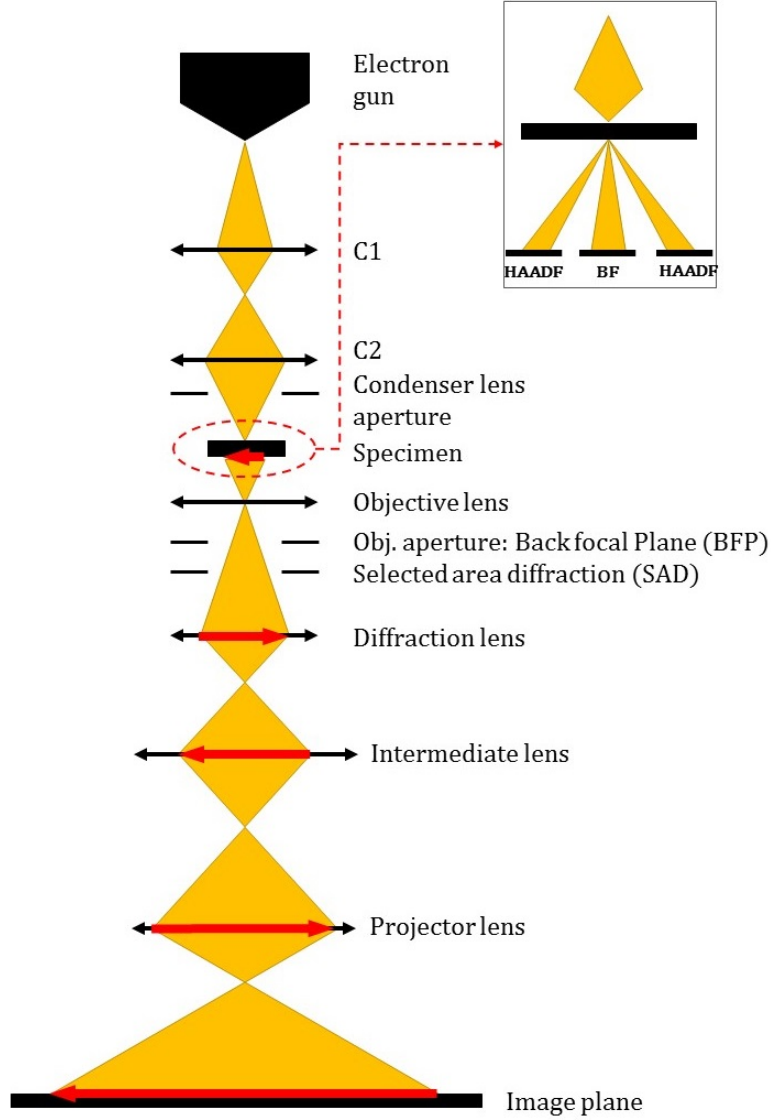


**Figure 3.4.** Schematic of image formation in TEM and STEM modes.

only 5 minutes, while others might take up to 2-3 days depending on the given material. For example, to prepare an Au thin film specimen, it is as simple as dropping a drop of liquid that contains Au nano-particles onto a carbon mesh grid and waiting for the liquid to evaporate in a few minutes. However, the process gets complicated quickly for solid materials. In general, for a bulk or heterostructure semiconductor, the yield of success is proportional to the time it takes to prepare one specimen. For our III-nitrides, we use both traditional polishing and Focus Ion-Beam (FIB) methods for TEM sample preparation. A cleaning process is

required before inserting the specimen into the TEM. At the Birck Nanotechnology Center, we use the Fischione Ar Plasma Cleaner to reduce possible contamination from the ion beam and air. For samples made by FIB, a Fischione Nanomill Model 1040 with an Ar beam is occasionally used to eliminate damage before using the plasma cleaner, depending on the quality of the FIB process.

Instrument alignment is as crucial as the sample preparation process in order to achieve high quality pictures. The complexity of the alignment process depends on the instrument and the desired resolution of images. Our samples are imaged using either an FEI Talos or an aberration-corrected Themis Z from Thermo Scientific. All of the STEM images in this document were taken in a high-angle annular dark-field condition that is highly associated with Z-contrast. In order to achieve true Z-contrast for post analysis, a small camera length (i.e., the distance from the specimen to the projected image) and  $C_2$  aperture are selected. Compared to a bright field setup, the contrast in these pictures is completely opposite, meaning the smaller the Z-number of elements, the darker the contrast. HRHAADF-STEM images that contain true Z-contrast can be used to study structural parameters, interface roughness, and material quality, including defects and inhomogeneities in our III-nitride semiconductors.

## **Traditional TEM Preparation Technique**

The traditional polishing method is also called multi-step TEM preparation. It consists of a long, tedious polishing period and a low-energy ion beam milling step. One of the advantages of this technique is that the process is simple, making it quick to learn. Furthermore, less damage is a positive consequence of not exposing the sample surface to high-energy ion beams during the preparation. However, as mentioned, the process requires a series of several steps that can take up to several days. Figure 3.5 shows how the sample is prepared with this multi-step technique. The first step is to prepare a thin slide of material from the bulk sample. Initially, the sample is cut with a countertop table saw into small pieces that can fit and are mounted onto a typical TEM grid (diameter of 3.05 mm). Next, the specimen is thinned down (to 30-50  $\mu\text{m}$ ) with an Allied MultiPrep System 8" mechanical

polisher. Then, a Gatan Dimpler Grinder II - Model 657 is used to further thin down the specimen (to 5-15  $\mu\text{m}$ ). The curvature of the sample's surface is caused by the Cu wheel of the dimpler during the grinding process. The final step is to mill the sample with a Gatan Precision-Ion-Polishing System (PIPS)-Model 695. The aim of this step is to create a small hole in the sample with thin regions around it. The lower the ion beam energy, the less sample damage is generated and the longer the process is. For a plan-view sample, the top surface (i.e., the surface with the active regions) is protected at the bottom. Thus, during each step of the whole preparation process, only the back surface is polished. For a cross-section sample, the active regions from two individual pieces are glued together using an adhesive product that is inactive to the material, so that they are right in the middle of the sample, as shown in Figure 3.5(b). As a hole is created by the PIPS, the process is ended, and the area of interest for TEM is around that hole. The thickness of this area depends on the angle of the ion beams and the diameter of the hole. More details of the polishing recipe can be found in the appendix A.

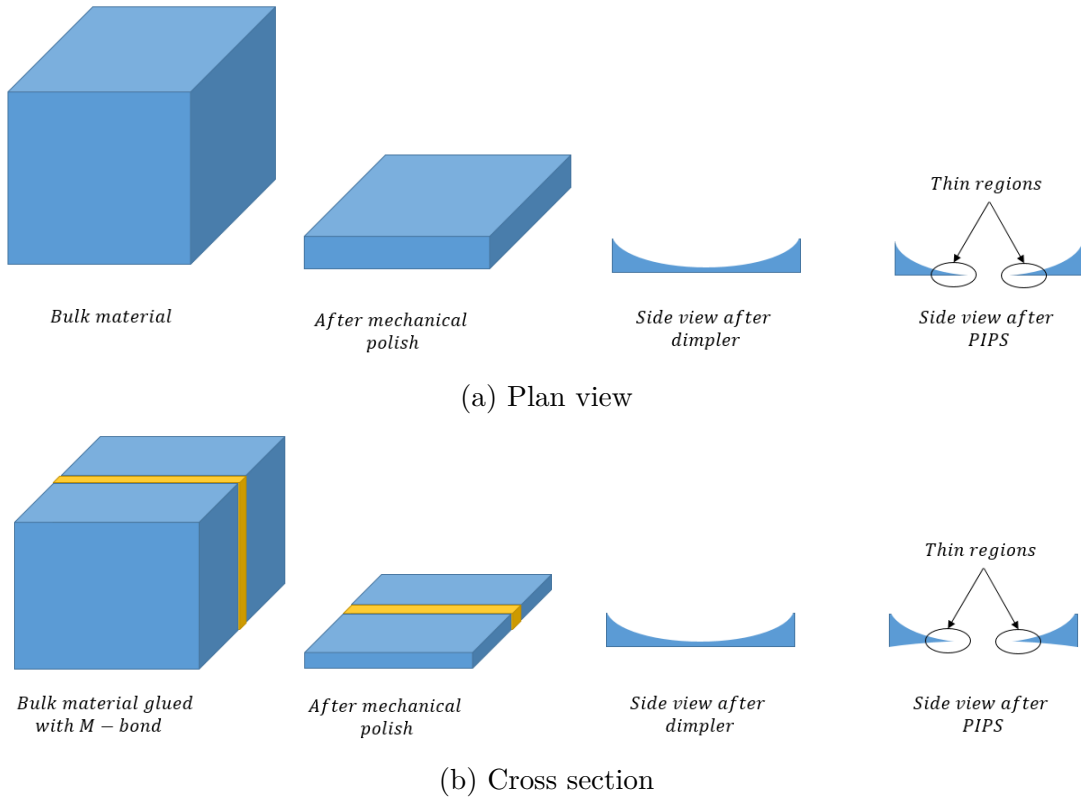


**Figure 3.5.** Traditional TEM Sample Preparation.

## Focused Ion Beam Technique

FIB is a more advanced technique compared to traditional polishing. This also means the process is more complicated. However, once the user is comfortable with the instrument, it can be much more convenient to make TEM samples using this method. A FIB instrument consists of two ion beam columns (electron and ion) as shown in Figure 3.6. The SEM beam is mainly used for extra protection layers at the beginning and imaging the specimen during the whole process. The ion beam ( $Ga^+$ ,  $He^+$ ,  $Xe^+$ ) is at an angle of  $52^\circ$  relative to the electron beam. This ion beam is used for depositing a layer on the surface to protect the area of interest, milling the material from bulk to a thin slide (i.e., a lamella), and thinning the lamella until electron transparent. During the whole procedure, the energy of the ion beam is reduced from high to low to preserve as much of the non-damaged region on the lamella as possible.

In order to estimate the effect of the ion beam on the sample, a program named Stopping-and-Range-of-Ions-in-Matter (SRIM) is used. SRIM is based on Monte Carlo simulation to predict the damage (from scattering mechanisms) on the sample caused by the high energy ion beam. Ideally, for different structures and materials, SRIM suggests a minimum amount of protection for the FIB process. However, for most materials, including our III-nitrides, 50-100 nm of protection layer is shown to be enough, although we often have multiple layers of protection that total more than  $1\mu m$  thick. These layers can be carbon, tungsten, platinum, or even gold. Detailed recipes on how to use FIB to prepare III-nitride material are listed in the appendix B.

There are several methods to make TEM samples with FIB, such as H-bar FIB, in-situ lift out FIB, ex-situ lift out, shadow FIB, etc. In our research, we use H-bar and in-situ lift out FIB techniques. Figure 3.6 shows the schematic of the electron beam and ion beam inside the FIB chamber as well as the milling process of the H-bar FIB technique. First, the sample is pre-polished and loaded onto a TEM Cu-grid. The specimen thickness is approximately 15-20  $\mu m$ . Then, the sample's surface is coated with a C-layer using a carbon sputter coating machine. However, as the sample is thinned, it is challenging to deposit carbon on the top surface. Thus, we often cover the specimen with Sharpie marker ink; this technique has been

well-known and used by several FIB experts. The Sharpie ink works perfectly as a protection layer for FIB sample preparation, especially the green ink. Then, the specimen is loaded into the FIB chamber for thinning. Inside the chamber, the sample is thinned down with various beam conditions, from the strongest beam to the weakest beam. With our nitrides, we often start with 16 keV and end with 500 eV. The strong ion beam is used to mill bulk material, while the weak ion beam is used to finely thin, take off the damaged layer from stronger beams, and polish the lamella for the final product. In order to avoid shadows in TEM, it is necessary to cut wide trenches during FIB with this method. One of the big advantages of this technique is that several lamellas can be made at the same time, resulting in a better yield of good samples for HRSTEM.

In contrast to the H-bar method, in-situ lift out FIB does not require a pre-polish step.

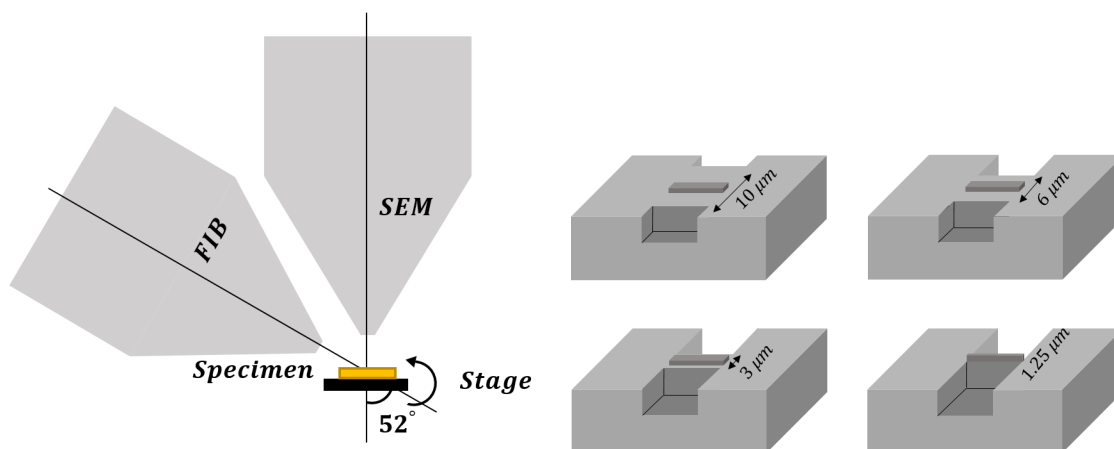


**Figure 3.6.** Schematic of the electron and ion beams of FIB instrument (left) and FIB milling process of H-bar FIB process (right).

Firstly, a bulk sample is carbon-deposited on the surface with a sputter coating machine. This step is not required for all samples, but is crucial for samples that are used for surface study. That piece of material is then loaded into the FIB chamber. The process of creating a thin lamella from bulk material with the in-situ lift out FIB is shown in Figure 3.7a. A series of carbon layers deposited using the electron beam and the ions beam is used to mark and protect the area of interest on the bulk substrate. Then, a strong ion beam is used to make trenches above and below the area of interest. Next, a series of different energy ion

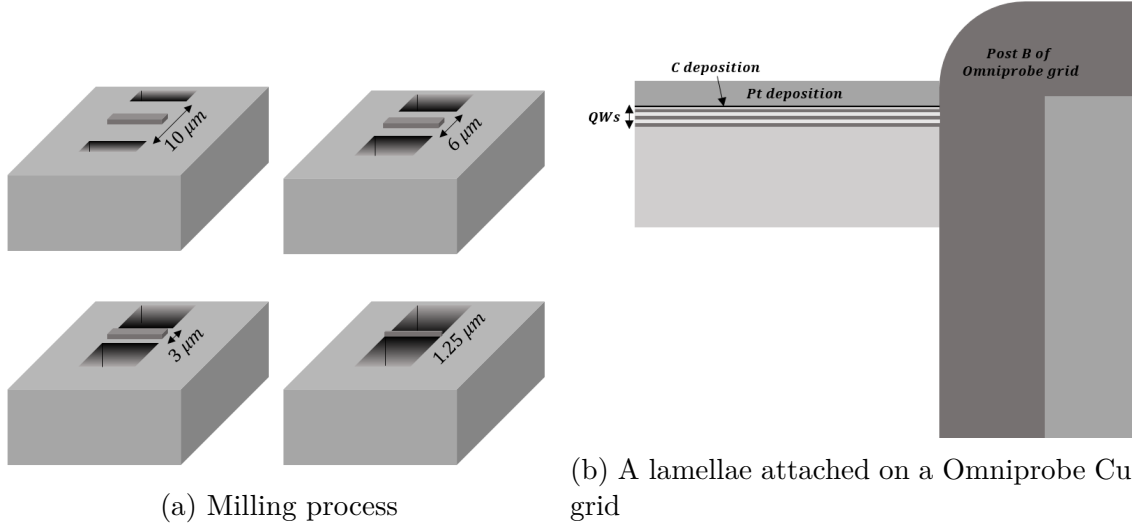


**Figure 3.7.** In-situ lift out FIB.

beams is used to enlarge these trenches until the lamella is 1.25-2.5  $\mu\text{m}$  thin. The lamella is then removed from the bulk sample by a manipulator tip and attached to the Omniprobe Cu grid as shown in Figure 3.7b. Without the polishing process, FIB methods can take anywhere from 1-6 hours, depending on the material. For our III-nitrides, it normally takes up to 2.5 hours to prepare a TEM specimen with this technique, but sometimes it can take up to 3.5-4 hours. This is significantly faster than the multi-step preparation technique. Unlike the H-bar method, only one thin lamella can be made at a time. Nonetheless, to enhance the yield, we make 2 thin regions on each lamellae. Each region is approximately 2-3  $\mu\text{m}$  wide, to increase the chance of obtaining high quality specimens for TEM imaging. Furthermore, the configuration of thin regions separated by a thicker region in the middle helps to strengthen the physical stability of our lamellae and to avoid any built-up physical stress that can either affect the analysis process or destroy the specimen.

## 4. INFRARED SPECTROSCOPY EXPERIMENTAL SETUPS AND PROCEDURES

The ISBA spectra of our samples are measured using a Thermo Scientific Nicolet 8700 FT-IR spectrometer. FT-IR measurements are based on the interference pattern of two light beams. Figure 4.1 shows the schematic layout of the FT-IR setup. When the incident light (infrared) beam reaches the beamsplitter, part of it is transmitted, while the other part gets reflected. The reflected beam then travels a path consisting of stationary mirrors. The transmitted beam follows a different path to and from a movable mirror. These two beams then recombine with each other, causing interference patterns on the detector. The signal is collected by detectors and Fourier transformed into a spectrum using a computer FFT algorithm. For near-IR measurements, the InSb detector is used to detect the transmission signal in the near-IR range, and the MCTA detector is used for the mid-IR range ISBA. This detector is cooled down with liquid itrogen. Except for the detector, the whole measurement is done at room temperature.

The three ISBA measurement techniques are the direct transmission measurement, the attenuated total reflection (ATR) transmission measurement, and the photoinduced absorption (PIA) measurement. We will discuss each of them individually in this section. The sample is physically prepared in a similar fashion to enhance the ISBA for the direct and PIA measurements. All c-plane samples are polished on the back side with a  $3\mu\text{m}$ -diamond lapping paper after  $6\mu\text{m}$ -diamond discs to remove the thin metal back-coating. The metal layer on the back of m-plane samples can be cleaned using a cotton tip soaked with acetone. For the direct and PIA measurements, the sample sides are polished with  $6\mu\text{m}$  and  $3\mu\text{m}$  to achieve a  $45^\circ$  multi-pass waveguide as shown in Figure 2.2 in chapter 2. A fine polishing step at the end with  $1\mu\text{m}$  diamond paper was done in order to eliminate all possible cracks caused by rougher grinding papers. The purpose of side polishing is to create facets where the incident light undergoes multiple passes by bouncing back and forth between the front and back of the sample, resulting in an enhancement of ISBA. However, with the ATR technique, this step is required for preparing the Ge crystal rather than the substrate.

There are four different spectra for each sample measured by the FT-IR spectrometer.

The first two spectra are obtained without the sample in s- and p-polarization. Another set of background spectra along s- and p-polarization may be obtained with a clean free standing m-plane *GaN* substrate. The purpose of this extra work is to further suppress any signal originating from the substrate that can add noise into the actual absorption spectrum of the active multi-quantum well layer. The aim of these spectra is to have a background spectrum in each polarization direction (s- and p-). This helps to enhance the signal-to-noise ratio for the final spectrum. The other two spectra are taken with the sample. A normalization between sample and background spectra in each polarization provides the signal from the sample without the background. According to the ISB selection rule, the ISB absorption only occurs in p-polarized light. Hence, we take another ratio of the p- and s- polarizations to achieve the final transmission spectrum with minimum noise.

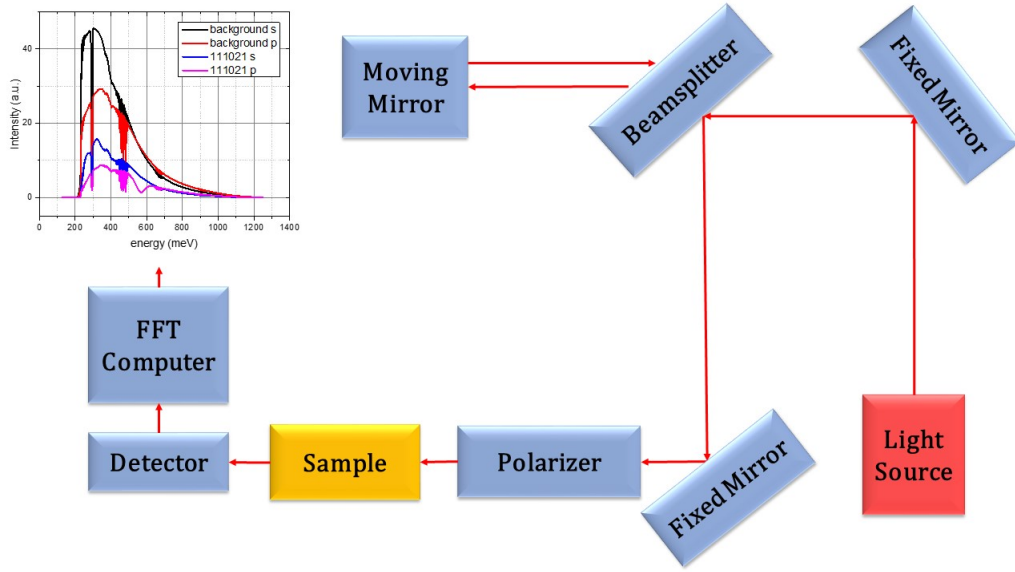


**Figure 4.1.** FT-IR schematic layout.

#### 4.1 Direct Transmission Measurements

The direct transmission measurement provides the normalized transmission spectrum through the QWs. This spectrum is converted to the absorption spectrum using the relationship between  $T$  and  $\alpha_{ISB}$  from equation 2.12. In this technique, the electrons that are promoted from the ground state to the first excited state originate from the impurity doping



layer. Therefore, this experimental result can be directly compared with the band structure calculations obtained using Nextnano++ and Wolfram Mathematica 11.

The number of passes,  $m$ , is the ratio of the length and the thickness of the waveguide. A typical thickness varies between 200-500  $\mu\text{m}$  depending on the type of substrate and the result of the back polishing process. Thus, for a sample with a length of 5 mm, a typical length for all  $m$ -plane samples, we can have up to 25 passes. In other words, we can increase  $m$  by thinning the substrate. However, a thin substrate is easier to break during the handling process and provides fewer facets to guide the incoming EM wave. The coupling factor  $C$  ( $\in [0, 2]$ ) is related to the refractive index, the wavelength of absorbed electrons, and the angle of incident radiation.  $C$  is calculated as below,

$$C = 2 \int_0^d dx \sin^2(kx) \quad (4.1)$$

where  $d$  is the active layer thickness, and  $k$  is the wavenumber of the incoming electric field. The value of  $C$  depends on the region of overlap between  $\vec{E}$  field and the active region. On top of our substrate, we sometimes add a thin layer of Ti-Au (4 nm of Ti, and 100 nm of Au) to change the boundary condition of the electric field standing wave from node to anti-node, as explained in [17] in order to enhance the value of  $C$ , thus the absorption signal. Figure 4.2 shows how an additional layer of metal on the surface helps to change the boundary condition, leading to an enhancement of  $C$ .

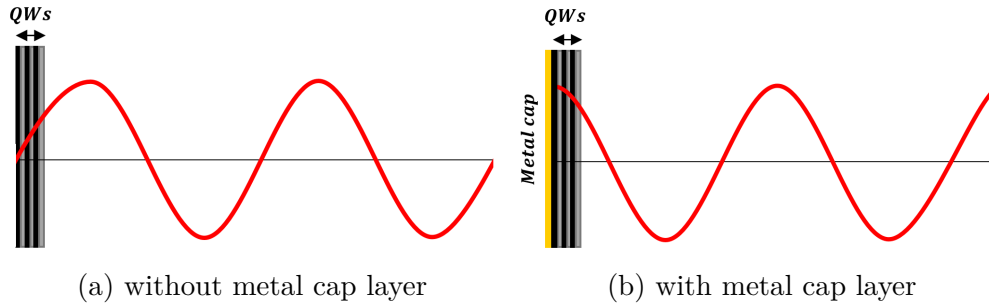


**Figure 4.2.** Schematic of the overlap of the  $\vec{E}$  field of the standing wave with the active region of MQW in the case without (a) and with (b) a metal cap layer.

## 4.2 Attenuated Total Reflection Measurements

As mentioned above, with the ATR technique, the samples can be used for measurements without having  $45^\circ$  facets on both sides of the specimen. Figure 4.3 demonstrates the different experimental setups for the direct and ATR infrared transmission measurements. The sample is sandwiched with a polished Ge-prism to allow an evanescent wave to probe absorption in the active region [54], [55]. Due to an unintentional air gap between the interfaces of the Ge crystal and the specimen, the penetration depth of the evanescent wave into the QWs may be reduced, resulting in lower absorption intensity. The s- and p-polarization backgrounds are collected in transmission through the Ge-prism without the sample. Since the Ge crystal is transparent in the mid- and near-IR ranges, this method helps to achieve clean and high absorption intensity ISBA spectra compared to the direct transmission technique. Moreover, with a simple preparation process, it is quicker to obtain optical results for samples using ATR than with other techniques. However, a disadvantage of this method is that the Ge crystal is brittle; hence, if the substrate is squeezed too hard on the prism, the prism can shatter.

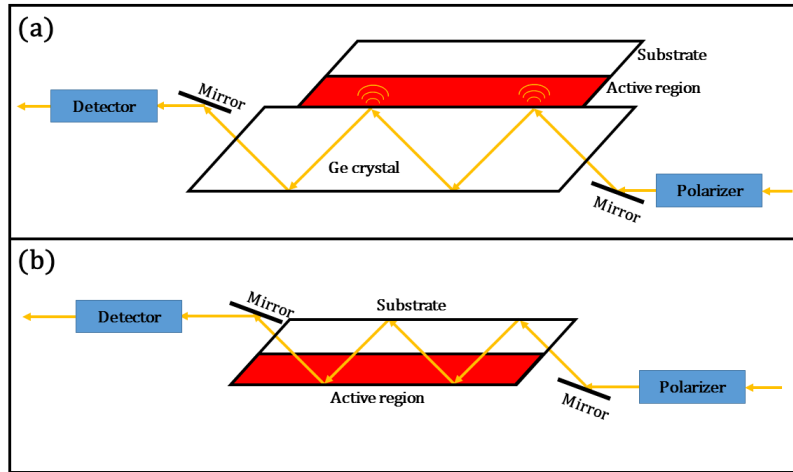


**Figure 4.3.** Experimental setup for (a) ATR-FT-IR and (b) direct-FT-IR ISBA measurement techniques.

### 4.3 Photoinduced Absorption Measurements

The PIA measurement requires a 15 mW HeCd laser with  $\lambda = 325$  nm to promote electrons from the valence band to the conduction band. These electrons are in addition to those from impurity doping. However, this signal is usually too small to measure. Hence, in order to increase the signal sensitivity, the laser beam is modulated by a mechanical chopper, and the FT-IR output signal from the detector is processed by a Stanford Instrument, Model SR830, lock-in amplifier, as shown in Figure 4.4b. The purpose of the lock-in technique is to filter only the signal at the chopper frequency and output the time average value of this signal at a certain mirror position. Thus, the PIA measurement uses the step scan mode of the spectrometer and takes longer time than the direct transmission measurement.

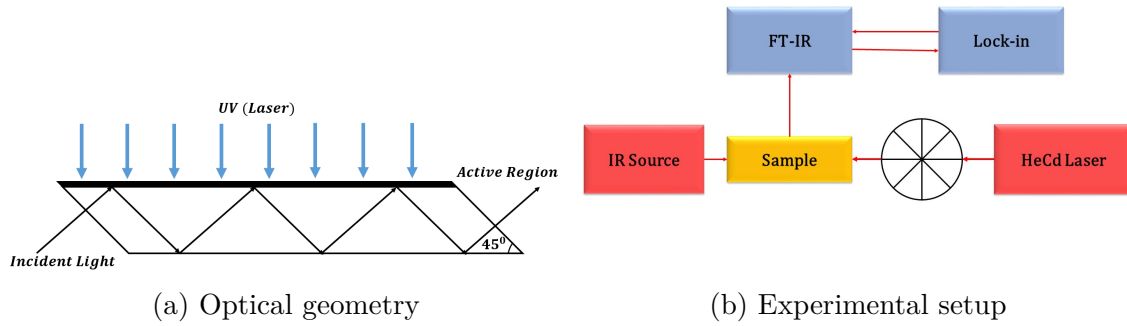


**Figure 4.4.** PIA measurement setup.

## 5. M-PLANE STRAINED ALGAN/GAN

### 5.1 Introduction

Non-polar nitride MQWs have been considered as an alternative to polar heterostructures for infrared ISB applications due to the absence of built-in polarization fields [30], [33], [36], [54], [55], [66]–[70]. This advantage results in a simplified band structure and increased wave-function overlap. As mentioned in [40], non-polar infrared photodetector devices were theoretically found to have a higher absorption probability at high energies than polar devices; resulting in better performance. In this study, we highlight recent progress in experimentally investigating infrared intersubband transitions in m-plane *AlGaN/GaN* superlattices, as well as theoretical efforts to predict them. The structure of *AlGaN/GaN* superlattices with a high *Al* composition is examined in detail for its effect on near-infrared intersubband absorption.

Nonpolar nitride heterostructures initially gained attention for their potential application in visible and ultra-violet light-emitting diodes (LEDs) [71]–[73]. However, the lack of high-quality m-plane nitride substrates has limited their application in other fields, such as infrared devices. Free-standing m-plane *GaN* substrates produced by hydride-vapor phase epitaxy have just recently become commercially available and cost-effective enough for rigorous growth studies. Due to anisotropy of adatom mobilities on the m-plane surface, the growth of non-polar m-plane heterostructures is still an ongoing research and the issue is still not well understood [58], [74]–[78]. We made significant progress toward growing m-plane *GaN* and m-plane *AlGaN/GaN* superlattices with *Al*-compositions of less than 20%, which enabled us to observe THz intersubband absorption [76]. Others have also succeeded in growing m-plane *Al(Ga)N/GaN* superlattices in a variety of composition ranges.[36], [53]–[56], [66]–[69]. However, it remains challenging to control the *Al* content of m-plane *AlGaN* over its whole compositional range.

Kotani et al. were the first to report mid-IR ISBA in m-plane *AlGaN/GaN* heterostructures grown by metal-organic chemical vapor deposition (MOCVD) [54], [55], [67]. The dependence of the ISBA energy of non-polar m-plane  $Al_xGa_{1-x}N/GaN$  ( $x \approx 0.5$ ) on QW thickness, doping level, and temperature was discussed in detail in this series of studies,

along with some provided theoretical estimations and explanations. The HFA was used in these reports to derive the exchange-interaction correction from the many-body theory [22], [79], while the depolarization correction and excitonic shift were explained by Allen et al. [28] and Jogai [18], respectively. Although there is good agreement between the experimental result and theoretical calculation, Kotani et al. stated that “the conduction band offset ratio, which is not yet well known, was set as the fitting parameter” [67]. Lim et al. reported ISBA of polar and non-polar  $AlGaN/GaN$  heterostructures in the near-, mid-, and far-IR ranges [36], [53], [68], [69]. The theoretical model that was used to compare with the observed ISBA energy was not described in these reports. However, reference [69] hinted that the exchange-interaction approximation from Bandara et al. [22] was employed in the many-body correction, along with the depolarization shift from [51] and the broadening effect of impurity scattering. The excitonic term was considered to be negligible, and therefore, it was omitted from the total corrected ISBA energy. The correlation interaction (i.e., the Coulomb repulsion between one electron and another as it moves through the electron gas) is another term that was omitted from the theoretical estimation. The strain state, fluctuations in quantum well layer thickness, and many-body effects were used to account for the discrepancy between the predicted and observed ISBA energies. Monavarian et al. compared mid-IR ISB transitions between non-polar m-plane and a-plane  $Al_{0.5}Ga_{0.5}N/GaN$  grown by ammonia-MBE [56]. The ISBA spectra of m-plane samples were demonstrated to have much smaller FWHMs than those of a-plane samples. A very narrow ISBA linewidth of 38 meV was obtained from an m-plane sample at 250 meV ISBA energy peak, which was explained by uniform layer interfaces. While establishing a very small FWHM for the ISBA spectrum is critical for practical purposes, this work is limited to the mid-IR range. We first reported the far-infrared (THz) intersubband absorption in MBE-grown m-plane  $AlGaN/GaN$  superlattices, followed by near-IR absorption and photocurrent [70]. This chapter discusses our recent work on improving near-IR intersubband absorption and deciphering the observed ISBA spectra of non-polar m-plane  $AlGaN/GaN$  superlattices.

## 5.2 Results

All non-polar m-plane *AlGa*N/*GaN* samples were grown by PA-MBE on commercially available free-standing m-plane substrates from Nanowin Science and Technologies, except sample C. Nanowin lists the m-plane substrates as having a RMS roughness of 0.2-0.3 nm over 16  $\mu\text{m}^2$  area, and a low threading dislocation density of less than  $2 \times 10^6 \text{cm}^{-2}$ . A miscut of approximately  $0.5^\circ$  towards the -c-axis was chosen based on the optimal growth conditions for m-plane *GaN* [58]. Sample C was grown on a c-plane *GaN*-on-sapphire wafer. Co-loading and growth of samples B and C enabled direct comparison of the structural properties of m-plane and c-plane MQWs. Gallium, aluminum, and silicon were provided through the standard effusion cells of the MBE instrument. Nitrogen flux was supplied by a Veeco Unibulb radio frequency plasma source operating at 300 W power with a 0.5 sccm of nitrogen flow rate. All samples were grown at 720 °C with a growth rate of m-plane *GaN* of 8.8 nm/min. Each sample was doped with two sheets of  $\delta$ -doping at a distance of 1 nm away from the QW for varying different durations. This doping scheme was adopted to provide narrow linewidths and high absorption strengths, as suggested in refecent [80]. Table 5.1 summarizes the structural characteristics, observed ISBA energies, and predicted ISBA energies for our sample set.

**Table 5.1.** Summary of structural parameters, observed ISBA energy peak, experimental FWHM of ISBA peak, and theoretical calculation of the ISB transitions energies for a series of polar and non-polar *AlGa*N/*GaN* heterostructures.

Sample	QB/QW thickness (nm)	QB alloy composition	Calc. sheet density charge $\times 10^{12} \text{cm}^{-2}$	Experimental ISBA Energy Peak/FWHM (meV)	Calculated ISBA Energy (meV)
A	2.9/3.5	m- <i>Al</i> <sub>0.45</sub> <i>Ga</i> <sub>0.55</sub> <i>N</i>	19	388/105	358
B	2.1/3.2	m- <i>Al</i> <sub>0.56</sub> <i>Ga</i> <sub>0.44</sub> <i>N</i>	21	340/159	425
C	3.8/3.2	c- <i>Al</i> <sub>0.23</sub> <i>Ga</i> <sub>0.77</sub> <i>N</i>	7.4	280/118	290
D	2.3/3.0	m- <i>Al</i> <sub>0.54</sub> <i>Ga</i> <sub>0.46</sub> <i>N</i>	21	429/177	449

Atomic force microscopy (AFM) and high-resolution x-ray diffraction (HRXRD) were employed to characterize the structural properties of each sample. AFM was utilized to

reveal the surface morphology of the samples. The HRXRD data was collected using a PANalytical MRD X'Pert high-resolution diffractometer. In order to perform the HRXRD fit, we assume that the growth rate of m-plane *GaN* layers is the same as that of c-plane *GaN* [66], [78]. Additionally, HRHAADF-STEM was used to confirm the structural data obtained from HRXRD. The lamellae were created using an in situ lift-out technique with an FEI Nova 200 Dualbeam FIB. These lamellae then went through a post-FIB process for further milling to remove any residual FIB damage, using a Fischione Nanomill Model 1040 at 900 eV and 120  $\mu\text{A}$  with  $\pm 10^\circ$  tilt. HRHAADF-STEM images and EDS elemental maps were taken on an FEI Talos 200 kV microscope.

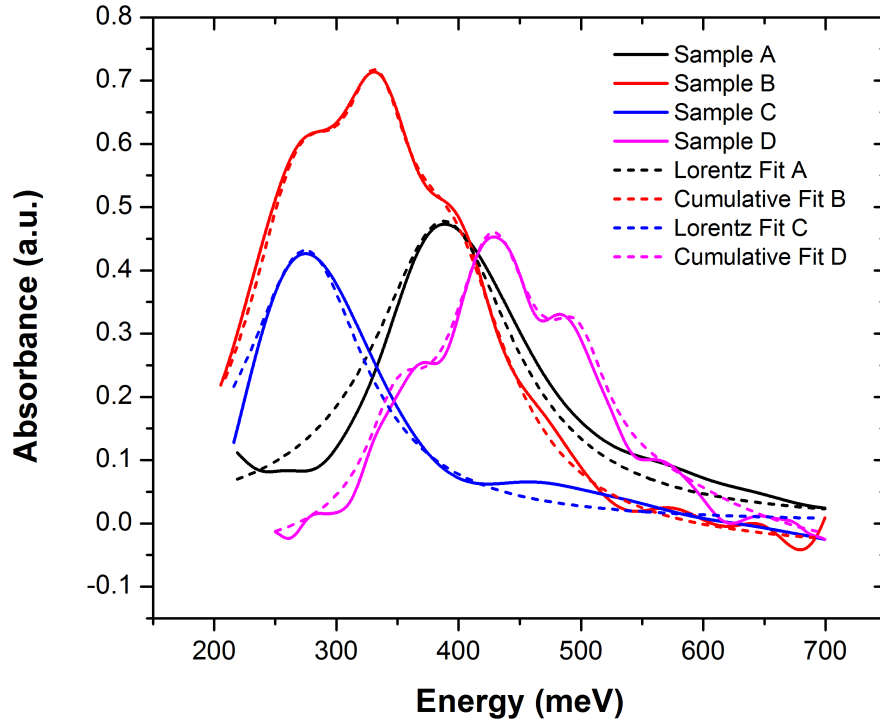


**Figure 5.1.** ISB transition spectra of sample A, B, C, and D (solid lines) and their fitting (dash lines) in black, red, blue, and magenta, respectively. The ISBA spectra of samples A and C were fitted using single peak Lorentzian fitting. The ISBA spectra of samples B and D were fitted using multi-peak Lorentzian fitting.

We self-consistently calculated the band structures of our polar and non-polar *AlGaN/GaN* heterostructures using the Nextnano++ eight-band k-p simulation package. Separate many-body corrections, including the exchange interaction, depolarization shift, and excitonic cor-

rections, were calculated using Mathematica [18], [22], [27]. The expected ISBA energies of our samples are indicated in Table 5.1. The ISBA spectra of our superlattices were obtained using the direct-FT-IR method. This procedure is described in greater detail in chapter 4. Figure 5.1 illustrates the observed ISBA spectra of samples A, B, C, and D with their Lorentzian fits.

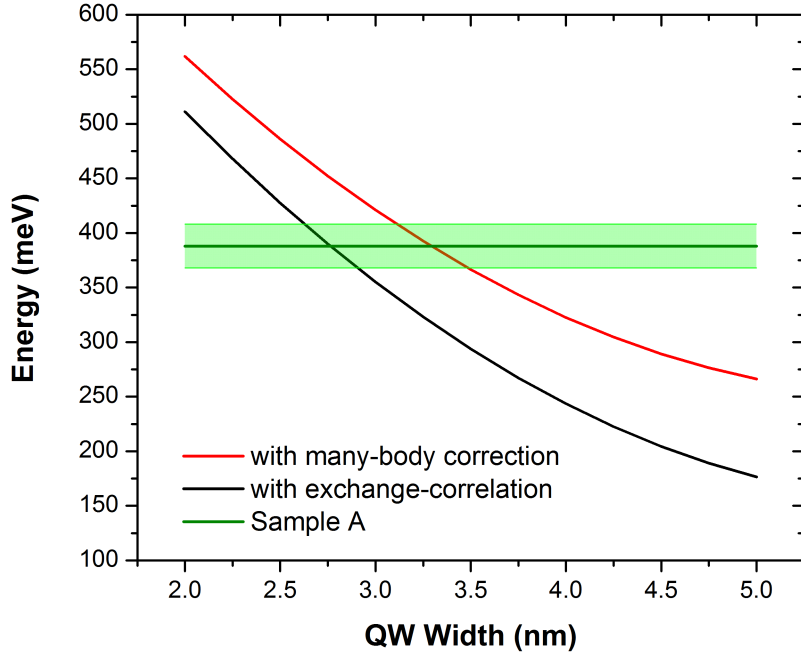


**Figure 5.2.** The dependence of the ISBA energy on the QW thickness of sample A. The black and red lines are theoretical calculations with exchange interaction and total many-body correction (including exchange interaction, depolarization shift, and excitonic correction), respectively. The green straight line is the experimental ISBA of sample A obtained from direct-FT-IR measurement.

First, we discuss the ISBA result of sample A in our sample set. Figure 5.2 shows the theoretical dependence of the ISBA energy on the QW width, which suggests a suitable average QW thickness for this sample. The experimental error bar comes from a fitting uncertainty of  $\pm 20$  meV. Figure 5.3(a) shows the HRSTEM image of sample A taken along the a-zone axis. Although the roughness of the interface between layers is relatively low with minor variance in QW thickness, HRSTEM determined that the average QW width of sample A was 3.2 nm with a standard deviation of 0.5 nm (i.e. 2MLs), while HRXRD determined that



the average QW thickness was 3.5 nm. The discrepancy is related to methodological uncertainty. This variance in thickness is significant in comparison to the c-plane  $AlGaN/GaN$  MQWs, for which is typically less than 0.25 nm (i.e., 1ML). As shown in Figure 5.2, the ISBA energy of the non-polar m-plane  $AlGaN/GaN$  is quite sensitive to variations in QW width. A thickness variation of 0.5 nm can result in a 60-80 meV shift in the overall adjusted energy. The high standard deviation of QW thickness shows why predicting the exact ISBA energy of sample A is challenging. According to our theoretical calculations, a QW width of 3.5 nm results in a total ISBA energy of 358 meV listed in Table 5.1. If the average  $GaN$  layer thickness is 3.2 nm, the anticipated ISBA energy of sample A is 396 meV, which is significantly closer to the observed value than the 3.5 nm  $GaN$  layer. Additionally, as previously stated, sample A was doped with two sheets of  $\delta$ -doping located 1 nm from the QW to reduce the linewidth of its ISBA spectrum. We may conclude that the long-range roughness broadening effect mentioned in section 2.3 is the cause of sample A's large FWHM (105 meV). Furthermore, under the current growth conditions, in order to obtain an ISBA spectrum with a narrower linewidth, the  $Al$  mole fraction must be reduced to produce a more homogeneous material.

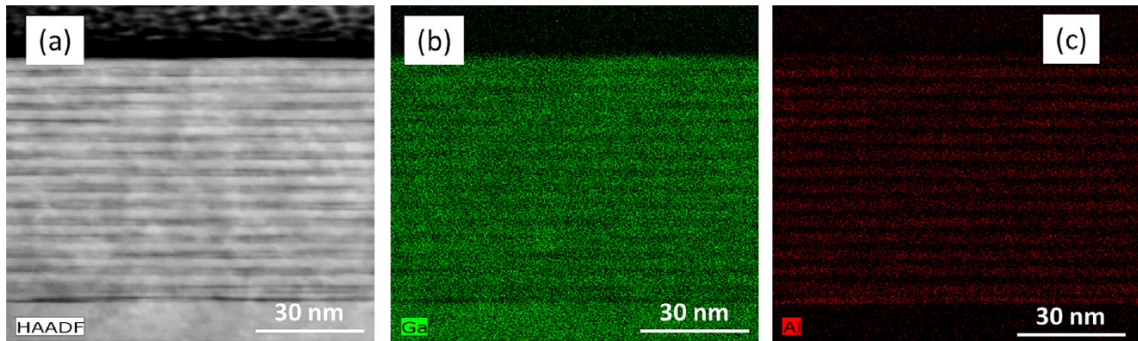


**Figure 5.3.** HRHAADF-STEM image(a) and EDS elemental maps of  $Ga$ (b) and  $Al$ (c) of sample A with zone-axis along the a-axis [32].

In the following, we discuss the effect of a high average aluminum content on the ISBA spectrum of m-plane  $AlGaN/GaN$  superlattices. Shirazi et al. described the challenges associated with growing a homogeneous non-polar m-plane  $AlGaN$  with a large  $Al$  mole fraction in [11]. When the  $Al$  composition is  $\approx 60\%$  or above, HRSTEM images of the

*AlGa*N layers reveal prominent high *Al* concentration plateaus and islands. As a result, the QW interfaces are rough and the ISBA spectrum is broad. While the ISBA spectra of samples A and C in Figure 5.1 were fitted with a single-peak Lorentzian distribution, samples B and D required multi-peak fitting, as seen in Figure 5.4, due to multiple absorbance at different energies on the raw FT-IR scans for samples B and D. These minima are exclusively visible on p-polarized scans, indicating they are not caused by interference fringes [81], [82]. This implies that the inhomogeneous *AlGa*N material is responsible for the shoulders on the ISBA curves of these two samples. According to the Figure 5.4, sample B was fitted with three Lorentz peaks at 267 meV, 332 meV, and 396 meV, which correspond to QW thicknesses of 5 nm, 4.1 nm, and 3.5 nm (i.e., a variation of 6MLs), respectively. Peaks at 356 meV, 427 meV, 493 meV, and 549 meV were fitted to the ISBA spectrum of sample D, corresponding to a QW width fluctuation of 2.3 nm to 3.8 nm (6MLs). Moreover, the inhomogeneous material generates defects in *AlGa*N that can potentially act as charge traps, leading to a lower activated charge density in the QW and, therefore, lower experimental ISBA energy than expected. The substantial difference between the experimental and calculated values of sample B's ISBA energy may be attributable to an incorrect assessment of the average QW thickness as well as the unknown activated charge level in the QW. Although the predicted and observed ISBA energy of sample D are within the error bar, we find that exceeding 50% of *Al* content in the QB is not ideal for obtaining near-IR ISBA with a narrow linewidth given the heterostructures' current growth conditions.

Next, we compare the ISBA of co-loaded and grown polar and non-polar *AlGa*N/*GaN* samples C and B. Figure 5.5 illustrates the computed conduction band edge and the electronic wave-function probabilities for the ground and first excited states of samples B and C, excluding effects from many-body theory. The primary distinctions between these two samples are the smaller CBO and the presence of the built-in polarization field of sample C. There is excellent agreement between the calculated and observed ISBA energies of sample C. As discussed in chapter 2, the effect of correlation interaction between electrons is insignificant at low charge densities. Consequently, HFA provides accurate predictions for samples with a low activated charge density, such as sample C [22], [80]. Meanwhile, there is a large discrepancy between the estimated and experimental results for sample B. We previously

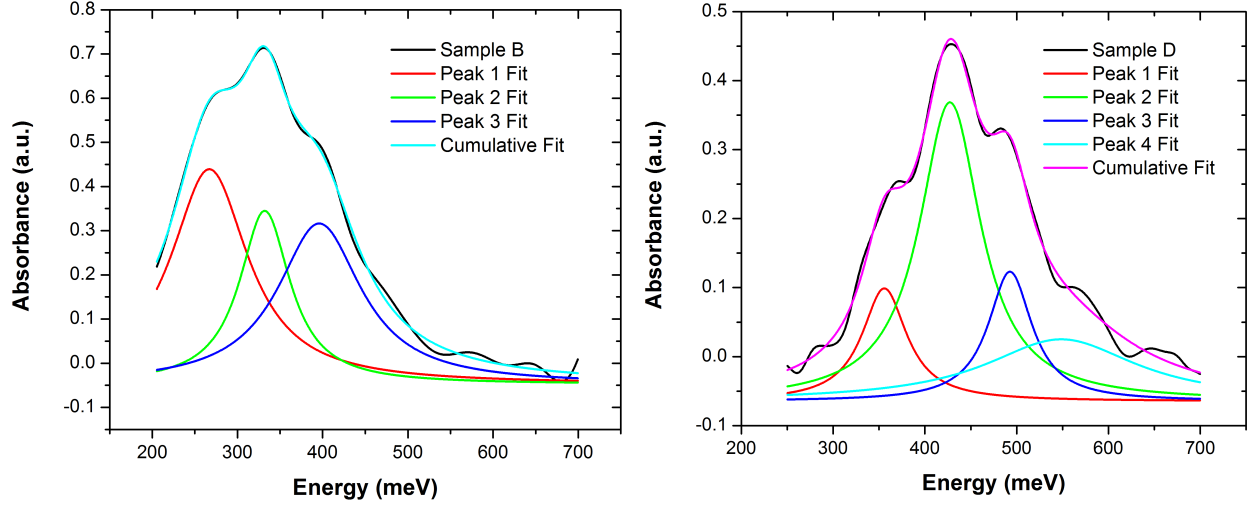


**Figure 5.4.** Multi-peak Lorentzian fits for the ISBA spectra of samples B(left) and D(right) which have *Al* composition of 56% and 54% suggested by HRXRD, respectively. The Lorentzian fit for sample B contains peaks at 267 meV, 332 meV, and 396 meV with FWHMs of 110 meV, 72 meV, and 68 meV, respectively. The Lorentzian fit for sample D includes peaks at 356 meV, 427 meV, 493 meV, and 549 meV with FWHMs of 59 meV, 81 meV, 57 meV, and 201 meV, respectively.

argued that this energy difference can be attributed to both an inadequate average QW width and a lower activated charge density than expected due to inhomogeneous material and defects. However, given the considerable difference in activated charge levels between samples B and C, the correlation interaction may be more significant, and hence cannot be ruled out. The FWHM of the ISBA spectrum of sample C (118 meV) is smaller than that of sample B (159 meV), but both spectra are relatively broad. The large linewidth of sample B's ISBA curve has been attributed to the high degree of uncertainty associated with QW thickness. Figure 5.5(right) shows that the electronic ground and first excited states of sample C are close to the top of the QW. The first excited state of sample C is only 24 meV below the ground state of the electron from the barrier. Therefore, the crossing between these states may result in a superlattice mini-band, which broadens the ISBA spectrum of this sample.

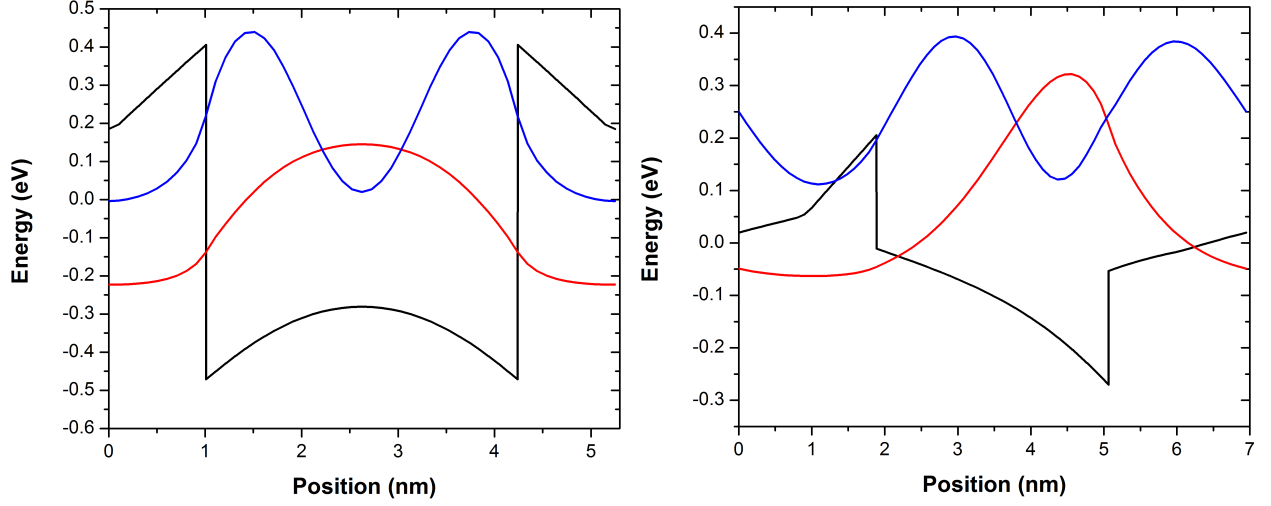


**Figure 5.5.** Conduction band edge (black) and probability of the ground (blue) and first excited states (red) for sample B (left) and sample C (right).

### 5.3 Conclusion

Non-polar m-plane  $AlGaN/GaN$  MQWs have attracted interest for their potential applications in not only visible and ultraviolet LEDs, but also in novel infrared optoelectronics. This chapter summarized major progress in developing and understanding their optical characteristics that has been reported in the literature. In addition, we highlight some of the difficulties of growing homogeneous non-polar m-plane  $Al_xGa_{1-x}N$  ( $x \in [0.45 - 0.56]$ ) in order to obtain a small linewidth ISBA spectrum in the near-IR range. At low  $Al$  composition, the non-polar m-plane  $AlGaN/GaN$  exhibits excellent agreement with experimental and estimated results. These results demonstrate that it is possible to create high performance ISB devices by replacing polar c-plane  $AlGaN/GaN$  superlattices with non-polar m-plane  $AlGaN/GaN$  heterostructures. However, high  $Al$  composition is needed for near-IR ISBT and its applications. As  $x > 0.5$ ,  $Al_xGa_{1-x}N$  alloys exhibit inhomogeneity due to the presence of plateaus and islands with high  $Al$  content, resulting in rough QW interfaces and defects. Due to the high variation of QW thickness, the ISBA linewidth is broad. Additionally, this complicates the prediction of the ISBA energy for each sample. To achieve narrow linewidth near-IR ISBAs with this material combination, more research is required on optimal growth condition for homogeneous non-polar m-plane  $Al_xGa_{1-x}N$  with  $x > 0.5$ .

## 6. M-PLANE STRAIN-BALANCED (IN)ALGAN/INGAN

### 6.1 Introduction

M-plane  $AlGaN/GaN$  MQWs initially were used to study ISBA in nonpolar nitrides [36], [54], [55]. Far- and mid-IR ISBA on m-plane  $AlGaN/GaN$  MQWs produced by PA-MBE was reported by our group [32], [66], [83]. Monavarian et al. [56] recently reported ISB transitions with record small linewidths in m-plane  $AlGaN/GaN$  produced by ammonia MBE. However, due to the large lattice mismatch between nonpolar  $AlGaN$  and  $GaN$ , this MQW system is not scalable to thick devices, leaving a big challenge for applications. Furthermore, the growth of high Al mole fraction m-plane  $AlGaN$  leads to an unexpected obstacle [11], [57], [58]. It has been shown in our research that PA-MBE growth of  $AlGaN$  on m-plane  $GaN$  has an instability that inhibits the growth of planar, homogenous  $AlGaN$  alloys containing more than 60% Al [11], [32]. In an effort to overcome these challenges, we explore nearly strain-balanced (to  $GaN$ ) m-plane  $(In)AlGaN/InGaN$  MQWs. The tensile strain of  $AlGaN$  barriers is compensated by the compressive strain of  $InGaN$  wells in each period of QB/QW that results in a minimum strain accumulation in the epilayer relative to the  $GaN$  substrate. As a result, thick ISB structures can be grown for applications. Moreover, with large CBO, m-plane  $(In)AlGaN/InGaN$  MQW can give a near-IR ISBA while the Al-mole fraction is below 0.3 to avoid the  $AlGaN$  growth instability. Together, these intrinsic advantages make non-polar m-plane  $(In)AlGaN/InGaN$  a promising material combination for near-IR optoelectronic applications.

However, non-polar m-plane  $(In)AlGaN/InGaN$  MQWs present their own set of material development challenges, limiting research into their infrared properties. The ISBA in m-plane  $AlGaN/InGaN$  was first demonstrated by Pesach et al. [33], but no extensive experimental work has been published thereafter. We conducted a thorough methodical investigation of the impact of structural parameters on ISBA energy in m-plane  $(In)Al_xGa_{1-x}N/In_yGa_{1-y}N$  MQWs ( $x = 0.16 - 0.3, y = 0.16$ ) grown by PA-MBE. This study explores the effect of quantum well width, barrier Al-composition, and doping level on the mid-IR transition energy of non-polar  $(In)AlGaN/InGaN$  MQWs. Many-body corrections were added to the calculations in order to compare them with the experimental data. Due to a better prediction

of correlation effects, the local density approximation (LDA) shows a more accurate prediction of m-plane nitride ISBA energies than the Hartree-Fock approximation (HFA). With this study, our final goal is to evaluate the potential of non-polar m-plane  $(In)AlGaN/InGaN$  heterostructures for near-IR devices.

## 6.2 Results

All non-polar  $(In)AlGaN/InGaN$  samples were grown by PA-MBE on m-plane  $(10\bar{1}0)$ -oriented free-standing  $GaN$  substrates from Nanowin Science and Technologies. These substrates have a threading dislocation density of less than  $5 \times 10^6 \text{ cm}^{-2}$ , a RMS roughness of less than 0.3 nm over a  $4 \times 4 \text{ }\mu\text{m}^2$  area, and a miscut of  $-0.5^\circ \pm 0.2^\circ$  toward the c-direction. The substrates first went through a meticulous cleaning process to be ready for the long growth inside the MBE chamber. The MBE instrument provides gallium, aluminum, indium, and silicon through standard effusion cells, while nitrogen ( $N_2$ ) is produced by a Veeco Unibulb radio frequency plasma source operating at 300 W power with 0.5 sccm  $N_2$  flow rate. An approximately 150 nm  $GaN$  buffer layer was grown under gallium rich conditions at  $720^\circ\text{C}$  before growing the active layers for ISBA. All samples were grown at  $565^\circ\text{C}$  with an indium surfactant. More details about these growths are listed in [84]. With these growth conditions, Dzuba et al. have shown a development of coherently strained and homogeneous  $In_{0.16}Ga_{0.84}N$  growth up to 30 nm thickness [85], as well as improving  $AlGaN$  material homogeneity and surface roughness while decreasing interface roughness of  $AlGaN/InGaN$  [84]. However, due to the existence of an indium surfactant during the growth of homogeneous  $AlGaN$ , a small amount of unintentional indium was found in the barrier; thus, it is now called  $(In)AlGaN$  [84].

Table 6.1 includes structural details as well as ISBA data of different groups of samples that are considered in this study. While the indium incorporation in the barrier material occurred randomly during growth, the barrier thicknesses of the MQW structures were designed in order to minimize strain accumulation between layers as below,

$$\epsilon_b t_b + \epsilon_w t_w = 0, \quad (6.1)$$



where  $\epsilon_b$  and  $\epsilon_w$  are the strains in the barrier and well, respectively, while  $t_b$  and  $t_w$  are the thickness of each barrier and well in the MQW structure. Equation 6.1 uses the thickness-weighted method to estimate the barrier thickness of each layer under strain-balanced conditions. Moreover, since the strain is anisotropic on m-plane surface, it can not be completely balanced along both a- and c- axes simultaneously. Hence, the thickness used in each growth was chosen in-between the desired values suggested when balancing strain for the a- and c-axes. Two silicon  $\delta$ -doping sheets, that are placed in each barrier, 1 nm away from each interface, are the source of charge. The charge density is determined by the duration of silicon deposition.

Structural details of each sample were first revealed by the HRXRD method, measured by a Panalytical MRD X'Pert Pro high-resolution x-ray diffractometer. Software package Epitaxy 4.5a from Malvern PANanalytical was used to extract structural information. In order to obtain data from HRXRD, including alloy composition and layer thickness of both quantum wells and quantum barriers, we made the following assumptions in our modeling process. Firstly, the growth rate of *InGa*N is the same for the quantum well regions and bulk *InGa*N layers. Furthermore, we assumed that all Al atoms were incorporated during (*In*)*AlGa*N growth.

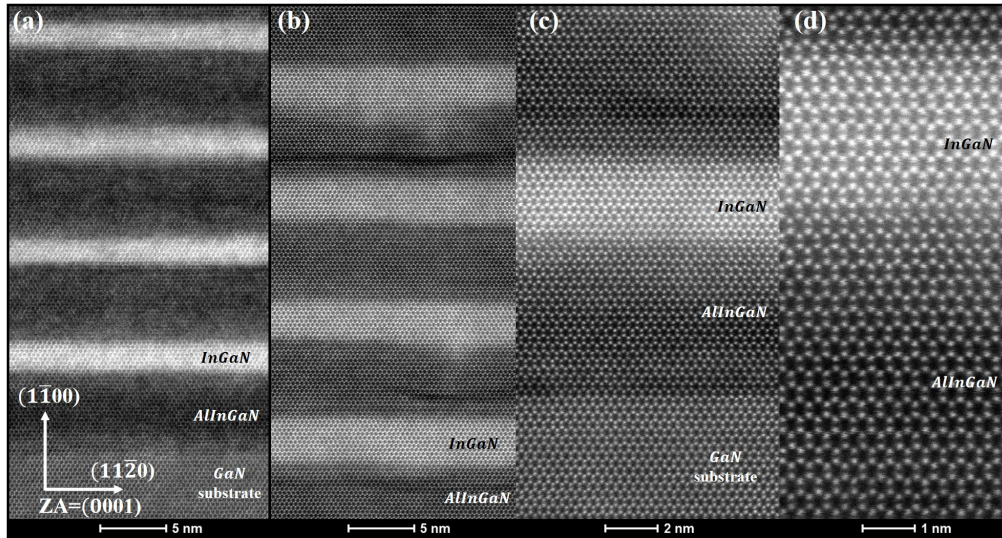


**Figure 6.1.** [Reprinted/Adapted] with permission from [59] ©Optica Publishing Group. HRHAADF-STEM of sample H (a) and B (b-d) [59]. The lighter the element, the darker contrast appears on HAADF-STEM images.

In addition to HRXRD data, HRHAADF-STEM was used to confirm the structural

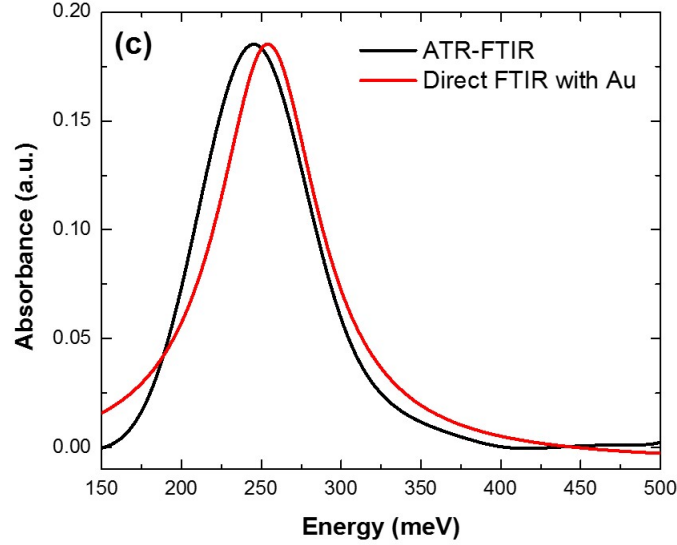


**Figure 6.2.** [Reprinted/Adapted] with permission from [59] ©Optica Publishing Group. ISBA spectra of sample A using direct-FT-IR (red curve) and ATR-FT-IR (black curve) method.

parameters of quantum wells and quantum barriers in selected samples. Figure 6.1 shows HRHAADF-STEM of samples H and D at different magnifications. The lamellae were prepared using an in situ lift-out technique with a Thermo Scientific Helios G4 UX Dual Beam focused ion beam. During this process, we used low energy Ga ion beams to etch the bulk material away, leaving an electron-transparent thin layer ( $< 100$  nm) for HRSTEM images. These lamellae then went through another milling procedure to clean up any damage resulting from FIB using a Fischione Nanomill Model 1040 at 900 eV and 120  $\mu$ A with  $\pm 10^\circ$  tilt. After that, to further reduce any possible contamination leftover from FIB and air, the lamellae underwent a one-hour cleaning process inside a Fischione Ar Plasma Cleaner, consisting of four 15-minute plasma cycles with a 5-minute break at the end of each cycle. This 5-minute break is crucial to cleaning up any contamination or material inside the chamber before starting another plasma period, resulting in clean lamellae for TEM imaging. The samples in Figure 6.1 show clear atom arrangements, indicating an effective sample preparation process with minimum ion-induced damage. HRHAADF-STEM images were taken using an aberration-corrected Thermo Scientific Themis Z microscope with the



beam condition of 300 kV, 0.24 nA, and 0.65 Å probe size. One of the advantages of this microscope is the image correction from astigmatism, spherical, coma, etc. up to 3<sup>rd</sup> order of aberration allowing clear images for post-analysis process. In addition, energy-dispersion x-ray spectroscopy (EDS) was performed to acquire 2D elemental maps of the epi-layers, leading to the alloy composition of QWs and QBs. However, due to low signal-to-noise and a large error bar for gallium, aluminium, and indium, results from EDS were only used for qualitative information. The alloy compositions listed in this study come from HRXRD analysis due to its  $\pm 1\%$  uncertainty of Al composition in the barrier. A combination of HRHAADF-STEM post analysis and HRXRD provides the thickness of QWs and QBs with an error bar of  $\pm 0.25$  nm. Furthermore, the contrast of HRHAADF-STEM also revealed any possible inhomogeneity in the active layers, e.g., the dark lines in Figure 6.1(a-c) represent high Al-composition regions.

**Table 6.1.** Summary of structural parameters, experimental results including ISBA energy peaks and FWHM of absorption peaks, and theoretical calculations of the transition energies for a series of m-plane (*In*)*AlGa*N/*InGa*N MQWs [59].

Sample (Group)	QB/QW thickness (nm)	QB/QW alloy composition	Calc. sheet charge density $\times 10^{12}$ $cm^{-2}/\delta$ - doping duration (s)	Experimental ISBA Energy Peak/FWHM (meV)		Calculated ISBA Energy (meV)	
				ATR	Direct	HFA	LDA
A (I)	7.5/2.8	$Al_{0.19}In_{0.06}Ga_{0.75}N/In_{0.16}Ga_{0.84}N$	5.37/10	246/65	254/77	342	285
B (I)	5.2/3.16	$Al_{0.3}Ga_{0.7}N/In_{0.16}Ga_{0.84}N$	5.73/10	303/86	329/89	364	293
C (I, II)	5.8/2.9	$Al_{0.24}In_{0.02}Ga_{0.74}N/In_{0.16}Ga_{0.84}N$	7.39/10	293/71	320/86	357	291
D (II)	5.8/2.9	$Al_{0.24}In_{0.02}Ga_{0.74}N/In_{0.16}Ga_{0.84}N$	8.01/20	284/124	340/104	359	291
E (II)	6/2.9	$Al_{0.24}In_{0.01}Ga_{0.75}N/In_{0.16}Ga_{0.84}N$	2.31/2	292/85	308/104	320	281
F (II, III)	6/2.9	$Al_{0.24}In_{0.02}Ga_{0.74}N/In_{0.16}Ga_{0.84}N$	5.62/5	288/85	303/55	348	290
G (III)	6/2.4	$Al_{0.24}In_{0.02}Ga_{0.74}N/In_{0.16}Ga_{0.84}N$	5.62/5	323/89	334/91	382	323
H (III)	6/2.1	$Al_{0.24}In_{0.03}Ga_{0.73}N/In_{0.16}Ga_{0.84}N$	5.52/5	336/218	360/324	394	337
I (III)	9/3.5	$Al_{0.24}In_{0.01}Ga_{0.75}N/In_{0.16}Ga_{0.84}N$	5.51/5	244/67	257/60	303	245

In this study, we exploited both direct-and ATR-FT-IR methods to obtain the ISBA spectra of our non-polar m-plane (*In*)*AlGa*N/*InGa*N MQWs. More details about these procedures are listed in the previous chapter 4. Figure 6.2 plots ISBA spectra of sample A

using direct- and ATR-FT-IR techniques. This particular sample was grown with only 15 periods of QWs, while other samples listed in Table 6.1 have 30 repeats of QB/QW. Thus, we added a 100 nm-thin layer of Au on top of the active region to enhance the ISBA intensity during the direct measurements [17]. Moreover, as mentioned previously, due to the possibility that the air gap at the interface between the Ge crystal and our  $(In)AlGaN/InGaN$  substrate unintentionally affects the absorption intensity, the ATR-FT-IR curve in Figure 6.2 was re-scaled to the same height as the direct-FT-IR curve. While ATR measurement of sample A gives an ISBA peak at 246 meV, direct measurement shows a similar peak at 254 meV. For this sample, the absorption energy from both approaches agree well with each other.

Table 6.1 lists the experimental and expected results of our series of non-polar m-plane  $(In)AlGaN/InGaN$ . Notice that the experimental ISBA peak energies from ATR-FT-IR are consistently lower than the values from direct-FT-IR. This phenomenon could be explained by the measurement geometry of the ATR technique. The penetration depth of the evanescent wave is proportional to wavelength; the longer the wavelength (lower energy), the larger the absorbance strength during ATR-FT-IR measurement. In contrast, in the direct-FT-IR measurement, an EM wave goes through the entire substrate. Hence, the ISBA peak is the result of not only the ISBA from our active region, but also defects in the free-standing  $GaN$  substrate. We list the results from both techniques in this study. However, more attention is needed to explain the origin of this energy discrepancy.

As mentioned above, in this study, we want to understand the ISBA of non-polar m-plane  $(In)AlGaN/InGaN$  to evaluate its potential for applications in the near-IR range. To pursue this goal, we conducted different investigations into the effects of material parameters on ISBT energy, including CBO, aluminum composition, activated charge density, and QW thickness. Samples are categorized into 3 groups, listed in Table 6.1. Group I contains samples A, B, and C, which were varied by Al-composition in the QBs. We expect to see an increase in CBO and ISBA energy as the Al-mole fraction is increased. Samples in group II are C, D, E, and F. They were grown with different doping levels to reflect the importance of activated charge density in ISBA theory [32]. Lastly, group III includes samples F, G, H, and I. These samples were designed with QW thickness variation to investigate the impact

of this parameter on the ISBA peak.

From a theoretical perspective, the barrier height (i.e., CBO) has a high impact on the ISBA energy of any MQW system with finite barriers. However, the CBOs of the non-polar m-plane  $(In)_yAl_xGa_{1-x-y}N/In_zGa_{1-z}N$  (with  $x < 0.3$  and  $z < 0.3$ ) are not yet well understood in current research. This becomes an obstacle for theoretical simulation to predict the ISBT energy of these heterostructures; thus, it deserves more investigation in the future. We use the available information for polar c-plane  $AlGaN/GaN$  and  $GaN/InGaN$  band offsets in the literature as the foundation for our calculations [6], [33], [86]–[95]. The CBO of  $Al_{0.25}Ga_{0.75}N/In_{0.16}Ga_{0.84}N$  heterostructure is listed approximately 512 meV. Figure 6.3 shows the dependence of the ISBT energy on CBO for the structure of sample F. While the black curve represents the variation of the bare transition energy as CBO is changed, the blue and red green curves show the corrected ISBA energy using HFA and LDA methods, respectively. Each of these curves has a band of error corresponding to the experimental uncertainty of QW width,  $\pm 0.25$  nm. The red curve displays the experimental ISBA energy using the direct-FT-IR technique. This curve also has a band of error that comes from a fitting uncertainty of  $\pm 20$  meV. In order to find an agreement between experimental and estimated ISBT energy, the HFA approach requires a CBO  $\leq 475$  meV, while LDA indicates  $420 \text{ meV} \leq \text{CBO} \leq 600 \text{ meV}$ . LDA method also agrees with our initial assumption of the polar c-plane  $AlGaN/GaN$  and  $GaN/InGaN$  band offsets. Therefore, we strongly believe that this is relevant evidence justifying that the LDA approach is more accurate than HFA to calculate many-body corrections in non-polar m-plane  $(In)AlGaN/InGaN$  MQWs.

As previously mentioned, samples in group I (A, B, and C) are used to study the effect of Al-composition on the ISBT energy of our heterostructures. Moreover, we are interested in identifying the Al mole fraction that gives near-IR ISBT with our current In-composition of  $InGaN$ . Simulations were done using the structure of sample A. The variation of QB was found to not affect the overall ISBT energy of the MQW system; therefore, we will compare all three samples, A, B, and C, with the theoretical curves in Figure 6.4. While the black curve indicates the bare transition energy inside QW, the red and blue curves are the many-body corrected ISBA energy estimated by the HFA and LDA approaches, respectively. Once again, LDA shows a more accurate prediction of ISBT energy than HFA, although neither

method was able to reproduce the experimental result perfectly.

Figure 6.1(b-d) reveals inhomogeneities in  $(In)AlGaN$  layers. The dark regions in  $(In)AlGaN$  layer indicate high Al-composition  $AlGaN$  resulting in inhomogeneous QBs. A similar phenomenon has been shown by our group as an obstacle for growing  $Al_xGa_{1-x}N$  with  $x \geq 0.6$  [11], [32]. The presence of inhomogeneities in QBs at low Al mole fraction in this study can be explained by a much lower growth temperature for indium incorporation purposes in QWs compared to our previous study on non-polar m-plane  $AlGaN/GaN$  [11], [84]. Although the interfaces of sample B remain unaffected by non-uniform regions in QBs, the existence of these areas hints at a negative effect on the ISBA spectrum due to inhomogeneous material and increased interface roughness as Al-composition gets higher.

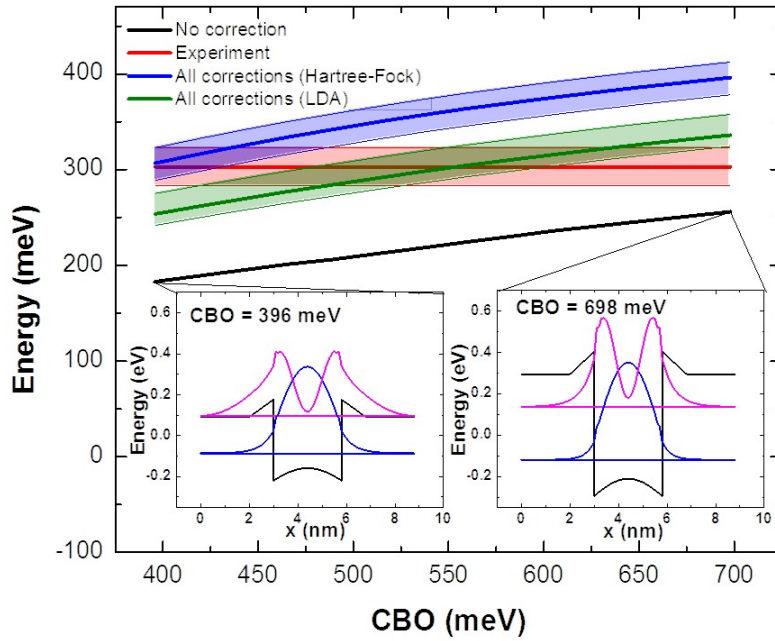


**Figure 6.3.** [Reprinted/Adapted] with permission from [59] ©Optica Publishing Group. Effect of CBO on expected ISBA energy with HFA and LDA approaches for a single QW using sample F's structure. The experimental ISBA energy of sample F from direct-FT-IR was used to compare with theoretical estimations. The insets represents the conduction band edge and two lowest energy states inside QW [59].

Nonetheless, the theoretical prediction was done to not only understand the behavior of our non-polar  $(In)AlGaN/InGaN$  heterostructures, but also guide us to a desired Al mole

fraction to obtain near-IR ISBT energies with given  $In_{0.16}Ga_{0.84}N$  QWs. Figure 6.4 only shows simulation of  $AlGaN$  up to 50% Al, which is enough to get near-IR ISBA energy suggested by HFA approach. However, LDA with more accurate calculations shows that it is not possible to achieve near-IR ISBA energy with an Al mole fraction  $\leq 0.5$ . Hence, with the limitation of growing homogeneous  $AlGaN$ , larger In-composition of  $InGaN$  is required to achieve higher ISBA energy and possibly near-IR absorption.

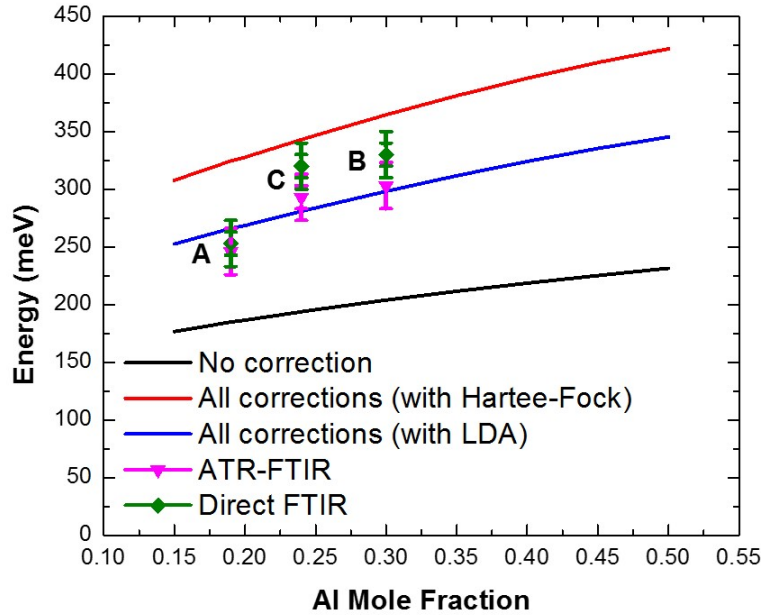


**Figure 6.4.** [Reprinted/Adapted] with permission from [59] ©Optica Publishing Group. Effect of aluminum mole fraction on calculated ISBA energy with HFA and LDA approaches. Samples in group I (A, B, and C) are plotted to compare with the theoretical estimation.

The second group of samples were grown with the same structural parameters, except  $\delta$ -doping level. The purpose of this study is to show the effect of the activated sheet charge density inside QWs on ISBA energy as well as its FWHM. Figure 6.5 shows the theoretical relationship between the transition energy and the charge density inside QWs. Again, we use both HFA, 6.5(a), and LDA, 6.5(b) approaches to calculate the total corrected ISBA energy in parallel. The black, blue, red, magenta, and green curves represent the transition energy without any correction, with excitonic term, with depolarization term, with exchange-correlation effect, and with total many-body correction, respectively. All samples in group

II (C, D, E, and F) are listed in each plot with an error bar of  $\pm 20$  meV that comes from the fitting uncertainty. A CBO of 512 meV was chosen for the simulation based on CBO values of c-plane nitride heterostructures. The theory shows that the ISBA energy increases as more charges are activated inside the QWs, then saturates at some high level of sheet charge density. HFA shows that this saturation point happens at a much higher sheet charge density than LDA. Furthermore, the higher doping density can lead to higher impurity scattering, affecting the FWHM of ISBA spectra because of the overlap of electron wavefunction inside QW and the doping layer. This phenomenon explains the peculiarly large FWHM of sample D. In comparison, HFA significantly overestimates the total corrected ISBA energy regardless of experimental technique, while LDA shows noticeably better agreement with the ATR-FT-IR result and underestimates the energy peak from the direc-FT-IR method. The discrepancy between the theoretical calculations comes from their different treatments of the exchange-correlation term. In [17], the correlation effect between electrons was underestimated by HFA but not by LDA. More theoretical details can be found in chapter 2. Our experimental data suggests that LDA gives a better prediction of ISBA energy due to its way of addressing the effect of both exchange and correlation on these materials.

Even though LDA adequately reproduces the experimental value from ATR-FT-IR, we showed that the ISBA peak can be affected by the penetration depth of the evanescent wave. Thus, we will focus on the disagreement between the results from direct-FT-IR and LDA. One of the culprits behind this small difference could be as simple as the uncertainty in measurements. All samples are in agreement within their error bars, except sample D. However, an inappropriate CBO that was used in the calculation process could also be the reason for this disparity. Therefore, we recommend a slightly higher CBO ( $> 512$  meV) is needed for our non-polar m-plane  $(In)AlGaN/InGaN$  MQW systems. This hypothesis has also been suggested in several reports for non-polar a-plane  $AlGaN/GaN$  [6], [33], [86]–[95]. According to these reports, the differences between c-plane and a-plane CBOs for  $AlGaN/GaN$  heterostructures are due to the adjustment of the built-in electric field in c-plane systems. Thus, a modified CBO would be all it takes for LDA to produce better quantitative agreement with the direct-FT-IR result. From our estimation, an increment of 16% in CBO would give excellent agreement between the suggested ISBA energy from

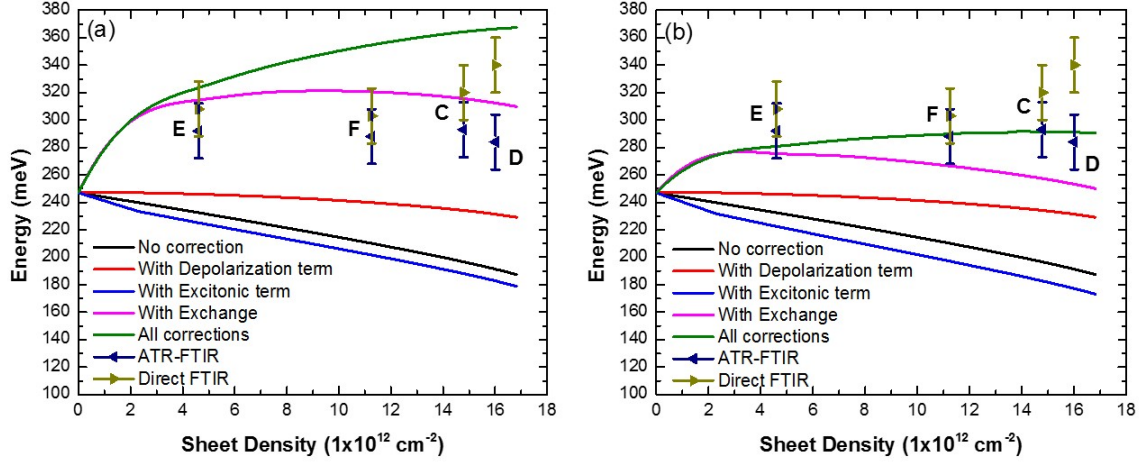


**Figure 6.5.** [Reprinted/Adapted] with permission from [59] ©Optica Publishing Group. Effect of sheet charge density on simulated ISBA energy using HFA (a) and LDA (b) methods. Samples in group II are listed for a comparison with the theoretical prediction [59].

LDA and direct-FT-IR experimental values. With results from two independent methods (i.e., HRXRD and HRHAADF-STEM), we are confident in the structural parameters of our heterostructures. Moreover, it is worth emphasizing again that the knowledge of CBO of these material combinations is still limited. Hence, we chose to use the CBO calculated from literature in this chapter.

Last but not least, we use our third group of samples (F, G, H, and I) to study the dependence of ISBA energy and FWHM on QW width. Similar to previous studies, samples in this group were grown with the same doping profile. The QB thickness is calculated to reach a nearly strain-balanced condition as we varied the QW width from 2.5 nm to 3.5 nm across samples. Figure 6.6 plots the theoretical estimation for ISBT energy using HFA and LDA in comparison with the experimental results from ATR- and direct-FT-IR methods. The black, blue, and red curves represent the calculation of ISBA without many-body effects, with many-body effects using LDA, and with many-body effects using HFA, respectively. While the magenta points are our experimental values obtained from the ATR-FT-IR technique,



the green points were collected using the direct-FT-IR method. All of these points have an error of  $\pm 20$  meV that comes from fitting uncertainty. Our experimental data follows the trend suggested by the calculations: the ISBT energy increases as the QW width decreases. Furthermore, LDA reproduces the experimental ISBT energy, while HFA overestimates it again. Because of the consistency of these theories on our MQW systems, we have high confidence in stating that LDA is more suitable for predicting the ISBA energies of non-polar III-nitrides than HFA.

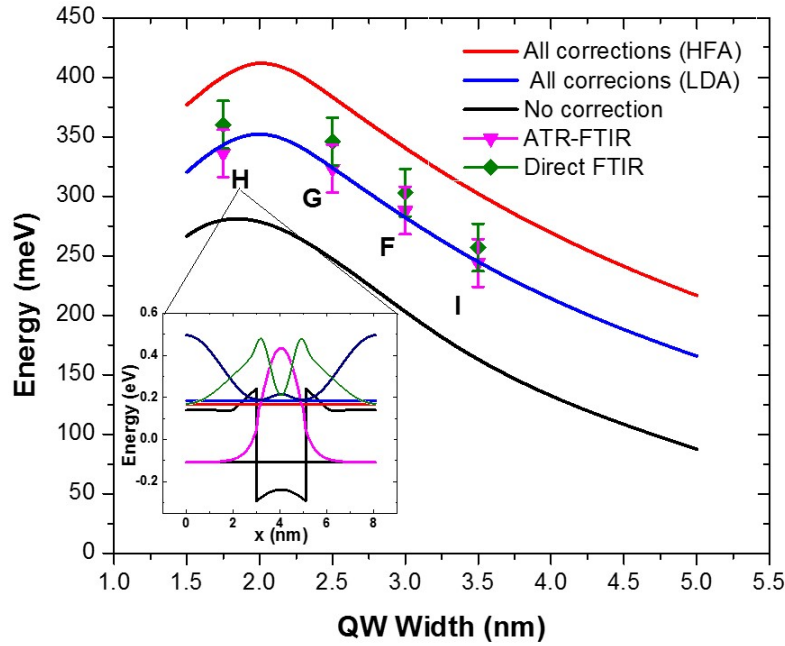


**Figure 6.6.** [Reprinted/Adapted] with permission from [59] ©Optica Publishing Group. The effect of QW width on ISBA energy simulated by HFA and LDA approaches. Samples in group III are used in comparison between experimental and theoretical results. The inset represents the simulated conduction band edge and electron wavefunction of the first 3 states of sample H [59].

Samples F, G, and I exhibit FWHMs comparable to the narrowest in this range of energy [54], [56]. This can be explained by low impurity scattering and relatively smooth interfaces between layers, as shown in Figure 6.1. However, the FWHM of sample H is unexpectedly large, e.g. 324 meV from direct-FT-IR. Sample H was grown with the thinnest QW width structure, leading to the ground and the first excited states inside QW sitting at higher



energies than other samples. The inset in Figure 6.6 indicates that the first excited state in the QW is sitting very close to the top of the barrier and only approximately 15 meV below the ground state of the electron in the barrier. Hence, the crossing between these states may result in a superlattice mini-band that broadens the ISBA spectrum of sample H.

### 6.3 Conclusion

For the first time, we reported in this study the ISBA in near strain-balanced non-polar m-plane  $(In)AlGaN/InGaN$  MQWs produced by PA-MBE. Experimental ISBA results are obtained using two different techniques, namely ATR-and direct-FT-IR. The ATR-FT-IR method routinely suggests a lower transition energy than that from direct-FT-IR. However, measurements from both techniques are in good agreement, as addressed in detail previously. Our heterostructures of  $(In)AlGaN/InGaN$  produce ISBAs in the range of 3.4 to 5.1  $\mu\text{m}$  with small FWHM that are comparable to the narrowest linewidths reported in the literature for non-polar m-plane  $AlGaN/GaN$  MQWs. Furthermore, our theoretical calculations show that CBO is a crucial factor in predicting the ISBT energies of non-polar m-plane  $(In)AlGaN/InGaN$ . We employed the recommended value of CBO from literature for c-plane nitride alloy in this section in all of our calculations, including HFA and LDA methods. While the HFA consistently overestimates the ISBT energy of our system, the LDA approach provides good agreement with the experimental results. The remaining discrepancy between expected and empirical values can be addressed by increasing CBO moderately. We also demonstrated the expected relationship between ISBA energy and structural factors, including charge density, QW thickness, and QB alloy composition (i.e., Al mole fraction). However, our current MQW systems yield ISBA energy outside of the technologically relevant near-IR range. In order to achieve the energy in this range, more research is required on higher CBO systems, e.g., higher indium composition in QWs.

## 7. SUMMARY

With the advantages of large CBO ( $> 1$  eV) and large LO-phonon energy, III-nitride semiconductors have been promising candidates for high-performance infrared optoelectronic devices. However, the challenges that come along with these materials, including large effective mass, internal polarization field, and high defect density, have made it hard to achieve the desired ISBA peak for applications.

As mentioned in chapter 1, III-nitrides have a large effective mass compared to arsenides, resulting in a low transition rate. A suggestion to overcome this obstacle is to increase the doping density ( $10^{12}$  atom/cm<sup>2</sup>). This action might help to enhance the absorption rate, but it also affects the ISBA energy peak through many-body effects. Fortunately, for c-plane *AlGa*N/*GaN*, the material parameters are well developed, so we can give a good prediction for the ISBA energy. Nonetheless, the extremely high doping density also gives rise to a large amount of impurity scattering that could result in a large FWHM of the ISBA spectrum. To further improve this obstacle, the effects of different doping schemes on ISBT energy have been studied. The optimal doping arrangement used for our samples consists of two  $\delta$ -doping sheets in the QB located 1 nm away from each side of the QW for *AlGa*N/*GaN* and (*In*)*AlGa*N/*InGa*N heterostructures and one or two  $\delta$ -doping sheets in the QW for *InAl*N/*GaN* MQWs. Furthermore, the reduction of doping from two sheets down to a single sheet in the polar c-plane lattice-matched *InAl*N/*GaN* has not been proven to improve the ISBT energy linewidth.

Another challenge of the III-nitride semiconductors is the internal polarization field. This field includes spontaneous polarization caused by the sum of dipole moments between nitrogen-metal bonds and a piezoelectric field from the lattice strain between layers of different materials along the c-direction. An attempt to reduce this internal polarization field is using polar c-plane lattice-matched *In*<sub>0.17</sub>*Ga*<sub>0.83</sub>N/*GaN*. We summarize the ISBA results of the c-plane lattice-matched *In*<sub>0.17</sub>*Al*<sub>0.83</sub>N/*GaN* later in this chapter in more detail. At lattice-matched conditions, we were able to eliminate the piezoelectric field that has been shown through the conduction bandedge calculated using Nextnano++. Furthermore, the result proves that the lattice-matched nitride semiconductors are promising materials for

near-IR ISBA applications. However, the difficulty of growing homogeneous  $InAlN$  material prevents us from achieving a small linewidth and a high transition rate for the ISBA spectrum. Another suggestion to overcome this obstacle is to grow our III-nitride materials along the non-polar m-direction. In the case of non-polar  $AlGaN/GaN$ , we were able to obtain the mid- and near-IR ISBA. Nonetheless, the growth instability of high Al-composition  $Al_xGa_{1-x}N$  ( $x \geq 0.6$ ) reported in reference [32] hinders strong infrared ISBA with narrow linewidth for these MQW systems. In the case of non-polar m-plane near strain-balanced  $(In)AlGaN/InGaN$ , our ISBA measurements show that this materials combination has high potential for applications in the range of 3.4 to 5.1  $\mu m$ . Although we could not reach a near-IR regime with our alloy combination, we were the first to report ISBA in non-polar near strain-balanced  $(In)AlGaN/InGaN$ . Moreover, unlike strained  $AlGaN/GaN$ , strain-balanced  $(In)AlGaN/InGaN$  allows a thick active region to be grown for making devices. Due to the limitation of inhomogeneity in  $(In)AlGaN$  with Al mole fraction  $\geq 0.3$ , in order to obtain a near-IR ISBA peak with this material combination, a higher In-composition (i.e., higher than 16%) in  $InGaN$  QW is required. We also discuss another attempt to reach a near-IR ISBA peak with a small linewidth using polar latticed-matched  $ScAlN/GaN$ .

## 7.1 Review of Past Work on Lattice-Matched $In_{0.17}Al_{0.83}N/GaN$ Heterostructures

Our group has demonstrated that polar lattice-matched  $InAlN/GaN$  heterostructures exhibit strong ISBAs [96]. This section discusses our recent research on polar c-plane lattice-matched  $In_{0.17}Al_{0.83}N/GaN$  heterostructures including some ISBA results and the challenges of growing homogeneous  $InAlN$ . Additionally, we show the effect of inhomogeneity in the  $InAlN$  layer on the ISBA spectra of  $InAlN/GaN$  superlattices. Polar c-plane lattice-matched  $In_{0.17}Al_{0.83}N/GaN$  MQWs were grown using PA-MBE on a thick  $GaN$  layer on a sapphire substrate with 15 periods of QB/QW and a QB at the end to ensure that each QW receives the same amount of charge from the doping layers. AFM and HRXRD were used to characterize the structure of each sample, while FT-IR was employed to obtain the ISBA spectrum.

Figure 7.1 shows the experimental ISBA of a c-plane  $InAlN/GaN$  superlattice obtained

by the direct-FT-IR method. While the HFA predicted transition energy is 520 meV, the FT-IR absorption spectrum indicates that  $E_{ISB} = 547$  meV shown in Figure 7.1. This result shows good agreement between the experimental and calculated values for the ISBA energy, which is consistent with our prior report by Edmunds et al. [97]. However, due to the honeycomb nanostructures in the  $InAlN$  layer, a high doping density located inside the QW is required in order to observe the ISBTs. This requirement results in a broad absorption spectrum with a large FWHM; for example, the ISBA spectrum in Figure 7.1 has a FWHM of 140 meV.

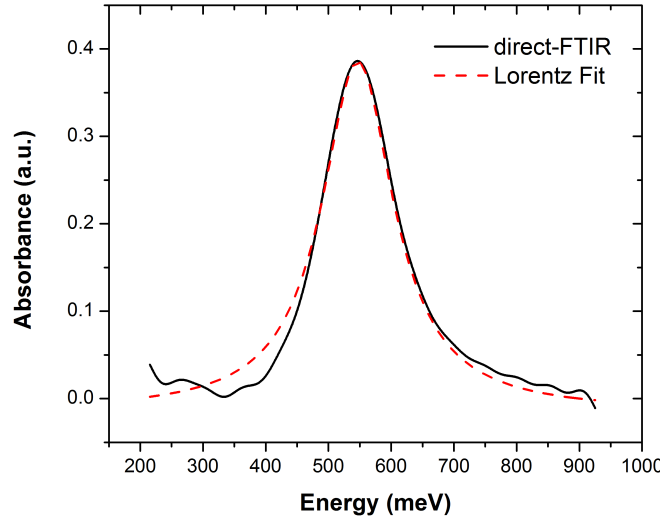


**Figure 7.1.** Experimental ISB transition spectrum of a c-plane 15-period  $In_{0.15}Al_{0.85}N/GaN$  SL with the QW thickness of 3.15 nm and the barrier thickness of 4.88 nm. The ISBA curve has its peak located at 547 meV with a FWHM of 140 meV.

Moreover, homogenous  $InAlN$  still remains difficult to achieve. Up to date, there is only one group that has published evidence of homogeneous  $InAlN$  [98]. A wide range of bulk  $InAlN$  growth conditions, including temperature and nitrogen flux, were explored to improve the homogeneity of this material [99]. Plan-view HRSTEM results suggest that not only the honeycomb nanostructures are still present in all samples but also  $InAlN$  forms larger cells at higher nitrogen flux [99]. Furthermore, these cells have open boundaries that make the structures more irregular compared to the lower nitrogen flux condition. Figure 7.2 shows plan-view HAADF-HRSTEM images containing evidence of honeycomb nanos-

structures in bulk  $InAlN$  grown over a wide range of temperatures and nitrogen flux. In this figure, the brighter regions have high In concentration, and the darker regions indicate high Al concentration areas. The In-compositions of these samples were determined by HRXRD measurements and varied from 15.4% (7.2b) to 17.4% (7.2a).

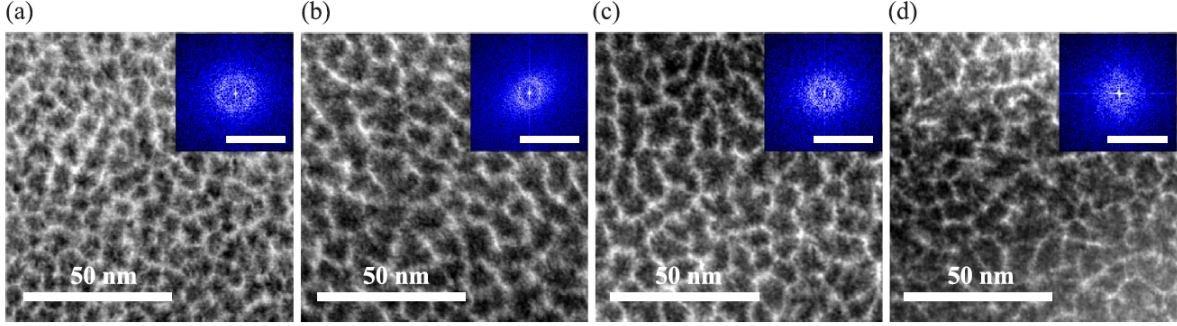


**Figure 7.2.** Plan-view HAADF-STEM image of a 30nm-thick  $InAlN$  c-plane samples grown at nitrogen flux (a)  $1.75 \times 10^{14}$ , (b)  $4.23 \times 10^{14}$ , (c)  $6.42 \times 10^{14}$ , and (d)  $1.26 \times 10^{15} \text{ atom/cm}^2 \text{ s}$ . Honeycomb cells consist of indium-rich borders and aluminum-rich centers [99].

The ISBA results from lattice-matched  $In_{0.17}Al_{0.83}N/GaN$  heterostructures are promising as an alternative to polar c-plane  $AlGaN/GaN$  SLs for high-performance ISB devices. However, due to the existence of nanostructures inside the  $InAlN$  layer, which act as defects and charge traps [96], a high doping scheme was placed inside the QW in order to obtain a strong ISBA intensity. This requirement leads to a large amount of impurity scattering, hence the broad ISBA spectrum. Furthermore, the homogenous  $InAlN$  still remains a challenging goal to achieve. Moreover, there is not a good agreement between the experimental and calculated results for the ISBA amplitude. A possible explanation is the effect of the honeycomb nanostructures [96]. While the simulation assumes the In and Al atoms are randomly distributed in the barrier, the unique nanostructures suggest that the regions with high Al-composition dominate the ISBA spectrum. As calculated, high Al-composition regions in  $InAlN$  layer lead to a larger CBO and a larger ISBT energy. This effect results in a higher energy ISB absorption peak from the experimental result compared to the calculation using the average composition of In and Al throughout the sample [96].

## 7.2 Future Work

While non-polar m-plane  $(In)AlGaN/InGaN$  heterostructures exhibit narrow linewidth IBSA spectra in the mid-IR range, the near-IR is still a challenging range for infrared optoelectronic applications. Overall, our polar lattice-matched  $InAlN/GaN$  superlattices show promising near-IR ISBAs. We are planning to overcome the limitation of growing homogeneous material in polar  $InAlN$  by employing polar c-plane  $Sc_{0.19}Al_{0.71}N$  which is lattice-matched to  $GaN$  [100], [101].  $ScAlN$  has been shown to have a wide bandgap (5.6 eV) that can lead to a large CBO (1.74 eV) for obtaining near-IR ISBA [101], [102].

Our study on  $ScAlN$  is still work in progress. There are reports in the literature that  $ScAlN$  can exist in a combination of rock-salt and wurtzite crystal structures. At low  $Sc$  composition ( $< 0.4$ ),  $ScAlN$  is stable under wurzite structure, and starts switching phase at higher mole fraction [103], [104]. A series of polar  $Sc_xAl_{1-x}N/GaN$  superlattices were grown using PA-MBE technique with  $x = 15 \pm 1\%$  determined by Rutherford Back Scattering (RBS) at EAG Laboratories. We report for the first time near-IR ISBA in  $Sc_{0.15}Al_{0.85}N/GaN$  superlattices in this section.

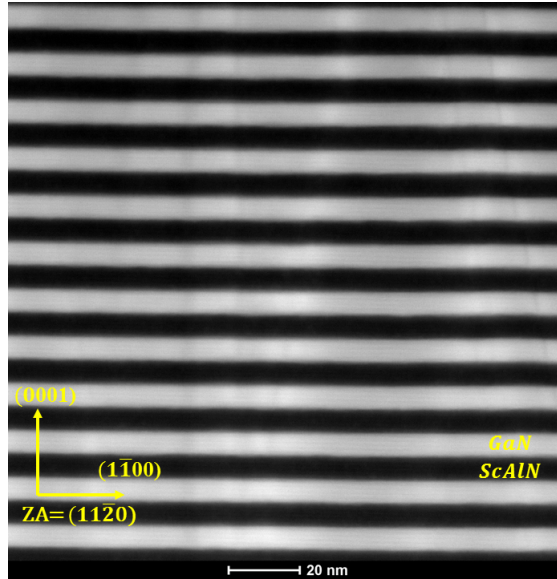


**Figure 7.3.** HAADF-HRSTEM of sample D. The dark (bright) layers are  $ScAlN$  ( $GaN$ ) layers.

HRHAADF-STEM was utilized to investigate several structural characteristics of our

polar  $ScAlN/GaN$  superlattices, including the layer thicknesses, interface roughness, and possible inhomogeneity. Figure 7.3 shows HRSTEM a cross-section view of sample D. Interfaces between layers are smooth and uniform, resulting in a constant QW thickness across the sample, hence small ISBA linewidths. Given that our  $ScAlN/GaN$  heterostructures were grown using the same alloy compositions but with varying doping durations or  $GaN$  thicknesses, we anticipate that all samples will exhibit a similar level of uniform interface roughness. The lamella was prepared using an in situ lift-out technique with a Thermo Scientific Helios G4 UX Dual Beam FIB. Small energy ion beams were employed to etch away the bulk material, leaving a thin lamella with a thickness of around 200 nm. The standard intended thickness of a lamella created by FIB is 100 nm or below. However, to minimize any unforeseen severe damage caused by FIB, we purposefully left the lamella relatively thick in comparison to normal. The specimen was then further thinned down to remove any FIB damage using a Fischione Nanomill Model 1040 operating at 900 eV, 120  $\mu A$ , and  $\pm 10^\circ$  tilt at low temperature. Following that, the lamella was cleaned with a Fischione Ar Plasma Cleaner to remove any contamination left over from the FIB and air. HRHAADF-STEM images were acquired using an aberration-correction Thermo Scientific Themis Z microscope with the beam condition of 300 kV, 0.24 nA, and 0.65 Å probe size.

**Table 7.1.** Summary of the structural parameters and the experimental results including ISBA energy peaks and FWHM of absorption peaks for a series of polar c-plane (near) lattice-matched  $Sc_{0.15}Al_{0.85}N/GaN$  MQWs.

Sample (Group)	ATR-FT-IR		Direct-FT-IR		QW(nm)	Doping duration(s)
	Peak (meV)	FWHM (meV)	Peak (meV)	FWHM (meV)		
A (I)	x	x	609	69	4	20
B (I)	x	x	616	32	4	5
C (I, II)	605	45	611	50	4	10
D (II)	559	31	568	50	6	10
E (II)	516	40	522	52	8	10

Due to the early stage of material development, various structural parameters of polar  $Sc_{0.15}Al_{0.85}N$  are unknown, which prevents us from precisely calculating the ISBA energy of these SLs accurately. Fortunately, we were able to build our own set of database pa-



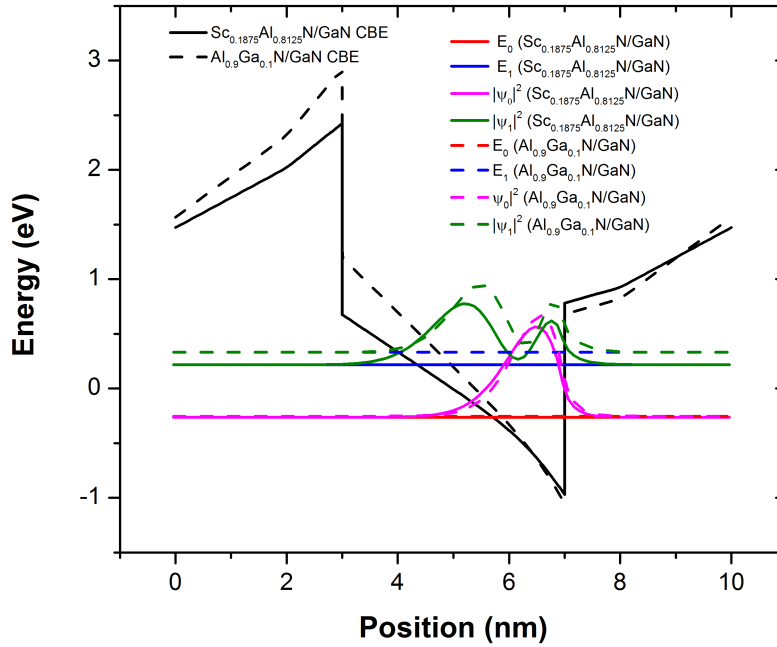
rameters for polar c-plane lattice-matched  $Sc_{0.1875}Al_{0.8125}$ . We calculated the ISBA energy of polar c-plane lattice-matched  $Sc_{0.1875}Al_{0.8125}N/GaN$  heterostructures using reported results from multiple publications [100]–[102], [105]–[107]. The theoretical lattice constants for  $Sc_{0.1875}Al_{0.8125}N$  along the a- and c-axes that we employed in our computations are 3.19145 Å and 5.02327 Å, respectively [100]. Reference [106] provided the dielectric constants. Zhang et al. determined the band gap of  $Sc_{0.1875}Al_{0.8125}N$  to be 5.58039 eV, while Fu et al. determined the CBO of  $Sc_{0.1875}Al_{0.8125}N/GaN$  to be 1.74 eV [101], [102]. Caro et al. reported the piezoelectric constants and spontaneous polarization for  $Sc_{0.1875}Al_{0.8125}N$  as  $e_{31} = -0.680707$ ,  $e_{33} = 1.82178$ ,  $e_{15} = -0.339223$ , and  $P_{SP} = 0.123301$  for  $Sc_{0.15}Al_{0.85}N$  [105]; while Ambacher et al. provided the pyroelectric constant in reference [107]. Since there are no reports in the literature describing the experimental or expected ISBA energies of polar  $ScAlN/GaN$  MQWs, we grew a series of samples to examine and understand the ISBA results as well as their behavior in the near IR-range for these heterostructures. Table 7.1 contains structural information as well as ISBA data for two groups of samples covered in this section. Group I consists of samples A, B, and C that were doped at varying levels in order to examine the dependence of the ISBA energy on activated charge density and to determine the optimal doping duration for future growth. Samples C, D, and E of group II were grown with varying QW widths to determine the impact of layer thickness on the ISBA energy and to narrow down the desired ISB absorption energy range for application purposes.

Figure 7.4 shows a comparison of the conduction band edges of c-plane  $Sc_{0.1875}Al_{0.8125}N/-GaN$  (solid lines) and c-plane  $Al_{0.9}Ga_{0.1}N/GaN$  (dash-lines) as well as their energy levels and probability amplitudes of the ground and the first excited states. We used polar  $Al_{0.9}Ga_{0.1}N/GaN$  in this comparison because it has a CBO of 1.73 meV, which is equivalent to the CBO of polar  $Sc_{0.1875}Al_{0.8125}N/GaN$ . This comparison demonstrates the difference in internal polarization field strength between these two heterostructures.

Similar to the study of non-polar strain-balanced  $(In)AlGaN/InGaN$ , we used both direct- and ATR-FT-IR methods to obtain the ISBA spectra of our polar  $ScAlN/GaN$  superlattices. However, due to the limitation of penetration depth, the signal-to-noise ratio from ATR-FT-IR is typically small for these superlattices. More details about these pro-



cedures are listed in chapter 4. Samples A and B were not reported with the ATR-FT-IR technique due to their low signal-to-noise ratios. There is very good agreement between ATR- and direct-FT-IR measurements for every sample.



**Figure 7.4.** Conduction band edges, energy levels, and probability amplitudes of the ground state and the first excited state of c-plane  $Sc_{0.1875}Al_{0.8125}N/GaN$  (solid lines) and c-plane  $Al_{0.9}Ga_{0.1}N/GaN$  (dash-lines) 10 s  $\delta$ -doping at 1 nm away from the QW with the well of 4 nm and the barrier of 6 nm.

First, we examine the dependence of the ISBA energy on the activated sheet charge density inside the QWs within samples A, B, and C. Samples in group I were grown with identical structural parameters except for the  $\delta$ -doping level. The duration of doping for each sample is provided in Table 7.1. The ISBA peaks of these samples are quite close to each other, indicating that the ISBA energy has already been saturated. This implies that the difference in doping between samples A, B, and C does not result in a significant ISBA energy change. Figure 7.5 shows the ISBA spectra of samples A, B, and C, which were measured by the direct-FT-IR technique (solid lines) and their Lorentzian fits (dash-lines). The different absorption intensities between these samples can be attributed to their varying amounts of doping. As discussed in chapter 2, the higher the doping level, the stronger the ISBT signal. Additionally, the FWHMs of samples A, B, and C are fairly small, with sam-

ple having the narrowest linewidth of 32 meV. This is the smallest FWHM reported in the literature for the ISBA in any nitride heterostructures in the near-IR range. Furthermore, as the doping duration increases from 5 s to 20 s, the activated charge level inside the QW also increases, resulting in larger FWHMs due to higher impurity scattering as addressed in section 2.3. Overall, the FWHM of our  $Sc_{0.15}Al_{0.85}N/GaN$  heterostructures is comparable to those of strained  $Al(Ga)N/GaN$  and near strain-balanced  $InAlGaN/InGaN$  [35], [59]. We may conclude that two sheets of  $\delta$ -doping placed 1 nm from the QW are required to achieve a small ISBA linewidth with a significant absorption for  $Sc_{0.15}Al_{0.85}N/GaN$  superlattices.

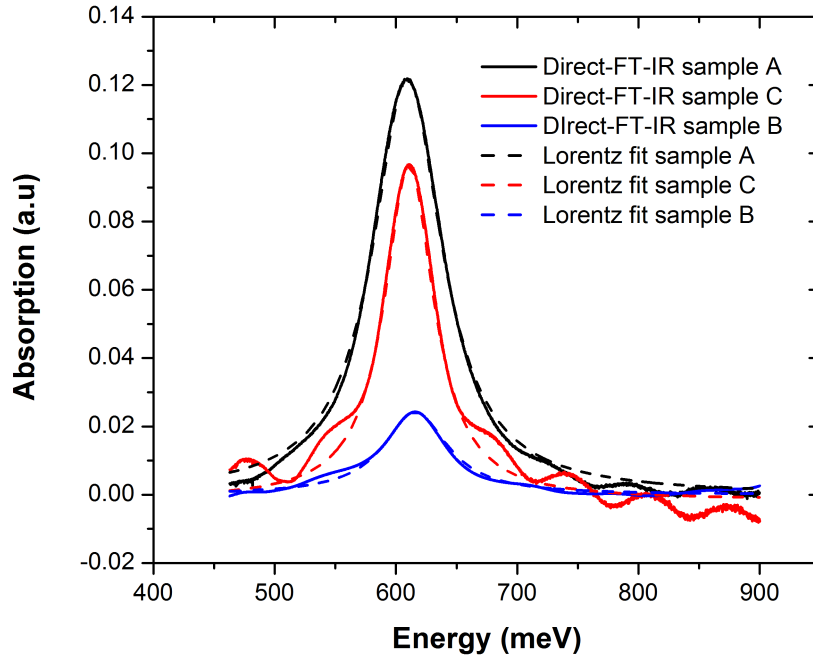


**Figure 7.5.** Experimental ISBA spectra of samples A (black), B (blue), and C (red) with ISBA peaks at 609 meV, 617 meV, and 611 meV, corresponding to FWHMs of 69 meV, 32 meV, and 44 meV respectively. The direct-FT-IR technique was used to obtain these spectra.

Next, we discuss the influence of QW thickness on the ISBA energy for  $ScAlN/GaN$  heterostructures. Samples C, D, and E were grown with the same doping level, alloy compositions, and QW width of 4 nm, 6 nm, and 8 nm, respectively. The ISBA spectra of these samples, provided by the direct-FT-IR measurements (solid lines), and their Lorentzian fits (dash-lines), are shown in Figure 7.6(left). The ISBA energy is expected to follow the theoret-

ical pattern shown in Figure 7.6(right). The blue and red curves are the exchange-correlation correction and total many-body corrections, respectively, using HFA (solid line) and LDA (dash-lines). The experimental points in Figure 7.6(right) have an error bar coming from fitting uncertainty of  $\pm 20$  meV. The QW thicknesses of samples E, D, and C were determined using HRXRD to be 8 nm, 6 nm, and 4 nm, corresponding to ISBA peaks at 611 meV, 568 meV, and 522 meV, respectively. The results of direct- and ATR-FT-IR measurements are in good agreement. While there are several reports of narrow linewidths in mid-IR [35], [56] for strained  $AlGaN/GaN$  heterostructures, there is still a lack of material combinations that yield comparable linewidths in the near-IR range. The ISBA spectra of samples from group II exhibit a narrow FWHM (50 meV - 52 meV), but also the ISBA peaks are well within the near-IR range (522 meV - 611 meV). This is the first indication that this material combination is potentially useful for near-IR devices.

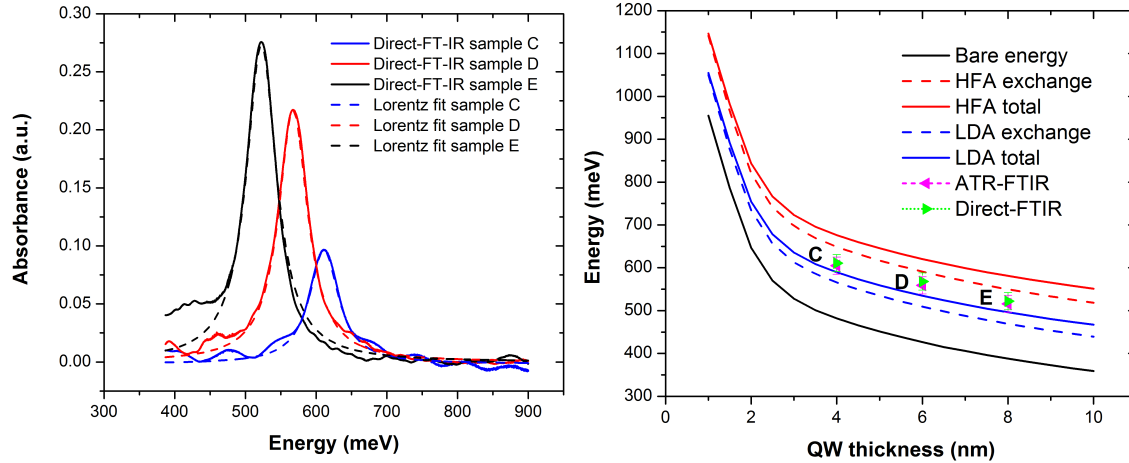


**Figure 7.6.** Experimental ISBA spectra of group II samples (left) and the effect of QW width on the ISBA energy (right). The theoretical calculations were done with polar c-plane  $Sc_{0.1875}Al_{0.8125}N/GaN$ ,  $10^{18}$   $\delta$ -doping at 1 nm in the QB away from each side of the QW.

Polar lattice-matched  $ScAlN/GaN$  is desirable for near-IR ISBA applications due to its large CBO. A series of polar near lattice-matched  $Sc_{0.15}Al_{0.85}N/GaN$  MQWs were grown by PA-MBE with varying doping levels and QW thickness. Despite the fact that this material is still under development and not completely understood, we were able to obtain near-IR ISBA with narrow linewidths on all of these superlattices for the first time. Additionally,

the ISBA data were collected using two different techniques, namely ATR- and direct-FT-IR, with excellent agreement between the two. This result is our first evidence that polar *ScAlN/GaN* heterostructures are suitable for near-IR ISBA applications because of their ISBA energy and narrow linewidth. However, additional experimental and theoretical research on this material combination is required to understand its structural and optical properties and hence make a more accurate prediction of its ISBA energy.

## REFERENCES

- [1] S. Nakamura, M. Senoh, N. Iwasa, and S.-I. Nagahama, “High-brightness *InGaN* blue, green and yellow light emitting diodes with quantum well structures,” *Japan Journal Applied Physics*, vol. 34, pp. 797–799, 7A 1995.
- [2] S. Nakamura, “*InGaN*–*AlGaN* blue-light-emitting diodes,” *Journal of Vacuum Science & Technology A*, vol. 13, p. 705, 3 1995.
- [3] S. Nakamura, T. Mukai, and M. Senoh, “High-brightness *InGaN/AlGaN* double-heterostructure blue-green-light-emitting diodes,” *Journal of Applied Physics*, vol. 76, pp. 8189–8191, 12 1994.
- [4] S. Nakamura, “Growth of  $In_xGa_{1-x}N$  compound semiconductors and high-power *InGaN*–*AlGaN* double heterostructure violet-light-emitting diodes,” *Microelectronics Journal*, vol. 25, pp. 651–659, 8 1994.
- [5] S. Nakamura, T. Mukai, and M. Senoh, “Candela-class high-brightness *InGaN*–*AlGaN* double-heterostructure blue-light-emitting diodes,” *Applied Physics Letters*, vol. 64, pp. 1687–1689, 13 1994.
- [6] D. Feezell and S. Nakamura, “Invention, development, and status of the blue light-emitting diode, the enabler of solid state lighting,” *Comptes Rendus Physique*, vol. 19, pp. 113–133, 3 2018.
- [7] H. L. Buijs, L. Rochette, and F. Chateaneuf, “Evolution of FTIR technology as applied to chemical detection and quantification,” *Chemical and Biological Point for Homeland Defense*, vol. 5269, pp. 132–142, 2004.
- [8] G. Bellisola and C. Sorio, “Infrared spectroscopy and microscopy in cancer research and diagnosis,” *American Journal of Cancer Research*, vol. 2, pp. 1–21, 1 2012.
- [9] S. G. Demos, R. Gandour, R. Edwards, R. Ramsamooj, and R. deVere White, “Spectroscopic detection of bladder cancer using near-infrared imaging techniques,” *Journals of Biomedical Optics*, vol. 9, p. 587, 4 2004.
- [10] T. Ando, “Density-functional calculation of subband structure on semiconductor surfaces,” *Surface Science*, vol. 58, pp. 128–134, 1 1976.
- [11] M. Shirazi-HD, R. E. Diaz, T. Nguyen, J. Jian, G. C. Gardner, H. Wang, M. J. Manfra, and O. Malis, “Kinetic instability of *AlGaN* alloys during MBE growth under metal-rich conditions on m-plane *GaN* miscut towards the -c axis,” *Journal of Applied Physics*, vol. 123, p. 161 581, 16 2018.

- [12] Z. Liliental-Weber, J. Jasinski, and D. N. Zakharov, “*GaN* grown in polar and non-polar directions,” *Opto-electronics Review*, vol. 12, pp. 339–346, 4 2004.
- [13] R. J. Molnar, W. Gtz, L. T. Romano, and N. M. Johnson, “Growth of gallium nitride by hydride vapor-phase epitaxy,” *Journals of Crystal Growth*, vol. 178, pp. 147–156, 1–2 1997.
- [14] T. Paskova, D. A. Hanser, and K. R. Evans, “*GaN* substrates for III-nitride devices,” *Proceedings of the IEEE*, vol. 98, pp. 1324–1338, 7 2010.
- [15] H. Sasaki, H. Sunakawa, N. Sumi, K. Yamamot, and A. Usui, “Fabrication of freestanding m-plane *GaN* wafer by using hvpe technique on an aluminum carbide buffer layer on an m-plane sapphire substrate,” *Journals of Crystal Growth*, vol. 311, pp. 2910–2913, 10 2009.
- [16] W. Neumann, A. Mogilatenko, T. Wernicke, E. Richter, M. Weyers, and M. Kneissl, “Structure investigations of nonpolar *GaN* layers,” *Journals of Microscopy*, vol. 237, pp. 308–313, 3 2009.
- [17] H. C. Liu and F. Capasso, *Intersubband transitions in quantum Wells: physics and device applications I-semiconductors and semimetals Vol.62*. Academic press, 2000.
- [18] B. Jogai, “Effect of many-body corrections on intersubband optical transitions in *GaAs–Al<sub>x</sub>Ga<sub>1–x</sub>As* multiple quantumw ells,” *Journal of Vacuum Science & technology B: Microelectronics and Nannometer Structures Processing*, vol. 9, p. 2473, 5 1991.
- [19] J. Perdew, “Local Density Approximation,” in *Centre Europeen de CAlcul Atomique et Moleculaire, Teaching the Theory in Density Functional Theory*, 2017.
- [20] E. Coronado, B. S. Tsukerblat, and R. Georges, *Molecular Magnetism: From Molecular Assemblies to the Devices*, ser. E-Applied Sciences. Boston: Springer, 1996, vol. 321.
- [21] P. R. Tupil, “Dielectric and lattice dynamical properties of molecular crystals via density functional perturbation theory: Implementation within a first principles code,” Ph.D. dissertation, University of Durham, 2004.
- [22] K. M. S. Bandara, D. D. Coon, Y. F. L. Byungsung O, and M. H. Francombe, “Exchange interactions in quantum well subbands,” *Applied Physics Letters*, vol. 53, pp. 1931–1933, 20 1988.
- [23] P.-H. Heenen and M. R. Godefroid, *The Hartree-Fock method*, 2012.
- [24] M. O. Manasreh, F. Szmulowicz, K. R. E. D. W. Fischer, and C. E. Stutz, “Intersubband infrared absorption in a *GaAs/Al<sub>0.3</sub>Ga<sub>0.7</sub>As* quantum well structure,” *Applied Physics Letters*, vol. 57, p. 1790, 17 1990.

- [25] L. Heldin and B. I. Lundqvist, “Explicit local exchange-correlation potentials,” *Journal of Physics C: Solid State Physics*, vol. 4, pp. 2064–2085, 1971.
- [26] W. Kohn and L. J. Sham, “Self-consistent equations including exchange and correlation effects,” *Physical Review*, vol. 140, A1133–A1138, 4A 1965.
- [27] W. L. Bloss, “Effects of Hartree, exchange, and correlation energy on intersubband transitions,” *Journal of Applied Physics*, vol. 66, pp. 3639–3642, 8 1989.
- [28] S. J. Allen and D. C. Tsui, “On the absorption of infrared radiation by electrons in semiconductor inversion layers,” *Solid-State Communications*, vol. 20, pp. 425–428, 4 1976.
- [29] A. Grier, J. D. Cooper, L. Lever, A. Valavanis, Z. Ikonic, D. Indjin, P. Harrison, M. Cervantes, C. Edmunds, J. Shao, L. Tang, D. Li, M. J. Manfra, and O. Malis, “A scattering rate approach to the understanding of absorption line broadening in near-infrared  $AlGaN - GaN$  quantum wells,” *6th Space Agency - MOD Workshop on Wideband Gap Semiconductors and Components*, 2012.
- [30] M. Beeler, E. Trichas, and E. Monroy, “III-nitride semiconductors for intersubband optoelectronics: A review,” *Semiconductor Science and Technology*, vol. 28, pp. 074 022–074 049, 7 2013.
- [31] J. Wu, “When group III-nitrides go infrared: New properties and perspectives,” *Journal of Applied Physics*, vol. 106, pp. 01 101–01 130, 1 2009.
- [32] T. Nguyen, M. Shirazi-Hosseini-Dokht, Y. Cao, R. E. Diaz, G. Gardner, M. J. Manfra, and O. Malis, “Intersubband transitions in nonpolar m-plane  $AlGaN - GaN$  heterostructures,” *Physica Status Solidi A*, vol. 215, pp. 1 700 828–1 700 835, 13 2018.
- [33] A. Pesach, E. Gross, C. -Y. Huang, Y. -D. Lin, S. E. Schacham, S. Nakamura, and G. Bahir, “Non-polar m-plane intersubband based  $InGaN/(Al)GaN$  quantum well infrared photodetectors,” *Applied Physics Letters*, vol. 103, pp. 022 110–022 115, 2 2013.
- [34] J. S. Speck and S. F. Chichibu, “Nonpolar and semipolar group III nitride-based materials,” *MRS Bulletin*, vol. 34, p. 304, 5 2009.
- [35] A. Ajay and E. Monroy, “Intersubband transitions in  $GaN$ -based heterostructures,” *Mid-infrared Optoelectronics*, pp. 539–565, 2020.
- [36] C. B. Lim, M. Beeler, A. Jay, J. Lahnemann, E. Bellet-Amalric, C. Bougerol, and E. Monroy, “Intersubband transitions in nonpolar  $GaN/Al(GaN)$  heterostructures in the short- and mid-wavelength infrared regions,” *Journal of Applied Physics*, vol. 118, pp. 014 309–014 318, 1 2015.

- [37] G. Chen, X. Q. Wang, X. Rong, P. Wang, F. J. Xu, N. Tang, Z. X. Qin, Y. H. Chen, and B. Shen, “Intersubband transitions in gan-ingan multiple quantum wells,” *Scientific Reports*, vol. 5, p. 11 485, 2015.
- [38] M. Li, Y. W. Lu, D. B. Li, X. X. Han, Q. S. Zhu, X. L. Liu, and Z. G. Wang, “Effect of spontaneous and piezoelectric polarization on intersubband transition in  $Al_xGa_{1-x}N - GaN$  quantum well,” *Journal of Vacuum Science & Technology B*, vol. 22, pp. 2568–2575, 6 2004.
- [39] Kishino, A. Kikuchi, H. Kanazawa, and T. Tachibana, “Intersubband transition in  $(GaN)_m - (AlN)_n$  superlattices in the wavelength range from 1.08 to 1.61  $\mu m$ ,” *Applied Physics Letters*, vol. 81, pp. 1234–1238, 7 2002.
- [40] D. Feezell, Y. Sharma, and S. Krishna, “Optical properties of nonpolar III-nitrides for intersubband photodetectors,” *Journal Apllied Physics*, vol. 113, pp. 1 133 103–1 133 111, 13 2013.
- [41] P. K. Kandaswamy, F. Guillot, E. Bellet-Amalric, E. Monroy, L. Nevou, M. Tchernycheva, A. Michon, F. H. Julien, E. Baumann, F. R. Giorgetta, D. Hofstetter, T. Remmele, M. Albrecht, S. Birner, and L. S. Dang, “ $GaN/AlN$  short-period superlattices for intersubband optoelectronics: A systematic study of their epitaxial growth, design, and performance,” *Journal of Applied Physics*, vol. 104, p. 093 501, 9 2008.
- [42] F. Guillot, B. Amstatt, E. Bellet-Amalric, E. Monroy, L. and L. Doyennette, F. H. Julien, and L. S. Dang, “Effect of Si doping on  $GaN/AlN$  multiple-quantum-well structures for intersubband optoelectronics at telecommunication wavelengths,” *Superlattices and Microstructures*, vol. 40, pp. 306–312, 4-6 2006.
- [43] N. Iizuka, K. Kaneko, and N. Suzuki, “Near-infrared intersubband absorption in  $GaN/AlN$  quantum wells grown by molecular beam epitaxy,” *Applied Physics Letters*, vol. 81, p. 1803, 10 2002.
- [44] K. Kishino, A. Kikuchi, H. Kanazawa, and T. Tachibana, “Intersubband transition in  $((GaN)_m/(AlN)_n)$  superlattices in the wavelength from 1.08 1.61  $\mu m$ ,” *Applied Physics Letters*, vol. 81, p. 1234, 7 2002.
- [45] A. Kaminska, P. Strak, J. Borysiuk, K. Sobczak, J. Z. Domagala, M. Beeler, E. Grzanka, K. Sakowski, S. Krukowski, and E. Monroy, “Correlation of optical and structural properties of  $GaN/AlN$  multi-quantum wells-ab initio and experimental study,” *Journal of Applied Physics*, vol. 119, p. 015 703, 1 2016.
- [46] K. Berland, M. Stattin, R. Farivar, D. M. S. Sultan, P. Hyldgaard, A. Larsson, S. M. Wang, and T. G. Andersson, “Temperature stability of intersubband transitions in  $AlN/GaN$  quantum wells,” *Applied Physics Letters*, vol. 97, p. 043 507, 4 2010.



- [47] X. Y. Liu, P. Holmstrom, P. Jänes, L. Thylén, and T. G. Andersson, “Intersubband absorption at  $1.5 - 3.5\mu\text{m}$  in  $\text{GaN}/\text{AlN}$  quantum wells grown by molecular beam epitaxy on sapphire,” *Physica Status Solidi b*, vol. 244, pp. 2892–2905, 8 2007.
- [48] T. Andersson, X. Liu, T. Aggerstam, P. Holmstrom, S. Lourdudoss, L. Thylen, Y. Chen, C. Hsieh, and I. Lo, “Macroscopic defects in  $\text{GaN}/\text{AlN}$  multiple quantum well structures grown by MBE on  $\text{GaN}$  templates,” *Microelectronics Journal*, vol. 40, pp. 360–362, 2 2009.
- [49] C. Bayram, N. Pere-laperne, and M. Razeghi, “Effects of well width and growth temperature on optical and structural characteristics of  $\text{AlN}/\text{GaN}$  superlattices grown by metal-organic chemical vapor deposition,” *Applied Physics Letters*, vol. 95, p. 201 906, 20 2009.
- [50] A. Helman, M. Tchernycheva, A. Lusson, E. Warde, F. H. Julien, K. Moumanis, G. Fishman, E. Monroy, B. Daudin, L. S. Dang, E. Bellet-Amalric, and D. Jalabert, “Intersubband spectroscopy of doped and undoped  $\text{GaN}/\text{AlN}$  quantum wells grown by molecular-beam epitaxy,” *Applied Physics Letters*, vol. 83, p. 5196, 25 2003.
- [51] M. Tchernycheva, L. Nevou, L. Doyennette, F. H. Julien, E. Warde, F. Guillot, E. Monroy, E. Bellet-Amalric, T. Remmele, and M. Albrecht, “Systematic experimental and theoretical investigation of intersubband absorption in  $\text{GaN} - \text{AlN}$  quantum wells,” *Physical Review B*, vol. 73, pp. 125 347–125 358, 12 2006.
- [52] P. K. Kandaswamy, H. Machhadani, C. Bougerol, S. Sakr, M. Tchernycheva, F. H. Julien, and E. Monroy, “Midinfrared intersubband absorption in  $\text{GaN}/\text{AlGaIn}$  superlattices on Si(111) templates,” *Applied Physics Letters*, vol. 95, p. 141 911, 14 2009.
- [53] C. B. Lim, M. Beeler, A. Ajay, J. Lahnermann, E. Bellet-Amalric, C. Bougerol, J. Schormann, M. Eickhoff, and E. Monroy, “Short-wavelength, mid- and far-infrared intersubband absorption in nonpolar  $\text{GaN}/\text{Al}(\text{Ga})\text{N}$  heterostructures,” *Japanese Journal of Applied Physics*, vol. 55, 05FG05, 5S 2016.
- [54] T. Kotani, M. Arita, and Y. Arakawa, “Observation of mid-infrared intersubband absorption in non-polar m-plane  $\text{AlGaIn} - \text{GaIn}$  multiple quantum wells,” *Applied Physics Letters*, vol. 105, pp. 261 108–261 113, 26 2014.
- [55] T. Kotani, M. Arita, and Y. Arakawa, “Doping dependent blue shift and linewidth broadening of intersubband absorption in non-polar m-plane  $\text{AlGaIn} - \text{GaIn}$  multiple quantum wells,” *Applied Physics Letters*, vol. 107, pp. 112 107–112 112, 11 2015.
- [56] M. Monavarian, J. Xu, M. N. Fireman, N. Nookala, F. Wu, B. Bonef, K. S. Qwah, E. C. Young, M. A. Belkin, and J. S. Speck, “Structural and optical properties of nonpolar m- and a-plane  $\text{GaIn}/\text{AlGaIn}$  heterostructures for narrow-linewidth mid-infrared intersubband transitions,” *Applied Physics Letters*, vol. 116, pp. 201 101–201 107, 20 2020.

- [57] J. Shao, D. Zakharov, C. Edmunds, O. Malis, and M. J. Manfra, “Homogeneous  $AlGaN-GaN$  superlattices grown on free-standing (1-100)  $GaN$  substrates by plasma-assisted molecular beam epitaxy,” *Applied Physics Letters*, vol. 103, pp. 232 103–232 108, 23 2013.
- [58] J. Shao, L. Tang, C. Edmunds, G. Gardner, O. Malis, and M. J. Manfra, “Surface morphology evolution of m-plane (1-100)  $GaN$  during molecular beam epitaxy growth: Impact of  $Ga - N$  ratio, miscut direction, and growth temperature,” *Journal of Applied Physics*, vol. 114, pp. 023 508–023 515, 2 2013.
- [59] T. Nguyen, B. Dzuba, Y. Cao, A. Senichev, R. E. Diaz, M. J. Manfra, and O. Malis, “Mid-infrared intersubband absorption in strain-balanced non-polar  $(In)AlGaN - InGaN$  multi-quantum wells,” *Optical Material Express*, vol. 11, pp. 3284–3297, 9 2021.
- [60] C. B. Carter and D. B. Williams, *Transmission Electron Microscopy*. Springer, 2009.
- [61] J. Mayer, L. A. Giannuzzi, T. Kamino, and J. Michael, “Tem sample preparation and FIB-induced damage,” *MRS Bulletin*, vol. 32, pp. 400–407, 5 2007.
- [62] J. D. Casey, M. Phaneuf, C. Chandler, M. Megorden, K. E. Noll, R. Schuman, T. J. Gannon, A. Krechmer, D. Monforte, N. Antoiou, N. Bassom, J. Li, P. Carleson, and C. Huynh, “Copper device editing: Strategy for focused ion beam milling of copper,” *Journal of Vacuum Science and Technology B: Microelectronics and Nanometer Structures Processing, Measurement, and Phenomena*, vol. 20, p. 2682, 6 2002.
- [63] J. R. Michael, “Gallium phase formation in  $Cu$  during 30 kV  $Ga+$  FIB milling,” *Microscopy and Microanalysis*, vol. 12, pp. 1248–1249, S02 2006.
- [64] R. Spolenak, L. Sauter, and C. Eberl, “Reversible orientation-biased grain growth in thin metal film induced by a focused ion beam,” *Scripta Materialia*, vol. 53, pp. 1291–1296, 11 2006.
- [65] J. P. O’Neill, I. M. Ross, A. G. Cullis, T. Wang, and P. J. Parbrook, “Electron-beam-induced segregation in  $InGaN/GaN$  multiple-quantum wells,” *Applied Physics Letters*, vol. 83, p. 1965, 10 2003.
- [66] C. Edmunds, J. Shao, M. Shirazi-HD, M. J. Manfra, and O. Malis, “Terahertz intersubband absorption in non-polar m-plane  $AlGaN - GaN$  quantum wells,” *Applied Physics Letters*, vol. 105, pp. 02 109–021 114, 2 2014.
- [67] T. Kotani, M. Arita, K. Hoshino, and Y. Arakawa, “Temperature dependence of mid-infrared intersubband absorption in  $AlGaN/GaN$  multiple quantum wells,” *Applied Physics Letters*, vol. 108, p. 052 102, 5 2016.

- [68] C. B. Lim, A. Ajay, C. Bourgerol, B. Hass, J. Schormann, M. Beeler, J. Lahnermann, M. Eickhoff, and E. Monroy, “Nonpolar m-plane  $GaN/AlGaN$  heterostructures with intersubband transitions in the 5-10 THz band,” *Nanotechnology*, vol. 26, p. 435 201, 43 2015.
- [69] C. B. Lim, A. Ajay, C. Bougerol, J. Lahnermann, F. Donatini, J. Schromann, E. Bellet-Amalric, D. A. Browne, M. Jimenez-Rodriguez, and E. Monroy, “Effect of doping on the far-infrared intersubband transitions in nonpolar m-plane  $GaN/AlGaN$  heterostructures,” *Nanotechnology*, vol. 27, p. 145 201, 14 2016.
- [70] O. Malis, C. Edmunds, D. Li, J. Shao, G. gardner, W. Li, P. fay, and M. Manfra, “Quantum band engineering of nitride semiconductors for infrared lasers,” in *Novel in-plane semiconductor lasers III*, ser. Proceedings of SPIE 9002, 2014.
- [71] A. Chen, V. Adivarahan, J. Yang, M. Shatalov, E. Kuokstis, and M. A. Khan, “Ultraviolet light emitting diodes using non-polar a-plane  $GaN - AlGaN$  multiple quantum wells,” *Japanese Journal of Applied Physics*, vol. 42, pp. L1039–L1040, 9A/B 2003.
- [72] Y. H. Ra, S. Kang, and C. R. Lee, “Ultraviolet light-emitting diodes using nonpolar  $AlGaN$  core-shell nanowire heterostructures,” *Advanced Optical Materials*, vol. 6, pp. 1 701 391–1 701 399, 2018.
- [73] J. Hartmann, F. Steib, H. Zhou, J. Ledig, L. Nicolai, S. Fundling, T. Schimpke, A. Avramescu, T. Varghese, A. Trampert, M. Strabburg, H. J. Lugauer, H. H. Wehmann, and A. Waag, “Study of 3D-growth conditions for selective area MOVPE of high aspect ratio  $GaN$  fins with non-polar vertical sidewalls,” *Journal of Crystal Growth*, vol. 476, pp. 90–98, 2017.
- [74] M. Sawicka, H. Turski, M. Siekacz, J. Smalc-Koziorowska, M. Krysko, I. Dziecielewski, and I. G. C. Skierbiszewski, “Step-flow anisotropy of the m-plane  $GaN$  (1-100) grown under nitrogen-rich conditions by plasma-assisted molecular beam epitaxy,” *Physical Review B*, vol. 83, p. 245 434, 24 2011.
- [75] M. Sawicka, C. Cheze, H. Turski, J. Smalc-Koziorowska, M. Krysko, S. Kret, T. Remmele, M. Albrecht, G. Cywinski, I. Grzegory, and C. Skierbiszewski, “Growth mechanisms in semipolar (20-21) and nonpolar m-plane (10-10)  $AlGaN/GaN$  structures grown by PAMBE under N-rich conditions,” *Journals of Crystal Growth*, vol. 377, pp. 184–191, 2013.
- [76] J. Smalc-Koziorowska, M. Sawicka, T. Remmele, C. Skierbiszewski, I. Grzegory, and M. Albrecht, “Ferroelectricity in hafnium oxide thin films,” *Applied Physics Letters*, vol. 99, p. 102 903, 10 2011.

- [77] M. Sawicka, A. Feduniewicz-Z<sub>m</sub>uda, H. Turski, M. Siekacz, S. Grzanka, M. Krysko, I. Dziecielewski, I. Grzegory, and C. Skierbiszewski, “High quality m-plane *GaN* grown under nitrogen-rich conditions by plasma assisted molecular beam epitaxy,” *Journal of Vacuum Science & Technology B*, vol. 29, p. 03C135, 3 2011.
- [78] J. Shao, D. N. Zakharov, C. Edmunds, O. Malis, and M. J. Manfra, “Homogeneous *AlGaN* – *GaN* superlattices grown on free-standing (1-100) *GaN* substrates by plasma-assisted molecular beam epitaxy,” *Applied Physics Letters*, vol. 103, pp. 232 103–232 108, 23 2013.
- [79] F. Szmulowicz, M. O. Manasreh, C. E. Stutz, and T. Vaughan, “Temperature and many-body effects on the intersubband transition in a *GaAs/AlGaAs* multiple quantum well,” *Physical Review B*, vol. 50, pp. 11 618–11 623, 16 1994.
- [80] C. Edmunds, L. Tang, J. Shao, D. Li, M. Cervantes, G. G. D. Zakharov, M. J. Manfra, and O. Malis, “Improvement of near-infrared absorption linewidth in *AlGaN* – *GaN* superlattices by optimization of delta-doping location,” *Applied Physics Letters*, vol. 101, pp. 102 104–102 109, 10 2012.
- [81] T. G. Mayerhofer, S. Pahlow, U. Hubner, and J. Popp, “Removing interference-based effects from infrared spectra - interference fringes re-visited,” *Analyst*, vol. 145, p. 3385, 9 2020.
- [82] T. Konevskikh, A. Ponossov, R. Blumel, R. Lukacs, and A. Kohler, “Fringes in ftir spectroscopy revisited: Understanding and modelling fringes in infrared spectroscopy of thin films,” *Analyst*, vol. 140, p. 3969, 12 2015.
- [83] C. Edmunds, L. Tang, D. Li, M. Cervantes, G. Gardner, T. Paskova, M. J. Manfra, and O. Malis, “Near-infrared absorption in lattice-matched *AlInN* – *GaN* and strained *AlGaN* – *GaN* heterostructures grown by MBE on low-defect *GaN* substrates,” *Journal of Electronic Materials*, vol. 41, pp. 881–886, 5 2012.
- [84] B. Dzuba, A. Senichev, T. Nguyen, Y. Cao, R. E. Diaz, M. J. Manfra, and O. Malis, “Indium surfactant assisted epitaxy of non-polar (10-10) *AlGaN/InGaN* multiple quantum well heterostructures,” *Journal of Applied Physics*, vol. 128, pp. 115 701–115 709, 11 2020.
- [85] A. Senichev, B. Dzuba, T. Nguyen, Y. Cao, M. A. Capano, M. J. Manfra, and O. Malis, “Impact of growth conditions and strain on indium incorporation in non-polar m-plane (10-10) *InGaN* grown by plasma-assisted molecular beam epitaxy,” *APL Material*, vol. 7, pp. 121 109–121 117, 12 2019.
- [86] R. Basanta, K. Mahesh, R. K. Mohana, N. Thirumaleshwara, and S. B. Krupanidhi, “Dynamics of the spatial electron density distribution of EUV-induced plasmas,” *Journal of Physics D: Applied Physics*, vol. 48, pp. 432 001–432 007, 43 2015.

- [87] U. Hilmi and A. Asen, “Binary group III-nitride based heterostructures: Band offsets and transport properties,” *Journal of Physics D: Applied Physics*, vol. 35, pp. 591–594, 42 2002.
- [88] Y. Tsai and C. Bayram, “Band alignmanes of ternary wurtzite and zincblende III-nitrides investigated by hybrid density functional theory,” *ASC Omega*, vol. 5, pp. 3917–3923, 2020.
- [89] Y. Gao, D. Sun, X. Jiang, and J. Zhao, “Ab initio analytic calculation of point defects in  $AlGaN - GaN$  heterointerfaces,” *Journal of Physics: Condensed Matter*, vol. 33, pp. 35 002–35 012, 3 2021.
- [90] S. Wei and A. Zunger, “Valence band splittings and band offsets of  $AlN$ ,  $GaN$ , and  $InN$ ,” *Applied Physics Letters*, vol. 69, pp. 2719–2723, 18 1996.
- [91] A. N. Westmeyer, S. Mahajan, K. K. Bajai, J. Y. Lin, H. X. Jiang, D. D. D. Kileske, and R. T. Senger, “Determination of energy-band offsets between  $GaN$  and  $AlN$  using excitonic luminescence transition in  $AlGaN$  alloys,” *Journal of Applied Physics*, vol. 99, pp. 013 705–013 710, 1 2006.
- [92] K. A. Wang, C. Lian, N. Su, and D. Jena, “Conduction band offset at the  $InN - GaN$  heterojunction,” *Applied Physics Letters*, vol. 91, pp. 232 117–232 121, 23 2007.
- [93] A. Hurni, H. Kroemer, U. K. Mishra, and J. S. Speck, “M-plane (10-10) and (20-21)  $GaN - Al_xGa_{1-x}N$  conduction band offsets measured by capacitance-voltage profiling,” *Applied Physics Letters*, vol. 105, pp. 232 108–232 113, 23 2014.
- [94] L. Sang, Q. S. Shu, S. Y. Yang, G. P. Liu, H. J. Li, H. Y. Wei, C. M. Jiao, S. M. Liu, X. W. Z. Z. G. Wang, W. Hao, and B. Shen, “Band offsets of non-polar a-plane  $GaN - AlN$  and  $AlN/GaN$  heterostructures measured by X-ray photoemission spectroscopy,” *Nanoscale Research Letters*, vol. 9, pp. 470–475, 1 2014.
- [95] P. Reddy, I. Bryan, Z. Bryan, J. Tweedie, S. Washiyama, R. Kirste, S. Mita, R. Collazo, and Z. Sitar, “Charge neutrality levels, barrier heights, and band offsets at polar  $AlGaIn$ ,” *Applied Physics Letters*, vol. 107, pp. 091 603–091 609, 9 2015.
- [96] C. Edmunds, “Near- and far-infrared intersubband transitions in polar and non-polar III-nitrides,” Ph.D. dissertation, West Lafayette, IN, 2014.
- [97] S. Birner, T. Zibold, T. Andlauer, T. Kubis, M. Sabathil, A. Trellakis, and P. Vogl, “Nextnano: General purpose 3-D simulations,” *IEEE Transactions on Electron Devices*, vol. 54, pp. 2137–2143, 9 2007.

- [98] S. W. Kaun, E. Ahmadi, B. Mazumder, F. Wu, E. C. H. Kyle, P. G. Burke, U. K. Mishra, and J. S. Speck, “*GaN*-based high-electron-mobility transistor structures with homogeneous lattice-matched *InAlN* barriers grown by plasma-assisted molecular beam epitaxy,” *Semiconductor Science and Technology*, vol. 29, pp. 45 011–45 027, 4 2014.
- [99] A. Senichev, T. Nguyen, R. E. Diaz, B. Dzuba, M. Shirazi-HD, Y. Cao, M. J. Manfra, and O. Malis, “Evolution of indium segregation in metal-polar *In<sub>0.17</sub>Al<sub>0.83</sub>N* lattice-matched to *GaN* grown by plasma assisted molecular beam epitaxy,” *Journal of Crystal Growth*, vol. 500, pp. 52–57, 15 2018.
- [100] O. Ambacher, B. Christian, N. Fiel, D. F. Urban, C. Elsasser, M. Prescher, and L. Kirste, “Wurtzite *ScAlN*, *InAlN*, and *GaAlN* crystals, a comparison of structural, elastic, dielectric, and piezoelectric properties,” *Journal of Applied Physics*, vol. 130, p. 045 102, 4 2021.
- [101] H. Fu, J. C. Goodrich, and N. Tansu, “Band alignment of *ScAlN/GaN* heterojunction,” *Applied Physics Letters*, vol. 117, p. 221 105, 23 2020.
- [102] S. Zhang, D. Holec, W. Y. Fu, C. Humphreys, and M. A. Moram, “Tunable optoelectronic and ferroelectric properties in *Sc*-based III-nitrides,” *Journal of Applied Physics*, vol. 114, p. 133 510, 13 2013.
- [103] S. Barth, H. Bartzsch, D. Gloess, P. Frach, T. Modes, O. Zywitzki, G. Suchanek, and G. Gerlach, “Influence of process parameters on properties of piezoelectric *AlN* and *AlScN* thin films for sensor and energy harvesting applications,” in *Smart Sensors, Actuators, and MEMS VII; and Cyber Physical Systems*, J. L. Sánchez-Rojas and R. Brama, Eds., International Society for Optics and Photonics, vol. 9517, SPIE, 2015, pp. 9–15.
- [104] R. Deng, S. R. Evan, and D. Gall, “Bandgap in *Al<sub>1-x</sub>Sc<sub>x</sub>N*,” *Applied Physics Letters*, vol. 102, p. 112 103, 11 2013.
- [105] M. Caro, S. Zhang, T. Riekkinen, M. Ylilammi, M. A. Moram, O. Lopez-Acevedo, J. Molarius, and T. Laurila, “Piezoelectric coefficients and spontaneous polarization of *ScAlN*,” *Journal of Physics: Condensed Matter*, vol. 27, p. 245 901, 24 2015.
- [106] M. Baeumier, Y. Lu, N. Kurz, L. Kirste, M. Prescher, T. Christoph, J. Wagner, A. Zukauskaitė, and O. Ambacher, “Optical constants and band gap of wurtzite *Al<sub>1-x</sub>Sc<sub>x</sub>N/Al<sub>2</sub>O<sub>3</sub>* prepared by magnetron sputter epitaxy for scandium concentrations up to  $x = 0.41$ ,” *Journal of Applied Physics*, vol. 126, p. 045 715, 4 2019.
- [107] N. Kurz, Y. Lu, L. Kirste, M. Reusch, A. Zukauskaitė, V. Lebedev, and O. Ambacher, “Temperature dependence of the pyroelectric coefficient of *AlScN* thin films,” *Physica Status Solidi A*, vol. 215, p. 1 700 831, 11 2018.

## A. TRADITIONAL TEM PREPARATION RECIPE FOR POLAR AND NON-POLAR III-NITRIDES

Specimens are cut using a table saw for accuracy. Plan-view samples are cut into 1x2 mm<sup>2</sup> pieces, while cross-section samples are glued together using 2 pieces of 1x2 mm<sup>2</sup> pieces and M-bond. Samples that use M-bond have to go through an annealing process at 130°C for >1 hour in the oven to completely cure the M-bond solution. The M-bond solution is located in the fridge in the galley outside of the “SEM Sample Prep” room at the Birck Nanotechnology Center.

### A.1 Allied MultiPrep System 8” Precision Polishing System

1. Polisher alignment: This alignment process is first required during training in order to gain access to use this instrument. In addition, all the details of this process are listed in the “Manual” that is located in the “Polisher” drawer right below the machine.
2. Mount sample onto the polisher holder. We can use any holder for this process based on personal reference. However, it is important to NOT use the alignment holder. The specimen is glued to the holder using clear wax at 130°C inside the film hood. Set the holder on the metal block to cool completely before polishing.
3. **IMPORTANT:** When switching out the sanding paper, we always need to take down a thickness of at least **x3** the roughness of the previous paper. Each sanding paper can generate cracks that are deep up to x3 the roughness of the paper. Thus, by doing this, we can save our specimen from cracking during the dimpler and PIPS processes. The exact recipe below works for III-nitride semiconductors. However, the recipe can be modified to accommodate different materials.
4. A couple of different recipes for plan-view and cross-section samples are listed in the tables [A.1](#) below.

**Table A.1.** Polishing recipe for plan-view (cross-section) III-nitrides.

Diamond paper	Minimum suggested thickness to take off	Sample's thickness as done
30 $\mu\text{m}$	x	300 $\mu\text{m}$
15 $\mu\text{m}$	90 $\mu\text{m}$	200 $\mu\text{m}$
9 $\mu\text{m}$	45 $\mu\text{m}$	110 $\mu\text{m}$
6 $\mu\text{m}$	27 $\mu\text{m}$	80 $\mu\text{m}$
3 $\mu\text{m}$	18 $\mu\text{m}$	60 $\mu\text{m}$
1 $\mu\text{m}$	9 $\mu\text{m}$	40 $\mu\text{m}$
0.5 $\mu\text{m}$	3 $\mu\text{m}$	35 $\mu\text{m}$
0.1 $\mu\text{m}$	1.5 $\mu\text{m}$	30 $\mu\text{m}$

## A.2 Gatan Dimpler Grinder II Model 657

### A.2.1 General Procedure

1. Mount the sample on top of a Cu grid with the back (in the case of plan-view) facing up. Mount with M-bond (that can be found in the fridge) and cure in the oven for >1 hour.
2. Mount the grid on the glass holder for the dimpler. Keep a part of the Cu grid clean. Later, we will use this area to check the thickness of the lamella during the dimpling process.
3. Mount the glass holder onto the stainless steel holder to place it on the dimpler grinder stage (with a magnet).
4. Center the sample under the optical microscope (attached to the dimpler)
  - Set center.
  - Rotate 180° (“table”).
  - Move the stage if needed with the screen on the microscope.
  - Repeat until when we rotate, the center of the sample does not move any more.
  - repeat the same process for the perpendicular direction.
5. Apply diamond paste.



- If the polishing process was stopped at 0.5  $\mu\text{m}$  paper, use 0.5  $\mu\text{m}$  diamond paste and apply it to the sample. Make sure the paste covers the sample completely and add water to thin out the paste if needed. If the paste is too thick or too thin, the sample will break once the Cu wheel grinds directly on the surface of the sample. The consistency of the paste should be thick enough to always maintain a thin layer of paste between the wheel and the surface of our specimen.
- Lower the arm until the Cu wheel touches the sample.
- Set weight from the back (different weight is required for different materials).
- Set arm speed. The smaller the speed, the slower and more gentle the grinding process, leading to a smoother surface.
- Set 0 and the point of contact.
- Set the desired thickness to take off.
- Check with microscope frequently to keep track of the thickness.
- **NOTE:** Everytime taking the glass cylinder off stage, you need to check the cross center again before lowering the wheel for grinding.
- Stop when desired thickness is achieved.

### A.2.2 Improvement of Dimpler

1. Arm speed
  - $\approx 9$  rpm or even slower for soft samples, i.e. m-plane GaN.
  - $\approx 15$  rpm or slower for hard samples, i.e. c-plane GaN.
2. Polish the Cu wheel once you see the “jumps” on the needle. Use 1200-4000p SiC paper with water.
3. For plan-view c-plane GaN (on sapphire)
  - Wheel: use 20 gr or less + 2-4  $\mu\text{m}$  paste when thickness  $> 60 \mu\text{m}$ .
  - Wheel: use 10 gr + 2-4  $\mu\text{m}$  paste when thickness  $> 40 \mu\text{m}$ .

- Wheel: use 10 gr + 0-2  $\mu\text{m}$  paste when thickness  $> 20 \mu\text{m}$ .
- Clothe: use 10 gr + 0-2  $\mu\text{m}$  paste when thickness  $> 10 \mu\text{m}$  and no cracks.

### A.3 Gatan PIPSII Model 695

#### A.3.1 Sample and Gun Alignment

1. Fill up the liquid nitrogen container in the back of the machine to cool down the system before using it.
2. Load the calibration sample onto the stage of PIPS.
  - Push camera to the side.
  - Raise the stage (on the screen).
  - Vent the chamber, then open the cap.
  - Load sample onto the stage (P screen). Then, close the cap. (Make sure the cap is aligned for a vacuum seal).
  - Lower the stage (on the screen). Then move the camera back.
  - Open “GMS 3” on computer.
  - Choose “Specimen prep”  $\rightarrow$  “View”.
  - Move camera up and down to focus (find the hole in the specimen).
3. Align calibration sample (Finding the center of rotation)
  - On the PIPS screen (the actual machine), choose “Alignment”.
  - Pick a distinguishable point on the sample (on the computer screen). This can be a piece of sample, dirt, or any feature on the surface.
  - On PIPS, choose “Align-Right rear beam sector”.
  - Right click, choose “line” and start with the location of the chosen feature on screen.
  - On PIPS, choose “Align-Right front beam sector”.

- Move the 2<sup>nd</sup> point of the line to the feature's location now.
- Do the same thing for the left beam sector. Then, the intersection of these two lines is the center of rotation.
- On PIPS, go to "Home-Align". Then, pick the line connecting the feature's location now and the center of rotation. That is how much we need to adjust the stage.
- Raise up the camera, **DO NOT** move the camera left or right, because you will change the image on the computer screen, hence the stage adjustment.
- Raise the stage up → vent the chamber → open the cap.
- Lower the camera down to focus and find the image on the computer screen.
- Use 2 screws inside (next to the stage) to move the center of the hole to the center of rotation.
- **NOTE:** You can pick the feature to be the center of the hole if you're starting out too far off center of rotation; otherwise, pick some feature on the surface that can be easily identified on the screen after rotation.
- Once you are happy with the adjustment, raise the camera up → close the cap → lower the stage → lower the camera.
- Check on the screen to see if it needs further adjustment. If yes, repeat until satisfied.

#### 4. Align both guns

- Choose "stationary right" on the PIPS screen.
- Choose 6 kV (make sure to turn off the lights to see the gun beam on screen. Also, at this point, after the center of rotation is aligned, we can freely move the camera on the side if needed).
- Use two knobs on the gun to adjust the gun's position. As we rotate the gun (from 10° → 0° and vice versa), we want to see the beam **DOES NOT** change or shift.

- Set gun at  $6^\circ$  (or desired angle as done.)
  - The bigger the angle  $\rightarrow$  the smaller the thin regions for TEM.
  - The smaller the angle  $\rightarrow$  the larger the thin regions for TEM.
- Repeat the same procedure for the left gun.

5. Load the desired sample onto the PIPS holder

- Tip: We can melt a tiny bit of wax (usually clear wax, or yellow wax should work) to hold the sample. Apply wax on the side of the sample and keep the middle region clean.
- Put sample in so that the back of the sample is on top (for plan-view sample) as shown in Figure A.1 below



**Figure A.1.** Cross-section view of mounting plan-view sample onto PIPS holder before milling.

6. Load the desired specimen into the PIPS chamber. The procedure here is the same as in step 2 (load the calibration sample onto the stage of PIPS). However, if the sample is transparent, make sure to focus the camera on the hole.

### A.3.2 PIPS Process

1. On the PIPS screen, choose “Dual beam modulation.”
2. From here, start picking the voltage as it works with your recipe. (for sapphire, usually start at 6 kV.)

3. **NOTE:** Take pictures before and after the milling process to compare the progress and adjust the recipe when needed. Select “Start” on the PIPS screen when ready for milling.
4. Beam condition: 3 keV at  $3^\circ$ . The purpose of this process is to use a high-energy beam to further take down sample thickness to achieve an electron transparent region. Each cycle is 1 hour, and we will keep running the gun with this setup until we start seeing fringes on the computer screen. These fringes are from the GaN layers on the sample
5. Beam condition: 2 keV at  $3^\circ$ . Since sample thickness is substantially reduced from the previous step, we need to lower the beam energy to avoid ion beam damage on our TEM samples. We will stop this process when the fringes become thick.
6. Beam condition: 1 keV at  $3^\circ$ . We will run this process until a hole in our specimen is opened. We want to use as weak an energy beam as possible to obtain a clean surface for TEM images.
7. Beam condition: 0.5 keV. Once the hole starts to open, we use the weakest beam to polish the surface and mill away any unintentional damage caused by higher energy beams. Notice that we do not want to enlarge the hole too much to reserve as much electron transparent thin area as possible.

## B. FIB (TEM PREPARATION) FOR POLAR AND NON-POLAR III-NITRIDES RECIPE

All samples are cut into approximately 1x2 mm<sup>2</sup> pieces. A large specimen can cause physical drifting on stage during the FIB process. Samples are then protected with a thin layer of carbon or Au-Pd using the sputter coating machine located in the “SEM Sample Prep” room at Birck. For polar GaN samples, since the substrate is sapphire, which is insulating, use Ag paint to draw a line from the top of the sample to the metal holder. This step reduces the drift from the e-beam screen due to a charged surface.

### B.1 FEI Nova 200 Nanolab

1. Log in with Ilab to enable the screen.
2. Go to “Column” → “Source” → move the cursor to the “Source” and record the number of hours into the log book.
3. Vent the chamber. Make sure the screw faces the wall.
  - Grid faces the needle (left), facing from the door.
  - Insert manipulator tip (if needed). The needle needs to be changed if the tip is too big to use during FIB.
4. After loading the sample onto the stage, pump the chamber down.
  - Close the door → hold on the door with a slight pressure.
  - Click “Pump” on the screen and wait a few seconds until feeling a small suction on the door. Then you can release your hands. This step is just to make sure the chamber will be sealed correctly and achieve a high vacuum condition layer.
  - Vacuum level should be of the order of  $10^{-5}$  mbar.
5. After the chamber reaches vacuum, click “wake up” to wake up the beams (electron beam and ion beam). Then click “beam on” for e-beam to start imaging with e-beam.

## 6. SEM imaging

- Beam condition: 10 kV, 8.4 nA.
- Un-pause the e-beam.
- Center the beam on the green “x” with “Crossover”.
- Find some spot/object on the surface to focus (right click).
- Zoom into the spot.
- Check working distance “WD” → link to z-height (2<sup>nd</sup> button top-right). Then click “link” on top. Then move z to 5 mm. This is the eucentric height of this instrument.

## 7. E-beam deposition

- Beam condition: 10 kV, 8.4 nA
- Application: Pt
- Size: 18x2x2  $\mu\text{m}$  (xyz)
- Pattern type: Regular rectangle
- Insert the Pt needle (at the bottom) by clicking on the needle box on the screen.
- Goal: Create an extra protection layer for the surface before showering it with the ion beam.
- Repeat: (if needed) until the box is obvious on the screen.
- As finish, unclick the Pt needle to retract the needle.

## 8. E-beam imaging

- Beam condition: 5 kV, 1.6 A
- Re-adjust brightness, contrast, and focus (every time changing I and V because the sample’s image is moved as these values are changed).

## 9. At 52° tilt

- Zero beam shift (1st button, bottom) by right click  $\rightarrow 0$ .
- Unpause the ion beam so that we can track the image on this screen for centering the sample.
- Go to “navigation” (2<sup>nd</sup> button, top) and tilt the sample to 52°. Use the z-knob on the door to adjust the sample so that we can see the same images on both the e-beam and ion beam screens.

#### 10. Ion beam deposition

- Beam condition: 30 kV, 0.3 nA
- Application: Pt dept
- Size: 15x1.5x1  $\mu\text{m}$  (xyz)
- Pattern type: regular rectangle
- Make sure you take a picture and refocus before clicking “start”. When ready, click “start”. Do not repeat this process.

#### 11. Trench: 10 $\mu\text{m}$

- Beam condition: 30 kV, 20 nA
- Size: 17x10x8  $\mu\text{m}$ . Check fig 3.6 for more details.
- Application: Si
- Pattern type: Regular rectangle
- Change type of milling from series to parallel to mill both trenches (top and bottom) at the same time.

#### 12. Trench: 6 $\mu\text{m}$

- Beam condition: 30 kV, 7 nA
- Application: Si
- Size: 17x1x8  $\mu\text{m}$ . Check fig 3.6 for more details.



- Pattern type: Regular rectangle

13. Trench: 3  $\mu\text{m}$

- Beam condition: 30 kV, 3 nA
- Application: Si
- Size: 17xyx8  $\mu\text{m}$ . Check fig 3.6 for more details.
- Pattern type: Regular rectangle

14. Trench 1.25  $\mu\text{m}$

- Beam condition: 30 kV, 1 nA
- Application: Si
- Size: 17xyx8  $\mu\text{m}$ .
- Pattern type: Regular rectangle

15. Cutting side

- Beam condition: 30 kV, 1 nA
- Application: Si
- Pattern type: Regular rectangle
- Make box on the side of the lamella with  $z = 8\mu\text{m}$  to cut and release one size of the sample.
- Cut the right side since the manipulator tip will come in from the right of the lamella.

16. Bottom cut

- Beam condition: 30 kV, 1 nA
- Application: Si
- Size: 17.5x0.3x3  $\mu\text{m}$ . The z-value can be adjusted to make sure it is cut through.

- Pattern type: Regular rectangle
- Tilt the stage back to  $0^\circ$ . then, find the lamella on the ion beam screen.

#### 17. Attach the tip onto lamella

- Beam condition: 30 kV, 0.3 nA
- Application: Pt dept
- Size:  $z = 1\mu m$ , x and y are as big as needed.
- Pattern type: Regular rectangle
- Make sure all the side cuts and bottom cuts are through. There should be only one side in touch (the left side).
- Tip: go to “stage”  $\rightarrow$  “xT align figure”  $\rightarrow$  draw a line and align. This step helps to rotate the sample horizontally.
- Go to the “Nano Control” program on the other computer screen, then change the man. tip from “part position” to “work position”. At this point, you should be able to see the tip of the e-beam window.
- Start moving the man. tip down and close to the sample.
  - Record the height of the sample first.
  - Goal: Bring the man. tip down to that height. Check the height of the man. tip by keeping focus on the man. tip.
  - Move up/down - page up/down
  - Move front/back -  $\uparrow/\downarrow$
  - Move left/right -  $\leftarrow/\rightarrow$
  - Note: As we move up(down), it also moves forward (backward) because of the angle. Thus, remember to adjust it every time.
- Once we can see a part of the tip on top of the sample on the e-beam screen, move the man. tip with care until it touches the sample SLIGHTLY.

#### 18. Cut lamella free

- Beam condition: 30 kV, 1 nA
  - Application: Si
  - Size:  $z = 10\mu m$ , x and y are as big as needed.
  - Pattern type: Regular rectangle
19. Remove lamella from bulk by rotate z-knob on the door **CCW** to lower the stage to 10 mm (check in z-value box).
20. Go to the “Nano Control” window  $\rightarrow$  change step size to  $50\ \mu m \rightarrow$  raise the man. tip. The purpose of this step is to move the man. tip to  $z = 3.5\mu m$  WD. Remember to refocus to keep track of the height of the needle. As you get close, reduce the step size.
21. Clean post B
- Beam condition: 30 kV, 7 nA
  - Application: Si
  - Size:  $z = 10\mu m$ , x and y are as big as needed.
  - Pattern type: Regular rectangle
  - Tilt stage back to  $0^\circ$ , this helps to find the post.
  - Zoom out on the e-beam window and move around to find post B. Once post B is found, tilt the stage back to  $52^\circ$
22. Attach the lamella to post B
- Beam condition: 30 kV, 0.3 nA
  - Application: Pt dept
  - Size:  $z = 1\mu m$ , x and y are as big as needed.
  - Pattern type: Regular rectangle
  - Focus on the needle with the ion beam
  - Use small step size to approach (not too close) the post.

23. Release the man. tip from the lamella

- Beam condition: 30 kV, 0.3 nA
- Application: Si
- Size:  $x = z =$  diameter of the tip.
- Pattern type: Regular rectangle
- After the cut, move the man. tip backward slowly and gently. Then move the stage away from the man. tip by double clicking points on the screen to recenter the image. DO NOT MOVE THE TIP, since there may be some static built up.

24. Thinning 1. The thinning configuration is shown in Figure B.1 below.

- Beam condition: 30 kV, 0.5 nA
- Application: Si
- Size:  $z = 8\mu m$
- Pattern type: Regular cross section
- Angle:  $\pm 2^\circ$  from  $52^\circ$

25. Thinning 2

- Beam condition: 30 kV, 0.1 nA
- Application: Si
- Size:  $z = 8\mu m$
- Pattern type: Cleaning cross section
- Angle:  $\pm 1^\circ$  from  $52^\circ$

26. As you lower the beam condition down to 20 kV, keep slicing the sheet as shown in Figure B.1 until the lamella is ready for TEM.

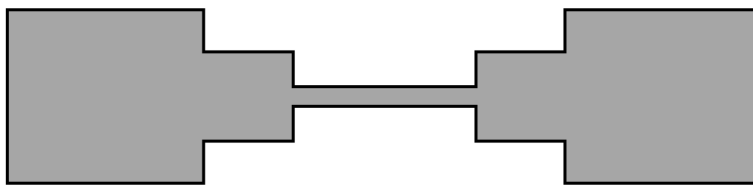


**Figure B.1.** Top view of lamella during thinning process. Lamella is cleaned from both sides leaving the middle region to be the thinnest part for TEM imaging.

## B.2 Thermo Scientific Helios G4 UX Dual Beam

1. Check if machine is asleep (unless was instructed not to do so); if not, put a note in the log book.
2. Log in with Ilab to enable the screen for Helios.
3. Click “Vent” to vent the chamber. It should take 3-5 minutes. Do not interrupt the process unless an emergency action is required.
4. Mounting sample onto holder. Make sure the Omniprob Cu grid is held by the clamp holder with the hole on the right side of the clamp.
5. Load the holder onto the appropriate stage for FIB.
6. Once the chamber is vented, load the stage into the chamber. Make sure to check the z-height before closing the door to make sure the sample will not touch the camera. (Use the standing ruler next to Helios, z-height  $<4$  mm).
7. Click “Pump” to start pumping the chamber. It should take about 5 minutes to bring the chamber to a vacuum. If the process fails, click “Vent” and wait for a moment, then click “Pump” again.
8. Once the chamber is pumped, click “Stage” → “take picture with Nav-Cam”. The purpose of this step is to store the location of the stage so that we can navigate and move the stage to the desired location during the in situ process.

9. Click “Beam on”. This step will turn on both the e-beam and the ion-beam. The e-beam will be on immediately; but the ion-beam will take a while to turn on.
10. On the e-beam screen, choose an obvious point on the sample’s surface to focus on. Then, link the working distance “WD” with the “z-link” at 4 mm.
11. Make sure the e-beam is set at zero to reset the e-beam at the center of the camera. “Beamshift”  $\rightarrow 0$ .
12. Protection deposition with e-beam
  - Beam condition: 2 kV, 3.2 nA
  - Application: C-dep
  - Size: 15x3x0.3  $\mu\text{m}$  (xyz)
  - Click “Multichem”  $\rightarrow$  click “C” ready  $\rightarrow$  wait for a couple minutes before starting the deposition process.
13. Once the deposition is done
  - Retract the chemical needle by unclicking “Multichem”
  - Beamshift  $\rightarrow 0$
  - Tilt to  $10^\circ \rightarrow 20^\circ \rightarrow 30^\circ \rightarrow 52^\circ$ . Check z-height at each step.
14. SEM imaging
  - Beam condition: 2 kV, 0.2 nA
15. Ion beam deposition (Ga)
  - Beam condition: 30 kV, 0.26 nA
  - Insert “Multichem”
  - Application: C-dep
  - Size: 12x3x3  $\mu\text{m}$  (xyz)

16. Once the deposition is done, start making trenches approaching the lamella.
  - Switch the beam condition down to 16 kV ASAP to reduce surface damage caused by the high energy ion beam.
  - Beam condition: 16 kV, 10 nA
  - Retract “Multichem”
  - Application: Si
  - Size: 18x10x8  $\mu\text{m}$ . These trenches are 10  $\mu\text{m}$  apart, with the lamella in the middle, as in Figure 3.6.
  - Pattern type: Regular rectangle
17. Trench: 6  $\mu\text{m}$ 
  - Beam condition: 16 kV, 4.4 nA
  - Application: Si
  - Size: 18xyx8  $\mu\text{m}$ . Check fig 3.6 for more details.
  - Pattern type: Regular rectangle
18. Trench: 3  $\mu\text{m}$ 
  - Beam condition: 16 kV, 1.2 nA
  - Application: Si
  - Size: 18xyx8  $\mu\text{m}$ . Check fig 3.6 for more details.
  - Pattern type: Regular rectangle
19. Clean top and bottom trenches
  - Beam condition: 16 kV, 1.2 nA
  - Application: Si
  - Size: 18xyx8  $\mu\text{m}$
  - Pattern type: Cleaning cross section

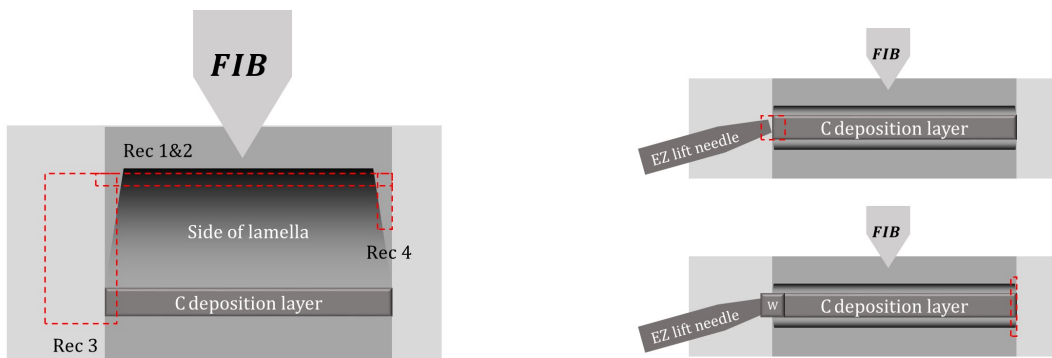
- Angle:
  - Bottom trench:  $52^\circ + 1.5^\circ$
  - Top trench:  $52^\circ - 1.5^\circ$

## 20. Undercut

- Beam condition: 16 kV, 4.4 nA
- Pattern type: Regular rectangle
- Make 4 rectangles as in fig B.2a

## 21. Weld the EZ tip to the bulk

- Beam condition: 30 kV, 41 pA
- Application: W-dep (to reduce Pt damage on lamella)
- Size:  $z=0.75\ \mu\text{m}$  (x and y can be adjusted to fit the side of lamella as in fig B.2b)
- Insert EZ-Lift needle (into the park position). Then use x, y, and z control to move the needle to the desired location for attachment. Please read the EZ-Lift document for more details.
- Insert “Multichem”.



(a) Undercut pattern configuration to release the lamella from the bulk substrate during in-situ FIB. View at  $-10^\circ$  on the ion beam window. (b) Attaching EZ lift needle to lamella. View at  $52^\circ$  on the ion beam window.

**Figure B.2.** FIB process



22. Cut lamella free

- Beam condition: 30 kV, 0.75 nA
- Application: Si
- Pattern type: Regular rectangle (as in fig [B.2b](#))

23. Remove lamella from bulk

- Make sure to take out the “Multichem” needle first.
- ONLY USE “Jog Z” to move the EZ-Lift needle up SLOWLY. Once the lamella is safely removed from the bulk and well above the surface, increase the needle speed to move it up more. Then, move the needle to the park position before retracting it.

24. Clean post B on the Omniprobe grid

- Tilt stage back to  $0^\circ$ , this helps to find the post easier.
- Use “Nav-cam” to find post B (double click on the grid area to move there).
- Tilting the stage between  $0^\circ$  and  $52^\circ$  to make sure both the e-beam and ion beam screens match with each other. (The eucentric height on this machine is around **Z=3.8 mm**). Post B will be cleaned at  $52^\circ$ .
- Beam condition: 30 kV, 0.75 nA. At this point, we can use high current (up to 20 nA, since we have the lamella saved on the tip of the EZ-lift (far away from the ion beam)).
- Application: Si
- Size: As desired, with  $z = 12 \mu\text{m}$ .
- When the process is done, make sure to change the ion beam condition down to 16 kV. This step is to make sure we can protect the lamella elater.

25. Weld lamella to post B at  $52^\circ$

- Insert EZ-lift needle. Then, bring it to the park position. Then, use x,y, and z-jog to move lamella close to post B.
- Insert “Multichem”
- Change beam condition to 30 kV, 0.44 nA
- Application: W. You can increase the current a little to speed up the process (upto  $\approx 2\mu\text{m}$ ).
- Size:  $z=3\ \mu\text{m}$ .

26. Release the EZ-lift needle from the lamella

- Retract “Multichem” first.
- Beam condition: 30 kV, 0.75 nA
- Application: Si
- Size:  $z=5\ \mu\text{m}$ .
- Once the process is done, slowly move the EZ-lift tip away from the lamella, then move it up. Once the tip is far enough from the lamella, use the button to move it to the park position and finally retract it.

27. Weld lamella to post B at  $0^\circ$ .

- Change the imaging condition from the e-beam screen with a beam condition of 5 kV, 0.4 nA. Make sure to zero beam shift and realign both screens at  $0^\circ$  and  $52^\circ$ .
- Beam condition: 30 kV, 0.44 nA
- Application: W. Same as the previous step, the current can be changed to a higher current to speed up the process.
- Size:  $z=1\ \mu\text{m}$ .

28. Thinning both sides until the lamella is about  $1\ \mu\text{m}$  thick. We use  $52^\circ + \alpha$  for the bottom side and  $52^\circ - \alpha$  for the top side.

- Beam condition: 16 kV, 1.2 nA
- Pattern type: Cleaning cross section.
- Size:  $z=15\text{ }\mu\text{m}$ . This large value of  $z$  is used for the reduction of the curtaining effect due to different hardness between layers.
- $\alpha = 2^\circ$

29. Thinning 2 until the lamella is about  $0.5\text{ }\mu\text{m}$ .

- Beam condition: 8 kV, 0.35 nA
- Cleaning cross section.
- Size:  $z=15\text{ }\mu\text{m}$ .
- $\alpha = 0.5^\circ$ . The angle can be changed to  $1.5^\circ$  if the current is smaller than above. The rules are “small current = high tilt” and “large current = low tilt”.

30. Thinning 3 until the protection layer is about 1/2 left.

- Beam condition: 5 kV, 63 pA
- Pattern type: Regular rectangle. Make 2 rectangles to make 2 windows on the lamella. Make sure to run these 2 patterns in parallel.
- Size:  $z=15\text{ }\mu\text{m}$ .
- $\alpha = 3^\circ$ .
- Application: Si 5kV fast.

31. Thinning 4 until just enough protection layer left on top.

- Beam condition: 1 kV, 49 pA
- Pattern type: Regular rectangle. Make 2 rectangles smaller and run them parallel.
- Size:  $z=15\text{ }\mu\text{m}$ .
- $\alpha = 4^\circ$ .
- Application: Si 1kV fast.

32. Polishing. This step is not necessary if you use a nanomill post FIB.

- Beam condition: 500 V, 48 pA
- Pattern type: Regular rectangle. Make one big rectangle to cover the whole lamella.
- Size:  $z=15\text{ }\mu\text{m}$ .
- $\alpha = 5^\circ$ . Only run for about 10-20s each side.
- Application: Si 500V fast.

33. Adjusting angle of milling (to avoid V-shaped lamella). More details are shown in the Figure B.3 below.

- If the protection layer is losing too fast, increase the tilting angle.
- If the lamella's bottom is losing too fast, decrease the tilting angle.

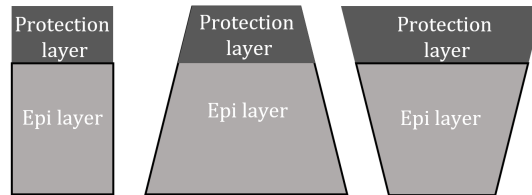


**Figure B.3.** Cross-section view of lamella during milling process. From left to right are: corrected lamella shape, losing the protection layer too fast, and losing lamella's bottom too fast.

### B.3 EZ-Lift - Helios G4 UX Dual Beam

1. Attach EZ-lift tip to the lamella (remove the lamella from the bulk).
  - On e-beam window:
    - Insert EZ-lift. Choose “park position.”
    - Use “Jog Z” to bring the needle to the side of the lamella. Make sure it is not touching the lamella. For safety purposes, make sure the tip is about a few microns away from the lamella when it is at the right z-height.

- On ion-beam window:
  - Working parallel with e-beam.
  - Use “x and y” to move the tip to the side of the lamella.
  - When the tip is at the right z-height and a few microns away from the lamella, move the tip in the x-direction slowly to approach the lamella. Prefer approximately 200 nm distance between the tip and lamella during deposition process.
- 2. Attach lamella to post B: Repeat the process above with the right side of lamella as the EZ-lift tip.

#### B.4 Omniprobe - FEI Quanta 3D FEG

- Software: Autoprobe
- On Ilab: Go to “Microscope” → “Omniprobe” → create new session. Make sure to turn omniprobe from “off” to “active”.
- Back to software → turn autoprobe “on” → “normal” user (for use only), or “supervisor”: user (for calibration and use).
- Procedure:
  1. Eucentric height:  $300\mu m$  (above eucentric point).
  2. Park position:  $1000\mu m$  on the side. In case you cannot insert the needle, go to the controller box and turn it “off” → “restart” the software.
  3. “Home axes”. Make sure the needle is retracted. If any axis changes slowly (during the “home” process), we can stop and rehome it.
  4. For Quanta, the eucentric height is 10.2 mm. Link WD and z.
  5. After going to the park, insert the needle. You should see the tip at 10.2 mm on e-beam.

6. Move the tip to the “+” position at the center. At 2000x, make sure the tip is at “+” precisely. Purpose: set tip to the eucentric position.
  7. go to “eucentric height” and click “go to”.
  8. Switch to the ion beam screen and look for the needle. Now, adjust the needle with both e-and ion beam screens to the “+” position. On the ion beam screen, adjust with **z** only on the program controller. On the e-beam, adjust with **x and y** on the program controller.
  9. Go to “eucentric” → “edit” → “ok”.
  10. On the ion beam screen, check by go to “eucentric height” and see if it’s back of  $300\mu m$ . When it is checked (e-beam should stay the same), go to “park” position.
  11. To get to the lamella, start with the tip at the eucentric height. Then, manually bring the tip down with z controller.
- How to set sample at eucentri point (on e-beam when we want to tilt  $52^\circ$ )
    1. Pick spot, link to z →bring to 10.1 mm
    2. Tilt:  $20^\circ$  →bring sample to “+” position. Repeat with angles  $30^\circ$  and  $52^\circ$ .
    3. Make sure by the time get to  $52^\circ$ , sample does not move any more and focus does not change.

## C. OPERATING NANOMILL FOR POLAR AND NON-POLAR III-NITRIDES

A Fischione Model 1040-Nanomill TEM Specimen Preparation System is used as a post-FIB process to remove amorphous, redeposition, and implantation on the lamella, thus enhancing the sample preparation quality for TEM. A low energy of  $Ar^+$  ion source is used to gently polish the outer layer of the lamella away, leaving clean and undamaged material on the surface for TEM imaging.

1. All details on how to mount the Cu grid (with lamella attached to one of the posts) can be found in the manual located in the “Nanomill” drawer next to the machine.
2. Cool down the machine by pouring liquid  $N_2$  into the dewar in the back of the chamber.
3. As the grid is mounted on the holder and ready to be loaded into the chamber, click “Vent” on the computer screen to vent the chamber. It should take a few seconds for the chamber to be vented.
4. Transfer the holder onto the small stage. Then, screw the holder onto the rod (make sure to do this while the holder is attached to the small stage), and remove it from the small stage.
5. Close the door and click “Pump” on the screen to bring the chamber back to vacuum.
6. Click “Open” to open the gauge that separates the chamber and loading dock.
7. Push the rod all the way in. Make sure that the holder is sitting on the stage inside the chamber, then unscrew the rod to release the holder on that stage. **DO NOT RETRACT THE ROD UNLESS IT IS COMPLETELY UNSCREWED FROM THE HOLDER!**
8. Pull the rod completely out and rest it on the loading dock. Make sure the rod does not slide back into the chamber, then close the gauge.

9. Wait about 20-30 minutes for the chamber to cool down and stabilize. This step is crucial to avoid any temperature drifting during the milling process, and it helps target the milling area better.
10. Start the ion source at 900 eV, 120  $\mu$ A and start imaging.
11. Tilt the specimen to  $-10^\circ$  and move the screen to center the lamella.
12. Find the magnification that works best for you and focus to get a clear image of your specimen. Contrast and brightness can be adjusted if necessary. Change the ion source to 1100 eV if needed. Make sure that you can see the Cu grid on the screen.
13. Change to  $15^\circ$  tilt, and refocus.
14. **NOTE:**
  - Calibration sample: 900 eV, 120  $\mu$ A, at  $\pm 10^\circ$ , 20x20  $\mu$ m area has a milling rate of 7.7 nm/min (Si).
  - For III-nitride samples: use 900 eV, 120  $\mu$ A
  - Switch imaging option to slow (“slow scan”) before the actual milling process.
  - Put a small rectangle around the sample. This rectangle is the target of the beam during the milling process. Make the rectangle comfortably bigger than the area you want to clean.
  - Pick your choice of time interval for milling. Usually, use 2-5 minutes per cycle and check the condition of the lamella. Estimate ahead of time how much time you would need. (For III-nitride samples, use 3 minutes per cycle and 4 cycles at  $+10^\circ$  and 3 cycles at  $-10^\circ$ . Keep in mind that this recipe can be changed across samples.)
15. When the milling process is done, stop imaging. This action will stop the ion source as well.



16. Tilt back to  $0^\circ$ . Then open the gauge to insert the rod back into the chamber, screwing the rod back onto the holder and retracting everything from the stage (rotate clockwise).
17. Retract the rock (with the holder on it) and leave it to rest on the loading dock. Then close the gauge.
18. Vent the chamber and unload the holder onto the small stage. Then close the door and pump the chamber back to a vacuum. Make sure the chamber is under a good vacuum when you leave. If there is any issue with this process, please report it to the coordinator as soon as possible.
19. Remove the Cu grid from the holder and leave it in the membrane box. Leave this box inside the dry box inside the TEM room. You will need to run the specimen through a plasma cleaning process before the actual (S)TEM imaging process.

## D. ALIGNING TEM INSTRUMENTS

### D.1 FEI-Technai T20

- General information: FEI Technai T20 has a low resolution STEM with no field emission. The software that is used with these instruments is “microscope user interface” and “digital micrograph”.
- Microscope user interface:
  1. Bottom window/panel: Include magnification information. High mag. starts with 2250x on screen (2550x on camera). The low magnification range starts at below 2250x and has different beam settings compared to high magnification.
  2. Left and right physical panel:
    - Multifunction x & y: Normally is to move things arounds in x and y directions. Can be switched to other functions as asked.
    - Lower focus knob: Set focus step value from fine to coarse (1  $\rightarrow$  9).
    - Higher focus knob: Change focus with given step.
    - Stick: Move the sample in x and y directions.
    - z-axis: Touch sensor to move sample in z-direction. This is used to find the eucentric height, etc.
    - Intensity: Changing size of condensed lense. Make sure at low level of high mag. (2250x), we are able to see the whole beam on screen.
    - NOTE: This should be a step of checking the beam before loading a sample. In order to do all of these, 1<sup>st</sup>, need to open “col. valves” and make sure the beam can be seen on screen through “vacuum overview”, valves V7 and V4 are opened.
    - Wheel: Used to shift the beam on screen (try to center it).
    - A and B tilt: Used to tilt  $\alpha$  and  $\beta$  on the sample holder.
    - Intensity zoom: used to change the beam size along with zooming.
- Daily alignment

1. How: Go to “Tune” → “Direct alignment”. Check “gun tilt”, “gun shift”, “beam tilt pp x and y”, “beam shift”, and “rotation center”.
2. Gun tilt:
  - Click on “gun tilt”.
  - Use “Multi x and y” to find the brightest spot.
  - The current that is listed on the bottom window of the computer screen will show the biggest value (Name: “Screen”).
3. Gun shift:
  - Use  $R_3$  and  $L_3$  to change spot size.
  - Keep shifting the gun to the center while changing the spot size between 9 and 3.
  - Want to see that as we change the spot size, the beam location (in the middle) does not change.
4. Beam tilt x and y
  - Want to minimize movement of the beam.
  - Use “Multi x and y” to adjust the beam.
5. Beam shift: Keep shifting the beam to the middle.
6. Rotation center:
  - Help when focusing, image will not move.
  - Goal: Using “Multi x and y” to minimize movement.
7. Once all the alignment steps are done, click “Done”. Then reset x and y, turn magnification level to 2250xx, close col. valves, and put holder back in when done. Go to “file” → “exit”.

- Loading sample

1. Pullout
  - Pull the specimen holder out until it stops (be gentle!).

- Turn holder CW, then pullout completely.
- 2. Insert
  - Make sure the holder comes in at the right position (the pin on the holder should match the hole on the loading dock).
  - turn holder CCW, then release. The suction will automatically pull the holder in. Make sure the holder is completely in at the end.
- Circular beam: “Tune” → “Condenser stig.” → Use “multi x and y” to make sure the beam is circular.
- Apertures:
  - Condenser aperture: Used to move the beam to the center. Then fill the screen with the beam (over focus).
  - Objective aperture: Turn ben to 1. Use diffraction mode to help center the beam.
- Setting eucentric height
  1. Start with  $L_1$  ( $\alpha$  wobbler).
  2. If image moves on the screen, use the z-axis button to bring it down until the image no longer moves ( $\approx 60 - 80\mu m$  on z-value).
  3. When happy, hit  $L_1$  again to stop the movement.
  4. Adjust eucentric focus by tilting the button on the panel.
  5. Use CCD camera by hitting  $R_1$  to lift the screen up.
- Digital micrograph
  - “Window” tab → “camera” → “show all” → start view.
  - FFT: “process” → “live” → “FFT”. Should see a circle (amorphous material).
  - As changing focus, the size of the FFT circle should change. **Over focus** = circle fills the screen (perfect focus). **Under focus** = can see the whole circle (want this). It usually fills the screen with a circle, then makes it smaller (under focus).

- Stigmator control
  - \* Control the shape of the circle (circular or oval). We want the beam to be as circular as possible.
  - \* Hit “Stigmator” on the left control panel.
  - \* Start using “Multi x and y” to make the beam circular. Work at high mag. level.
  - \* When happy with the beam’s shape, turn off “Stigmator”. Then find the sample and focus on the actual sample.
- Exposure time
  - CCD camera: 2048 x 2048 pixels.
  - Live view:  $\frac{1}{16}$  (16 = number of pixel in 1 bin).
  - Acquire: 1 (full 2048 x 2048 pixel).

## D.2 FEI-Talos

- Initial check before starting the session
  - Room’s temperature: If  $\Delta T \geq 4$  F from 68 F, report it to the lab coordinator. Also, it is OK to use.
  - Column pressure: If  $\leq 10$  log, and increasing, report to the lab coordinator; otherwise, it is OK to use. If  $\leq 20$  log, report to the lab coordinator immediately.
  - Liquid  $N_2$ : If  $\leq 10\%$ , report to the lab coordinator. If  $10\% \leq N_2 \leq 30\%$ , fill up, then wait for it to stabilize and use. If  $\geq 30\%$ , it is ok to use.
  - Column valves: If open, then close it and report it to the lab coordinator. If closed, it is good to use.
- Checking with Ilab and log into computer
  - ID: user

- Password: guestD6393
- Software (MSL - Microscope Software Launcher)
  - Open: vacuum logger →log →stop (interval:1s)
  - 1<sup>st</sup> way: click “play” on MSL.
  - 2<sup>nd</sup> way: Open TEM user interface, Flucam, TEM image, and Velox manually.
- Check Talos stage condition
  - Extraction Voltage: 3900V
  - FEG Emission: 252  $\mu$ A (should not change during time, if  $\Delta I \geq 3\mu A$ , report to lab coordinator.
  - Cooling (C) for CCD: “Green and Stable = good”, “Red and Archive = ok to use”, “Red and Unknown = report to the lab coordinator”.
  - “Search” tab: Check all apertures (should be rejected; if not, report them).
  - “Camera” tab: Should be BMCeta (should be rejected, if not, check off).
- Plasma cleaning
  1. Open valves: 1 →3 (order of valves in the Plasma Cleaning Room). DO NOT touch 2 unless the pressure is not 15 psi.
  2. Vent and wait until the light switch to “atm.”
  3. Pull out the teflon holder and insert the TEM holder. Then hit “pump” and wait for the high vacuum.
  4. Add time: (usually 30s) and set (the chamber turns purple = plasma is on).
  5. Done →vent →atm →eject holder →insert the teflon plug →pump →wait until high vacuum and close valve 1.
- Loading sample
  - Unload holder

1. Hold the holder as the other hand pushing against the wall of Talos box.
  2. Pull holder out until cannot do it any more and stop.
  3. Rotate the holder CW until cannot it stops
  4. Wait 5-10 s to see if the pump is triggered. At this step, the user can just pull the holder out without waiting, but the user has to risk breaking the vacuum.
  5. If the pump is not triggered, pull the holder out completely.
  6. If the pump is triggered, wait until done pumping, then pull the holder out.
- Load holder
    1. Align the pin on the TEM holder with the machine.
    2. Push the holder in (you should feel a bit of suction at the end) and plug in the wire. Then wait for the 5-minute pumping cycle.
    3. Turn the holder CCW until it stops. Then, gently hold and let the holder slide into the machine. Make sure the holder is all the way in.
  - On Talos screen: make sure you follow the steps and hit the buttons appropriately (“loading”, “unload”, “insert”, “connect cable”, etc.).
  - Reset xyz,  $\alpha\beta$ : This step can be done on a computer (“Search” → “stage” → “control”). If you do it on Talos screen, just hit the “Reset” button.
- Check talos after loading sample
    - Always have the vacuum overview on to keep track of the chamber’s vacuum level.
    - If pressure  $\leq 12$ , user can operate the machine right the way. Else, wait until so.
    - “Setup” tab: Go to FEG registers and choose one of the options below
      - \* 200kV \_ TEM → set (Spotsize should be 3).
      - \* 200kV \_ STEM, spotsize 9: HRSTEM
      - \* 200kV \_ STEM, spotsize 6: STEM + EDS
    - Under “Search” flapout, “Microprobe” is in used (not “nanoprobe”).

- Alignment

1. Eucentric height

- Search →stage →set → $z = 200\mu m$  (eucentric height). This value will change depending on the specimen.
- Can also use z-axis button on panel.
- Find the point of least contrast in the image.
- Reset eucentri focus.

2. Condenser aperture

- Go to 150 kx magnification →bring sample far away from beam →bring beam to center.
- Change intensity to crossover point, bring beam to center.
- Change intensity to enlarge beam and check center of beam.
- Search →aperture →condenser 2 →adjust (with Multi x and y) the center of beam to center of circle.
- Repeat all these step until happy.

3. Make beam circular: Tune →condenser →Multi x and y →click “done”.

4. Direct alignment

- Do not align “gun tilt” and “gun shift”.
- Align: “beam shift”, “beam tilt pp x and y”, and “rotation center”.

5. Diffraction: (click the “diffraction” button on the panel)

- Hit “HDR” at the bottom of the screen to see K-line.
- Tilt  $\alpha$ & $\beta$  to bring the intersection point to center ( $\alpha + \beta < 30^\circ$ . If there is feedback on screen, stop immediately and bring the value of  $\alpha$ & $\beta$  back before the holder gets stuck.
- Unclick “diffraction” on the panel when done. Then lift the screen to take an image.



- TEM images taking
  1. Camera →insert →search.
  2. In “search” tab
    - Int. time: 0.1 (larger value, usually 0.2-1s for acquire)
    - Binning: 1
    - readout: full/half/0.25/0.125 of the CCD screen (usually pick full).
  3. Adjust “Stigmator”
    - Camera →insert →search →live FFT.
    - Tune →stigmator →objective.
    - Click “none” and unclick FFT when done.
  4. For alignment reference: Do all alignment at a magnification level above the mag. that would be used for imaging.
  5. Save images: file →save as →shared drive →direct to the correct folder.
- STEM images taking
  1. FEG registers: Choose STEM with spotsize 6.
  2. STEM →STEM →search.
  3. Want to focus: STEm →focus.
  4. Tune →stigmator →condenser →fix until happy then click “none”.
  5. STEM →unclick “focus” and click “search”. Acquire when you find the desired region.
- EDS (velox software)
  - Turn on Velox software.
  - Change “preference” (directory) →change to the right folder.
  - Click “STEM”, then “HAADF”.
  - Take image before mapping. Then, go to the mapping panel on the screen named “St”. When ready, click the right button to start mapping.

## D.3 Thermo Fisher Scientific-Themis Z

### D.3.1 TEM Mode Pre-alignment Process

- Plasma cleaning: 4 cycles of 15 minutes/cycle with a 5-minute break at the end of each period. This 5-minute break is used to clean out any leftover material in the chamber; hence, enhancing the sample's quality for (S)TEM imaging.
- Take out holder: Pull the holder out with both hands (unplug the connection before do so, if working with the double-tilt holder) until it stops →Rotate the holder **CW** →Push against the thumb to pull the holder out completely.
- Match the pin (on the holder) and the hole (on the loading dock) →Push the holder in until it stops →Plug in the connection (if working with the double-tilt holder) →Leave the holder on the dock and click the desired option on the computer screen →Wait for the airlock cycle →Rotate the holder **CCW** until it stops →Release gently (the holder should slide in automatically). Make sure the holder is completely in by pushing gently at the end of the holder.

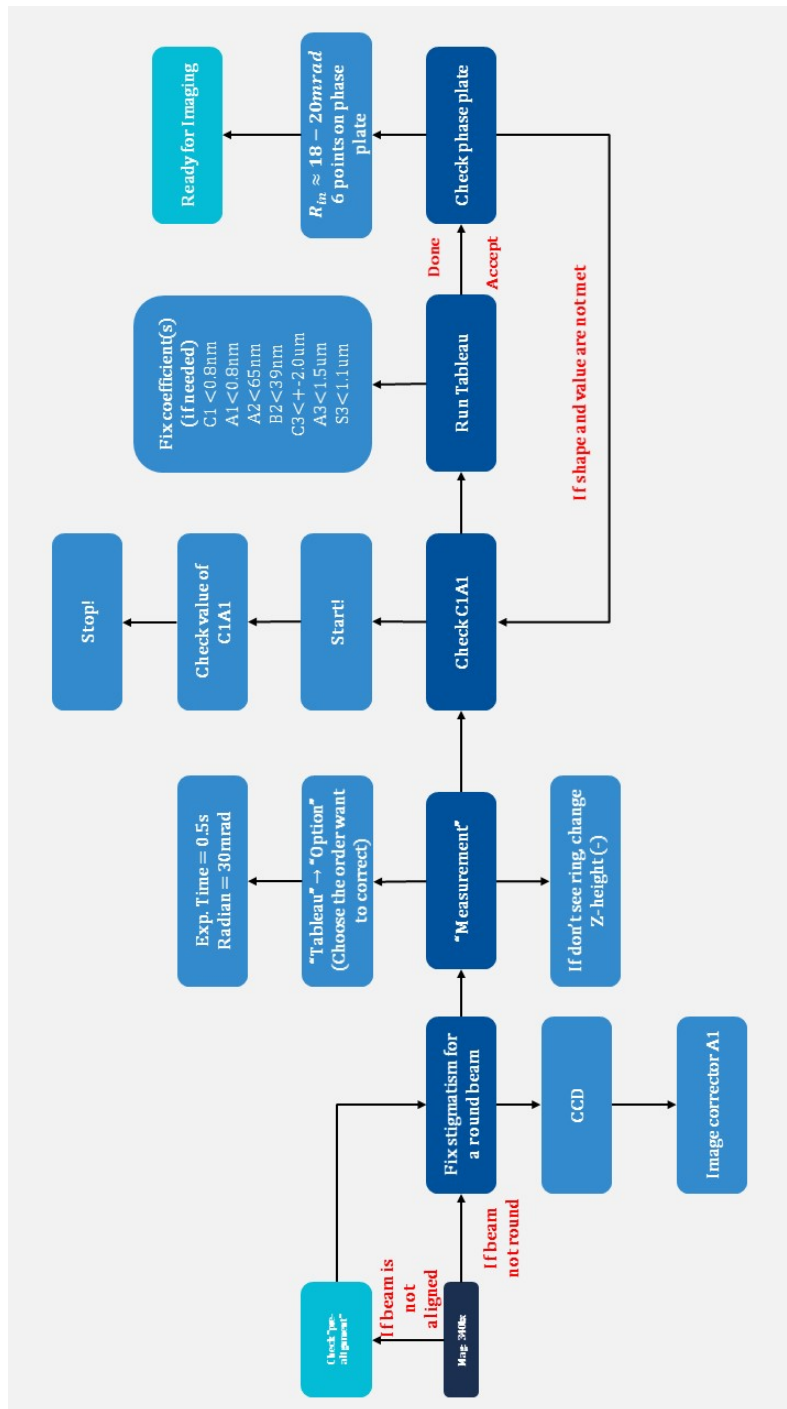


Figure D.1. TEM Pre-alignment Process

### D.3.2 STEM Mode Pre-alignment Process

- For III-nitride samples, it is optimal to align the machine and leave the specimen inside the machine overnight to minimize any drifting at high magnification levels (5.1 Mx and up). If it is impossible to do so, 30 minutes period is enough (at 10 Mx, there will still a small amount of drifting causing “not good” image).
- During the probe correction process
  - Fix in order: A1 and C1 → A2 and B2 → A3, C3, and S3.
  - Do not worry about the 4<sup>th</sup> order since the instrument is not physically equipped for that level of correction.
  - If the shape is square, fix A2.
  - If the shape is a star (with 5-6 points) with a low value, fix A3, S3, and C3.
  - After a new run, A1 and C1 should be in pm value.
- While working with probe correction, if C1A1 is red/dark grey, the beam might be lost.
  - Check the beam in diffraction mode (make sure the beam is centered).
  - If the probe correction process still has problems, turn off the diffraction mode and check the beam (make sure it is as small as possible, round, and centered).
- When the machine is well aligned and ready for imaging, if atoms appear to not young, use manual A1 fine to fix it.

